Feedforward and feedback mechanisms in sensory motor control

Proefschrift

ter verkrijging van de graad van doctor aan de Radboud Universiteit Nijmegen op gezag van de rector magnificus prof. mr. S.C.J.J. Kortmann, volgens besluit van het college van decanen in het openbaar te verdedigen op woensdag 24 april 2013 om 15:30 uur precies

door

Julian Jonathan Tramper

geboren op 26 juni 1983
te Veere

Promotor: prof. dr. C.C.A.M. Gielen

Manuscriptcommissie: prof. dr. A.J van Opstal (voorzitter)
prof. dr. W.P. Medendorp
prof. dr. J.B.J. Smeets (Vrije Universiteit Amsterdam)

Contents

1

General introduction

Every day, we execute a huge variety of movements in a seemingly effortless way, without thinking about how to control each of the individual limbs. Movements such as walking to the train station or drinking a cup of tea seem to happen automatically. As soon as we decide to hurry up to catch the train, we just start walking without thinking about the size of each step or where to put our feet. And if we take a sip of our tea, we do not think about how to bend each of our fingers around the cup, the amount of force needed to lift it, and the trajectory along which we move the cup to our mouth.

All these underlying decisions are made by our brain based on feedforward predictions prior to the movement and sensory feedback during the movement. Since we learn during our childhood how to grasp objects, the brain "knows" which of the more than 600 muscles it needs to activate to pick up the cup from the table. This is an example of feedforward control since the brain uses past experiences to execute the current movement. However, feedforward control can be problematic since we never have a complete knowledge about all the aspects affecting the movement. For example, when the elbow hits something while you are reaching for the cup, the movement trajectory is disturbed. If we do not correct for this disturbance, the hand does not reach the cup. Also, we probably do not know whether the cup is full or empty. Therefore, we cannot determine the exact amount of force needed to lift the cup.

To deal with these kinds of uncertainty, our movements are guided by sensory feedback. We use our eyes, ears and skin to process the visual, auditory and tactile cues that we receive during the movement. In this way, we can determine whether the cup is full or empty by looking into it, and by using proprioceptors in the muscles that sense the forces acting on our limbs. This sensory information needs to travel from the sensors to specific areas in the brain, and is therefore not immediately available to correct ongoing movements. Feedforward control relies on an internal estimate of the movement stored in our memory, and therefore, it is immediately available to use. How the brain combines these feedforward predictions with sensory feedback to generate and control movement is the field of sensory motor control, and is the central theme of this thesis.

1.1 Visual feedback

We rely heavily on vision as a source of sensory feedback. We continuously move our eyes to look at stationary and moving objects that are relevant for the task. We use fast eye movements, called *saccades*, to redirect the eyes to a new location in our visual world. Figure 1.1a shows a saccade in the horizontal direction, which is called the azimuth direction, from left to right (as indicted by the arrow). Since our eyes are separated by about 6 to 7 cm, each eye makes a slightly different angle when fixating on a point of interest. Therefore, we define the gaze direction relative to the midpoint between the eyes, at the position of the nose, as indicated by the thick lines. In a normal situation, we make about three saccades every second. We need that many eye movements because the fovea, which is the region of the retina specialized for high visual acuity, is small and covers only about 2 deg of our field-of-view (Purves et al., 2004). Therefore, we need to move our eyes to obtain a complete and detailed image of the world around us.

Saccades are fast, reaching speeds exceeding 700 deg/s (Carpenter, 1988). During these eye movements we are effectively blind, and therefore, it is beneficial to keep the duration

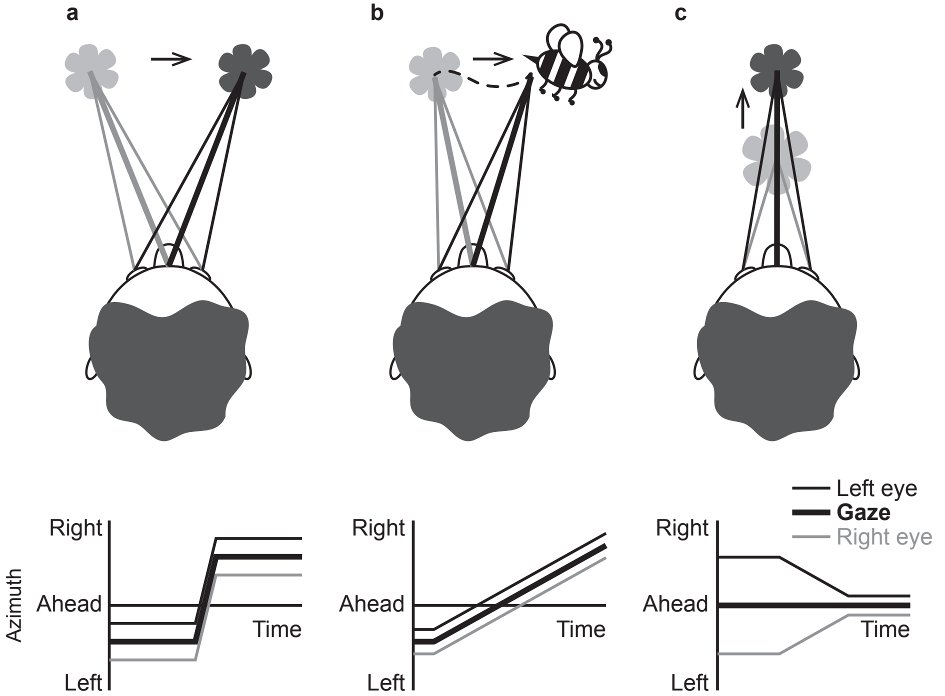

Figure 1.1 Different eye-movement types. **(a)** A saccade is a fast, conjugate movement of the eyes to redirect gaze (indicated by the thick line) to a new location. In this case, an eye movement is made from the left to the right flower. The graph shows the displacement in horizontal direction (called azimuth) of the left eye (black line), right eye (gray line) and gaze (thick black line). **(b)** Smooth pursuit is a slow eye movement to track moving objects by keeping a stable image of that object on the fovea. In this figure, the observer tracks the flight of the bumblebee (dashed line), flying away from the left flower towards the right. **(c)** Vergence is a slow, disconjugate movement of the eyes to redirect gaze between objects located at different distances to the observer. This example shows divergence, which is an eye movement between the flower closest to the observer and the flower farther away. Note that although each individual eye shows a displacement in the horizontal direction, gaze only shifts in the depth direction.

of a saccade as short as possible. The retina consists of light-sensitive receptors, called rods and cones. These receptors capture photons that entered the eye and respond by generating action potentials. This process has a time constant of about 20 ms (Friedburg et al., 2004). Therefore, between saccades, gaze must be kept still to capture visual information. These periods are called *fixations* and can last between tens of milliseconds to several seconds (chapter 2).

Whereas saccades are designed to realign the eyes to a point of interest that falls outside the fovea, we use a different type of eye movement called *smooth pursuit* to follow moving objects. The velocity of such an eye movement matches the velocity of the moving object to keep a stable image of the object on the fovea. This is illustrated in figure 1.1b where the person follows a flying bumblebee. The smooth pursuit system is able to track moving targets up to velocities of about 100 deg/s (Meyer et al., 1985). However, depending on the target speed and the predictability of the movement, additional saccades (so-called catch-up saccades) are needed to keep the fovea aligned with the target (De Brouwer et al., 2002).

Ocular pursuit is driven by visual motion on the retina. The difference in velocity between the eye and the moving object, or retinal slip, is sensed by the retina and processed by motion-sensitive areas in the brain. This error signal is used to compute a smooth pursuit eye movement with the correct amplitude and timing (Krauzlis and Lisberger, 1994). However, there are several studies where smooth pursuit eye movements were observed in the absence of retinal slip (Barnes, 2008). For example, smooth pursuit continues for a short time when the target temporarily disappears (Becker and Fuchs, 1985; Whittaker and Eaholtz, 1982). Also, when the direction and onset of the upcoming target motion is known, smooth pursuit anticipates the movement direction (Kowler et al., 1984; Kowler, 1989), as opposed to a 100-ms latency for unpredictable movement directions (Lisberger et al., 1987). Thus, in addition to sensory feedback, smooth pursuit is also driven by feedforward (predictive) mechanisms (Soechting et al., 2010).

To shift our gaze between near and far objects we use *vergence* eye movements. The eyes converge or diverge to align their visual axes with the point of interest to obtain a proper binocular fixation. In figure 1.1c, the person makes a divergent eye movement from the near to the far flower. Note that the eyes move in opposite directions (disconjugate), which is different from saccadic eye movements where the eyes move in the same direction (conjugate). Also, vergence eye movements differ from saccades in that they are relatively slow (Chaturvedi and Van Gisbergen, 1998).

In daily life, we use a combination of saccades, smooth pursuit and vergence eye movements to direct our gaze to relevant objects in our surroundings. These gaze shifts provide sensory feedback to guide our movement. Therefore, recording eye movements during movement execution gives additional understanding of human motor control. In natural movements such as driving (Land and Lee, 1994), making a cup of tea (Land et al., 1999), or making a sandwich (Hayhoe et al., 2003), gaze explores the task-relevant locations ahead of the limb movement. Therefore, the motor system can use the visual feedback to anticipate and guide the movement.

In **chapter 2** we investigated eye-hand coordination in three dimensions. We discovered that the lead time in the frontal plane was inversely related to the hand velocity when tracing a curved trajectory. This suggests that gaze leads the finger by a constant distance, and not by a fixed amount of time as previously thought.

In **chapter 3** we further explored visuomotor coordination by designing a highly demanding video-game task in which subjects were required to maneuver a left and right hand icon between a series of obstacles. This task elicited a sequence of saccades interleaved with fixations or smooth pursuit segments. The fixations led the hand movements, in agreement with previous studies. Interestingly, also these segments of smooth pursuit led the hand movements. This result suggests that the sensory motor system can use saccades as well as smooth pursuit eye movement to explore the environment to guide the ongoing movement.

1.2 Sensorimotor delays

Suppose that you were asked to track a moving cursor on a computer screen with your finger. Between the time that the cursor changes its position and the time that you correct your arm movement to follow that change, a cascade of neurophysiological and physical processes takes place. Photons from the screen enter the eye where they hit light-sensitive receptors (rods and cones) of the retina. These receptors convert the influx of photons into a series of electrical discharges, called action potentials or spikes, which travel via the optic nerves, passing through the thalamus, to the visual cortex (Purves et al., 2004). From there, via other brain areas, this information reaches the motor cortex, which computes the appropriate activation of the muscles to move your arm. Finally, the muscles receive this signal and start to build up a force large enough to move your arm in the desired direction. Each of these processes takes time. Therefore, the visual information about the cursor position on the screen is not immediately available for the brain, and we cannot move our arm instantaneously to the desired location. The minimum time for the visual information to correct the arm movement is 100–150 ms (Day and Lyon, 2000), which is called the sensorimotor delay.

This example shows that it takes time before sensory input is available to the motor system. Therefore, the sensory information is already out-of-date before it can be used as feedback for correcting the ongoing movement. Nevertheless, from experiments (chapter 2), and from our own experience, we know that we can follow moving objects accurately without any delays. In section 1.4 and 1.5, we explain how the brain can deal with these delays by using feedforward control or by making an up-to-date estimate about the current state of our body and the environment.

1.3 Noise and uncertainty

The brain codes information as a series of action potentials, which are generated by specialized cells called neurons. The intra- and extracellular fluid of a neuron contains charged particles called ions, separated by the neuron's cell membrane. During an action potential, ions cross the membrane through highly selective ion channels, diffusing from the side with a high ion concentration toward the site with a low concentration, thereby creating an electrical discharge. Ion pumps in the membrane restore the ion concentrations to their initial values, after which the neuron is ready to elicit its next action potential (Purves et al., 2004). This passive diffusion process through the membrane is a stochastic process, meaning that the number of ions traversing the membrane varies each time when the ion channels are open. Therefore, the exact timing of an action potential is variable, even when all properties of the cell would remain the same (White et al., 2000). Thus, if you repeatedly present the neuron exactly the same input, each resulting series of action potentials will be slightly different. Since we often do not know the exact source of the variability, we call this 'noise'.

Noise occurs at every stage of sensory motor control (Faisal et al., 2008). It is present in sensory processing where physical properties such as light, sound, or temperature are converted into neural correlates. It is introduced when action potentials are generated and transmitted across synapses (the connections between neurons). It plays a role when action potentials arrive at a muscle to generate force. In addition, the variability in force output of that muscle increases with increasing force, which is called signal-dependent noise (Jones et al., 2002). Faster movements require more force than slow movements, and hence, faster movements are more noisy and less accurate than slow movements.

The brain not only has to deal with noise, but also with other sources of uncertainty. Here, uncertainty refers to incomplete knowledge about the world around us, the task we are engaged in at the moment, and the current state of our body. Delays and noise are sources of uncertainty, but there are many other sources as well. For example, when walking we probably do not exactly know the unevenness of the pavement, or the fatigue of each of our muscles. When we pick up a cup of tea, we may be unsure about its inertia, or whether it is empty or full. The limitations in receptor density of our fingertips introduce uncertainty about where our fingers are placed on the keyboard while composing an email. Situations in which people are interacting with each other, like chatting or playing squash, can introduce a high amount of uncertainty since you do not know what the other will say or which kind of move your opponent will make. How our motor system can deal with noise in the sensory feedback and uncertainty about the environment is discussed in section 1.5.

1.4 Feedback error learning

Because of sensorimotor delays (section 1.2) the information from our sensory system is always out-of-date. For slow movements (several seconds or longer) there is ample time to correct for any mismatch between the true state of the body and the perceived state provided by the sensory system. However, for fast movements of less than about 0.5 s, the feedback from our sensory system is significantly delayed relative to the total movement duration (Franklin and Wolpert, 2011). For instance, saccades are very fast eye movements with durations as small as 30 ms (Smit et al., 1987), which is much shorter than the time it takes before the visual feedback about the target is available to correct the ongoing movement. Still, these saccadic eye movements are very accurate. How is this possible?

One solution that has been proposed assumes that the brain uses a feedback error learning model (Wolpert et al., 1998; Wolpert and Ghahramani, 2000), see figure 1.2. Suppose that we would like to draw a circle on a piece of paper. Since we know from experience what a circle will look like, the desired trajectory for the hand holding the pencil is known. Our brain has to convert this desired trajectory to the appropriate motor command that innervates the muscles in the arm to generate the actual trajectory of the hand. The part of the model that converts the desired trajectory to the motor command is called the inverse model. In our example, the inverse model of the "hand with pencil" is learned during your childhood. Since this inverse model only uses past experiences about the movement to execute the current movement, we call this feedforward control.

Not only during learning, but also when we are fully familiarized with the task, the actual trajectory of the pencil will not be identical to the desired trajectory. Uncertainty of estimating the inertia of the pencil, the resistance of the paper and fatigue of the muscles, makes an exact mapping of the desired trajectory to the actual trajectory impossible. Therefore, we use visual and haptic feedback from our sensory system (sections 1.1 and 1.6) to verify whether the actual trajectory of the pencil corresponds to the desired trajectory

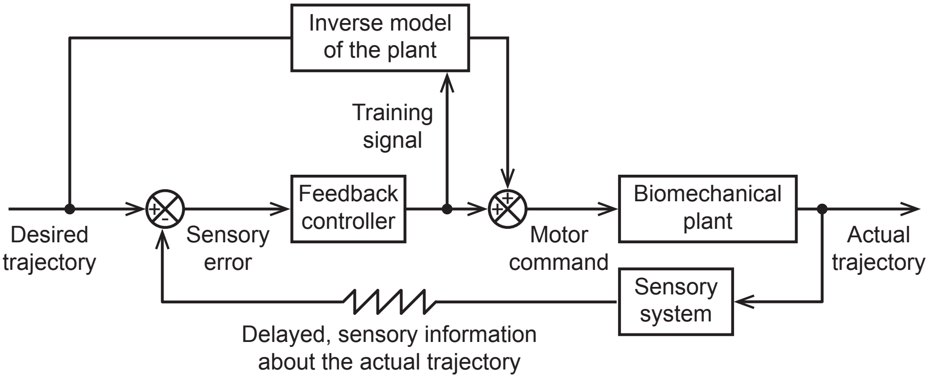

Figure 1.2 The feedback error learning model (Wolpert et al., 1998) describes how the central nervous system can control movements of the eyes, hands, legs, arms or the torso (here called the 'biomechanical plant'). The 'inverse model' represents the neural circuitry that converts the desired trajectory of the plant, for example the arm, to the corresponding motor commands. These commands activate the muscles of the plant. This is called feedforward control. Due to imperfections in the inverse model, and due to noise, our sensory system detects that the actual trajectory is not exactly the same as the desired trajectory, and this information is sent back with a delay. The 'feedback controller' converts the sensory error (or sensory feedback) to a corrective motor command, which can also be used to reduce the imperfections in the inverse model. This is called feedback error learning.

of the circle. If not, the brain needs an additional motor command to correct for this error. The sensory error is thought to enter the feedback controller that converts this signal into the appropriate, corrective motor command. The output of the feedback controller is not only used to correct the ongoing movement, but also to train the inverse model. Since we use the sensory feedback to learn how to make the movement, this is called feedback error learning.

This model uses the sensory error to correct the movement, and to train the inverse model. However, to compute this sensory error, the desired trajectory at a certain time is compared with the outdated sensory information. Thus, there is a mismatch in time between these two signals and therefore both signals cannot directly be compared. The model by Wolpert et al. (1998) does not account for this delay in sensory feedback. A solution may be that the neural system does not wait until the sensory information is available, but that it estimates this sensory information based on recent sensory input, making it immediately available to compute the (estimated) sensory error. This is the topic of the next section.

1.5 Optimal feedback control

We can use over 200 joints and 600 muscles to make a virtually endless variety of movements (Franklin and Wolpert, 2011). In addition, this abundance of joints and muscles allows us to execute a particular movement in an infinite number of ways, making our motor system redundant. For instance, a reaching movement to a cup of tea can be executed using different combinations of muscles resulting in different configurations of the

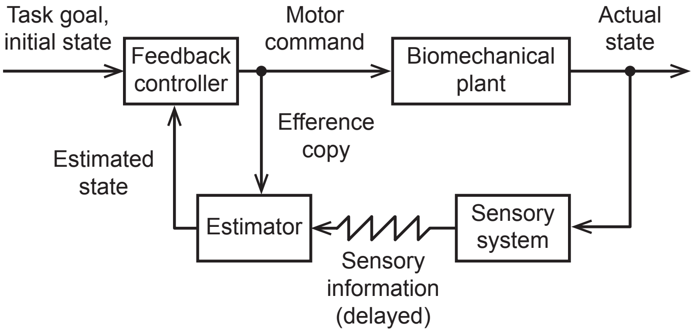

Figure 1.3 The stochastic optimal feedback control model (Todorov, 2004) is a model for motor coordination. Given the task goal and the initial state, the 'feedback controller' generates a motor command that controls the biomechanical plant (e.g., the eyes, the body, or a limb). The model uses an 'estimator' that provides the optimal, estimated state to the controller. This estimation takes into account the (delayed and noisy) sensory information provided by the sensory system, the dynamics of the plant, and a copy of the current motor command ('efference copy').

shoulder and elbow joints. We can make a straight or curved trajectory and vary the speed along this trajectory. It is striking that we nonetheless execute such a reaching movement in a very stereotypic way, namely with a slightly curved path and a bell-shaped velocity profile of the hand (Atkeson and Hollerbach, 1985).

For many years, scientists have wondered why humans choose one specific way of making a movement out of the redundant set of possible ways. Apparently, the brain somehow reduces the number of solutions to simplify the control of movement. One way to achieve this, is to optimize the movement with respect to some physical properties of that movement. This has been formalized in the framework of optimal control theory (Kappen, 2005b; Todorov and Jordan, 2002; Todorov, 2004). The optimal solution to a typical motor control problem is found by optimizing a set of possible actions that achieves the future goal. To each of these actions a penalty, or cost, is assigned. Optimization techniques are used to find the control law, or motor program, that minimizes the total time-integrated cost while reaching the goal.

For sensory motor control, the cost function includes components related to the speed, effort, accuracy or performance of the task. For example, to beat your opponent during a squash game, you prefer that you hit the ball as accurately as possible. At the same time, it is also preferable to save as much energy as possible on each shot. Therefore, minimizing the effort and maximizing the accuracy gives you the optimal motor program, which is a series of motor commands that innervates the appropriate muscles to reach out and hit the ball.

The feedback error learning model described in section 1.4 (figure 1.2) assumes that the sensory information is an accurate representation of the actual trajectory of the movement and does not take into account the noise present in this sensory signal. Stochastic optimal feedback control uses optimization principles to deal with noise and uncertainty (Kappen, 2005b; Scott, 2004; Todorov and Jordan, 2002; Todorov, 2004). The model scheme is shown in figure 1.3. This model uses estimates about the state of the body rather than the actual state provided via sensory feedback, because this information is delayed and noisy, and can therefore not directly be used as a control signal.

The model (figure 1.3) assumes that the task goal and initial state of the biomechanical plant (i.e., the controlled limb) is known to the 'feedback controller'. In order to provide the appropriate motor command for the plant, the feedback controller relies on an internal estimate provided by the 'estimator'. This estimator predicts the sensory consequences of a motor command based on a copy of that command, called efference copy or corollary discharge (Crapse and Sommer, 2008). This prediction, together with the actual (delayed and noisy) sensory feedback and the dynamics of the plant, are weighted according to their reliability to estimate the state of the body. The feedback controller compares this estimate with the task goal and uses this error signal to generate a motor command to control the plant. Since this motor command is based on the optimal estimate provided by the estimator, the sequence of motor commands is equal to the optimal control solution. The estimator can use any type of information, such as past experiences or future predictions, which allows the controller to account for disturbances and uncertainties by updating the ongoing movement.

Chapter 4 shows an example of a stochastic optimal feedback control model that correctly predicts the main features of eye-hand coordination in a video-game task. The problem there is how to find the optimal motion pattern of two hands and gaze, such that both hands reach a target without hitting obstacles. We solve this optimal control problem by modeling the eye-hand coordination as a continuous-state partially-observable Markow decision process (POMDP). The model's solution is in agreement with key features of the observed behavior, such as the spatial locations of eye fixation and hand positions.

Chapter 5 deals with sensory motor control under uncertainty in time-constrained tasks. We investigate human motor behavior in two different video-game tasks where subjects have to steer a ball on a screen to hit a target (first task) or one of two targets (second task) with a specified end time. The movement of the ball was corrupted by noise to impose uncertainty in future ball positions. This study shows that a cost function representing only a trade-off between effort and accuracy at the end time is insufficient to describe the observed behavior. We postulate a new model with an additional cost criterion that penalizes deviations between ball position and the target throughout the movement, forcing arrival on target before the final time.

1.6 Haptic feedback

Haptics refers to the sensing of our environment through touch. For example, haptic feedback is provided by the keys of a keyboard, the vibration mode of a mobile phone, or when reading a text written in braille. When we move our hand along the wall looking for a light switch in the dark, deviations from the expected texture provide information about the location of the switch. Therefore, haptic guidance could be established by a sensory feedback loop that compares the actual sensory input with the expected sensory information provided by efference copy signals (Weiss and Flanders, 2011), as shown in figure 1.4.

During haptic guidance of movements, the biomechanical plant, for example the hand, receives descending motor commands provided by the inverse model. The input of the inverse model is the difference between the desired target state and the actual state provided via sensory feedback. Because of conduction delays (section 1.2), it takes about 100 ms

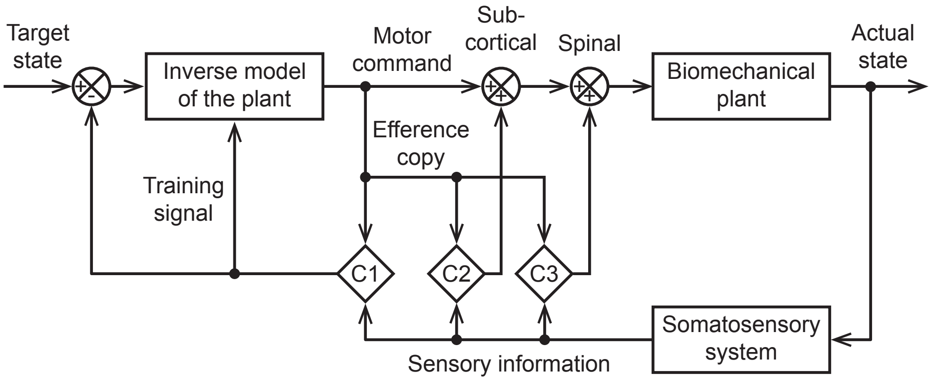

Figure 1.4 Haptic guidance of movement (Weiss and Flanders, 2011). Feedforward control is provided by the inverse model of the plant that sends a motor command to the biomechanical plant. The somatosensory system provides feedback that is compared with a copy of the motor command (efference copy) at multiple levels, as indicated by the boxes with labels C1–C3. The sensory feedback is also used to train the inverse model.

before the somatosensory feedback can correct the ongoing hand movement (Johansson and Flanagan, 2009). Therefore, the brain also estimates the actual state by comparing a copy of the motor command (efference copy) with the delayed sensory feedback (indicated by the box with label C1 in figure 1.4), similar to the optimal feedback control model in figure 1.3. The sensory feedback is also used to train the inverse model, similar to the feedback error learning model in figure 1.2. The output of the inverse model is a motor command that innervates the muscles of the arm to produce the appropriate forces for guiding the hand along the desired trajectory.

Short-latency corrections of about 50 ms found in ongoing exploratory movements suggest that also at the subcortical and spinal levels, sensory feedback is used to update the movement (Weiss and Flanders, 2011). At these levels, the expected somatosensory feedback provided by efference copy signals is compared with the actual somatosensory information (see boxes C2 and C3) to adjust the motor command. In general, feedforward control of movements is prone to the accumulation of errors, since it can only rely on past experiences provided by the inverse model. Therefore, by comparing the expected with the actual sensory information at multiple levels, the somatosensory system keeps track of its actual state to allow continuous updating of the ongoing movement.

In chapters 6 and 7, we investigate the degree to which subjects combine feedforward predictions with feedback control during haptic tracing. Subjects had their finger attached to a robot arm that produced virtual shapes by creating a force field. In **chapter 6**, we used elliptical hoops with a flattened section. Subjects traced the inner surface of these virtual tubes in five repetitive laps. We found that it was difficult for subjects to detect the onset of the flattened section if they were not allowed to touch the shape's surface and had to rely on their internal estimate of the shape acquired during previous laps. Thus, feedforward predictions alone are insufficient to detect upcoming changes in curvature. However, even with continuous haptic feedback, subjects could not precisely anticipate an abrupt change in curvature. In **chapter 7**, we extended the study by also including virtual shapes with a smooth change in curvature. We found that finger speed varied with curvature as predicted by the two-thirds power law. Also, the changes in curvature were anticipated by adjusting the amount of contact force. These results show that, without vision, we cannot anticipate abrupt transitions in curvature, but that smooth changes may be facilitated by feedforward predictions of the somatosensory system.

2

Visuomotor coordination is different for different directions in three-dimensional space

J.J. Tramper
C.C.A.M. Gielen

Published in *The Journal of Neuroscience*, 2011, 31(21): 7857–7866

2.1 Introduction

Gaze shifts in a natural environment require binocular eye movements with both directional and depth components. When playing tennis, a player has to track the ball with the eyes to estimate its movement direction in 3D space before he/she can hit the ball at the proper position at the proper time. This task requires ball tracking with conjugate (saccadic and smooth pursuit) and disconjugate (vergence) eye movements to adjust fixation to the ball at varying distances relative to the subject.

Almost all studies in eye-hand coordination have been done for movements in a frontal plane, implicitly assuming that the characteristics of eye-hand coordination are identical for all movement directions. Recently, Van Pelt and Medendorp (2008) tested the accuracy of pointing movements to remembered target positions and found that changes in vergence led to errors in memory-guided reaches that were based on the new eye position and on the depth of the remembered target relative to that position. These findings demonstrate that eye position affects hand position in pointing. This result and the finding that directional changes in gaze by saccades are much faster than depth changes in gaze (Chaturvedi and Van Gisbergen, 1998), raise the question as to whether eye-hand coordination during tracking a moving target or tracing a shape in 3D is similar for the directional and depth components.

When tracking an object moving in the frontal plane, the trajectories of the eye and hand almost superimpose, whereas the eye leads the hand during tracing a complex shape (Gielen et al., 2009). This illustrates that eye-hand coordination is task-dependent, in agreement with previous observations, that eye-hand coordination changes during learning (Sailer et al., 2005) and that directional and variable errors of the eye and hand change differently according to the task (Sailer et al., 2000).

To investigate any differences between eye-hand coordination in the frontal plane (only conjugate eye movements) and in depth (also requiring vergence eye movements) we have measured 3D eye movements of subjects in two eye-hand coordination tasks. These tasks used stimulus paths in the frontal plane and the same paths rotated along the horizontal axis inducing variations in depth. In the first task, subjects were asked to track a target moving along a curved 3D path with their finger. We investigated whether the observation, that gaze almost perfectly follows a target moving in the frontal plane (Fuchs, 1967), also applies to the depth component for targets moving in 3D by presenting the same stimulus path in the frontal and oblique orientation. In the second task, subjects had to move their finger along a curved path in 3D. In this task, each new fixation point is located at a different depth, resulting in combined fast, conjugate saccades and disconjugate vergence eye movements. Based on the different dynamics for gaze changes in direction and in depth (Chaturvedi and Van Gisbergen, 1998), we expect differences in eye-hand coordination in the frontal plane and for eye-hand movements in 3D space.

2.2 Methods

Subjects Five human subjects (three males) aged between 23 and 56 years participated in the experiment. All subjects were right-handed and had normal or corrected to normal visual acuity. None of the subjects had any known neurological or motor disorder. Further-

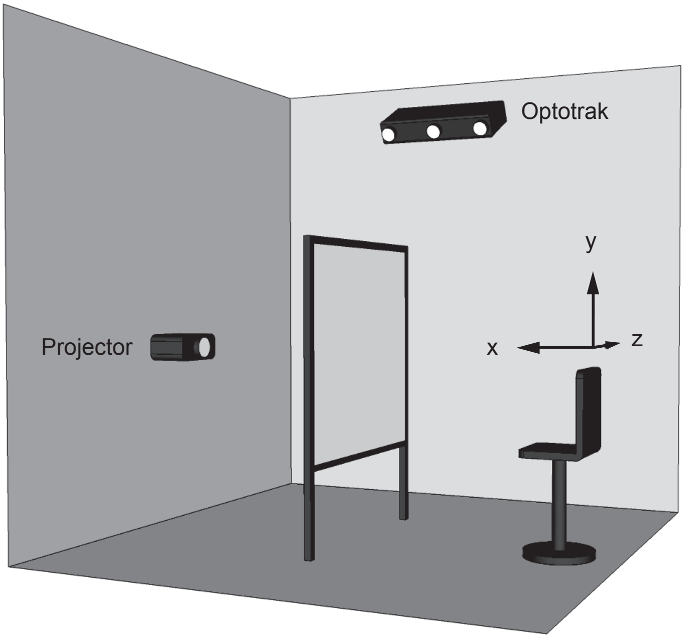

Figure 2.1 Experimental setup. Red-green anaglyph stimuli (123 × 92 cm^2) were projected with an LCD projector (Philips ProScreen 4750) on a 2.5 × 2-m^2 rear-projection screen. The subject was seated in an adjustable chair to align the subject's cyclopean eye with the center of the projection area, approximately 70 cm in front of the screen. Finger movements were measured with an Optotrak 3020 system. A Cartesian coordinate system was defined with its center located at the subject's cyclopean eye, its *x*-axis pointing towards the screen, its *y*-axis pointing upward and its *z*-axis pointing in horizontal direction, to the subject's right.

more, all subjects had participated in previous eye tracking experiments with scleral coils and reported that they had no problems in perceiving depth in the presented anaglyph stimuli. One subject (one of the authors) was aware of the purpose of the experiment, whereas the others were naive. All subjects gave informed consent. The experimental procedures were approved by the local Ethics Committee of the Radboud University Nijmegen.

Experimental setup Subjects were seated in a chair with a high backrest in front of a 2.5 × 2-m^2 rear-projection screen in a completely darkened room (figure 2.1). The subject's eyes were positioned at a distance of approximately 70 cm to the screen. The height of the chair was adjusted to align the subject's cyclopean eye with the center of the projection area. Head movements were restrained by a helmet fixed to the chair.

Visual stimuli were rear projected on the screen with an LCD projector (Philips ProScreen 4750) with a refresh rate of 60 Hz. The size of the computer generated image was 123 × 92 cm^2. A red-green anaglyph stereoscopic system was used to create a red and green copy of the stimulus. Subjects wore anaglyph stereo-glasses with red and green filters to ensure that each eye received input from either the red or green stimulus, respectively. The disparity between the red and green images provided the perception of depth. Although the anaglyph stimuli produced discrepancies between accommodation and vergence, the subjects had an accurate percept of stimulus depth (see figures 2.4 and 2.5), in agreement with previous studies in the literature. For a subject-invariant perception of the 3D stimuli, the perspective transformations had to take into account the distance between the eyes and the distance from the cyclopean eye to the screen. Therefore, inter-pupil distance and distance to the screen were measured prior to the experiment. Typical distances were 6.5 cm for the inter-pupil distance and 70 cm for the distance to the screen.

Finger position was measured with an Optotrak 3020 system (Northern Digital) at a sample frequency of 120 Hz. The Optotrak cameras were located at the upper-right corner with respect to the subject, tilted down at an angle of 30 deg, to track the position of strobing infrared light emitting diodes (ireds) with an accuracy better than 0.15 mm in all dimensions. An ired was placed at the tip of the right index finger, oriented towards the cameras. In addition, an ired was placed next to the right eye to control for any unintended head movements (see below).

Gaze was measured using scleral coils (Skalar) in both eyes simultaneously in a large magnetic field (Remmel Labs). The three orthogonal components of this magnetic field, with frequencies of 48, 60 and 80 kHz, were produced by a $3 \times 3 \times 3\text{-m}^3$ cubic frame. The subject's head was fixated by a helmet in the center of the frame where the magnetic field is most homogeneous. No instructions were given to the subject regarding eye movements during the experiment. The signals from both coils were filtered by a fourth order low-pass Bessel filter (3-dB cut-off frequency at 150 Hz) and then sampled at 120 Hz.

In order to relate finger, gaze and stimulus position to each other, a right-handed Cartesian laboratory coordinate system was defined (figure 2.1). Its origin was located at the subject's cyclopean eye. The positive x-axis pointed forward, i.e., orthogonal to the screen away from the subject, the positive y-axis upward and the positive z-axis in horizontal direction to the subject's right. Note that the x-, y- and z-directions correspond approximately to depth, elevation and azimuth, respectively.

Experiments The experiment started with a calibration trial to calibrate the scleral coils. Subjects were instructed to fixate at $3 \times 3 \times 3$ small spherical targets (radius of 3 mm) with a spacing of 15 cm along each axis, resulting in a total of 27 targets spanning a cube with a volume of $30 \times 30 \times 30$ cm^3. Its center was located at $x = D - 25$ cm, with D the distance between the subject's cyclopean eye and the screen (~70 cm). During the calibration, the frame of the cube was visible. Targets were sequentially presented from left to right, top to bottom and front to back, starting at the upper left vertex of the frontal plane. Subjects had to fixate on the target, press a button, and maintain fixation for one second for sampling of the coil data.

Stimuli were presented in three blocks. In the first block of eight trials (trials 1–8), stimuli were presented in two different conditions ('tracking' or 'tracing'), two different velocities (slow or fast), and two different orientations (frontal or oblique, rotated over 45 deg). In the tracking condition (trials 1, 3, 5, 7), subjects were asked to track a dot (diameter of 1.7 cm at $x = 70$ cm) moving along an invisible 3D path with their right index finger. In the tracing condition (trials 2, 4, 6, 8), the entire path (width of 0.8 cm at $x = 70$ cm) was visible and subjects were asked to trace the path with their right index finger at approximately the same speed as in the tracking condition. The path was defined by a so-called Cassini shape, given by

$$\begin{pmatrix} x(t) \\ y(t) \\ z(t) \end{pmatrix} = \begin{pmatrix} D-d \\ a(1+b\cos(2\omega t))\cos(\omega t) \\ \frac{3}{2}a(1+b\cos(2\omega t))\sin(\omega t) \end{pmatrix}, \tag{2.1}$$

with D the distance between the subject's cyclopean eye and the screen (70 cm), $d = 30$ cm, $a = 20$ cm and $b = 0.5$. The dot started at the top and moved along this path in four cycles, with $\omega = 2\pi/15$ rad/s or $\omega = 2\pi/10$ rad/s, resulting in a movement duration of 15 s per cycle (slow trials: 1 and 5) or 10 s per cycle (fast trials: 3 and 7). Note that for the tracing condition, there is no moving stimulus since the complete path is visible. Therefore, in the tracing condition (trials 2, 4, 6, 8) subjects were instructed to move their finger along the shape with a velocity approximately equal to the velocity in the previous tracking trial. Equation 2.1 defines the frontal orientation with the path in the yz-plane (trials 1–4). The oblique orientation was obtained by rotating this path 45 deg left handed along the z-axis (trials 5–8) such that the lower part of the Cassini shape is closer to the subject than the upper part. This transformation from the frontal orientation (x,y,z) to the 45-deg tilted orientation (x',y',z') is given by

$$\begin{pmatrix} x'(t) \\ y'(t) \\ z'(t) \end{pmatrix} = \begin{pmatrix} x(t) + y(t)/\sqrt{2} \\ y(t)/\sqrt{2} \\ z(t) \end{pmatrix}. \tag{2.2}$$

In the second block of four trials (trials 9-12), the shape of the stimuli was given by a helix with four windings, two different orientations (long axis along z- or x-axis) and two different sizes (small or large). All trials in this block were performed in the tracing condition, where the complete path of the helix was visible. Subjects were asked to follow the shape back-and-forth three times. A helix with the z-orientation (trials 9 and 11) had its long axis along the z-axis and the data points of the helix were defined by

$$\begin{pmatrix} x(s) \\ y(s) \\ z(s) \end{pmatrix} = \begin{pmatrix} D + r\cos s \\ r\sin s \\ q - \frac{ps}{2\pi} \end{pmatrix} \quad (0 \le s \le 8\pi), \tag{2.3}$$

with D the distance between the subject's cyclopean eye and the screen (70 cm), $p = 9$ cm (pitch) and $q = 18$ cm. Helices with the long axis along the x-axis (trials 10 and 12) were obtained by swapping the x- and z-axis, and setting $q = -12$ cm. For both orientations, the small helix was defined by $r = 6$ cm (trials 9 and 10) and the large helix by $r = 10$ cm (trial 11 and 12). In this block, no particular instructions on finger velocity were given. However, it is known that the tracing velocity decreases as curvature increase (Lacquaniti et al., 1983). Therefore, the radius of the helix implicitly imposes the finger velocity, resulting in slow trials (trials 9 and 10) and fast trials (trials 11 and 12).

The last block of eight trials (trials 13–20) was identical to the first block, except that the stimulus shape was given by a Limaçon shape instead of a Cassini shape. The Limaçon shape in the frontal orientation (trials 13–16) was defined by

$$\begin{pmatrix} x(t) \\ y(t) \\ z(t) \end{pmatrix} = \begin{pmatrix} D - d \\ v\sin(\omega t) + \frac{u}{2}\sin(2\omega t) \\ \frac{u}{2} + v\cos(\omega t) + \frac{u}{2}\cos(2\omega t) \end{pmatrix}, \tag{2.4}$$

with D the distance between the subject's cyclopean eye and the screen (70 cm), $d = 30$ cm, $u = 20$ cm and $v = 10$ cm. The oblique orientation (trials 17–20) was obtained by rotating this path 45 deg left handed about the z-axis (equation 2.2).

Each experiment took approximately 40 minutes including the application of eye coils and infrared markers (8 minutes), instructions (2 minutes), calibration (3 minutes), first block with trials 1–8 (10 minutes), second block with trials 9–12 (5 minutes), third block with trials 13–20 (10 minutes) and removing of eye coils and markers (2 minutes).

Data calibration The Optotrak system measures the 3D coordinates of the markers in Optotrak coordinates. The transformation into the laboratory coordinates (i.e., the same coordinate system defined for the stimuli, see figure 2.1) involves a rigid body transformation, which translates the origin of the Optotrak coordinate system to the origin of the laboratory coordinate system and rotates the Optotrak coordinate axes to align with the laboratory coordinates axes. A procedure described by Challis (1995) was used to determine the rigid body transformation parameters (i.e., a rotation matrix and a translation vector).

Precise mapping of gaze position requires calibration of the eye coils. Commonly, a neural network is trained to obtain a proper mapping of the voltage signals of each coil to azimuth and elevation (Goossens and Van Opstal, 1997). This approach works well for 2D gaze positions in the frontal plane but appeared to be less accurate in the depth direction due to small errors in vergence which give rise to relatively large errors in 3D gaze position, especially if the fixation point is relatively far from the subject. Therefore, we used a novel calibration method introduced by Essig et al. (2006). With this approach, azimuth and elevation could be determined with an accuracy ≤ 0.3 deg. This accuracy allowed us to estimate gaze position in depth (i.e., the x-coordinate) with an accuracy of 5 cm when the fixation point was relatively far from the subject ($x = 55$ cm) and up to 1 cm for near fixation points ($x = 15$ cm). Note that this accuracy reflects a variable ('noise') error, which still allows us to determine distances in depth more accurately by averaging over time, which is what a cross-correlation achieves.

Data preprocessing Data were analyzed using Matlab (Mathworks). Two trials (2% of the data) were discarded because of technical problems discovered during the data analysis. In order to skip initial transients in tracking and tracing (Mrotek et al., 2006), data analysis started five seconds after the start of each trial. In addition, for the tracing data the analysis stopped five seconds before the end of each trial. Occasionally, the marker on the finger was not visible for the Optotrak cameras. One trial was discarded because the marker was not visible for more than 700 ms. In seven trials the marker was not visible for 42 to 633 ms. For these trials, missing values were interpolated using a cubic spline. The result was validated by comparing the interpolated finger position with the finger position in the previous and/or next cycles within the same trial. For all these trials, the interpolated finger position did not substantially differ from the measured finger position of the previous and/or next cycles within that trial.

During the data analysis we sometimes found relatively large errors between the median values of gaze and finger position for the x-, y- and z-components. Analyses of these trials revealed that this error originated from multiple sources, including head movements, calibration errors, and the pointing accuracy of the subjects. It is important to have an accurate estimate of gaze and finger position, since small deviations lead to large errors in lead time estimation. Therefore, trials where the median of eye and finger position differed by more than 2 cm were discarded (25% of the data).

Average lead time The lead time of gaze relative to finger position was calculated for the x-, y- and z-components separately. First, for each component of gaze, the mean position of that component was subtracted from the corresponding gaze data. Similarly, the mean finger position was subtracted from the finger position time traces. Then, a Hann (also called Hamming) window (Jenkins and Watts, 1968) was applied to all components of the gaze and finger time traces. The average lead time of gaze relative to finger position was defined as the time of the peak of the cross-covariance between the gaze and finger time trace. A positive lead time means that gaze leads finger position. This procedure was repeated for all trials and all subjects. Additionally, for the tracking condition, the lead time between gaze and stimulus position, and between finger and stimulus position was calculated. Gaze shifts in azimuth direction have the same dynamics as gaze shifts in elevation direction and therefore, the lead times of the y- and z-component were pooled for averaging. We will refer to the y- and z-directions as the frontal direction, and the x-direction as the depth direction. We used a Mann-Whitney U test at the 5% significance level to test for significant differences between lead times for the frontal and oblique orientation of the Cassini and Limaçon shapes (helices were not included in this statistical analysis. In addition, we used a two-sample t test at the 5% significance level to test for significant differences between the following two variables: lead time in frontal direction versus depth, gaze-finger lead time in frontal direction for tracking versus tracing, and gaze-finger lead time in depth for tracking versus tracing.

Effects of saccades on lead time During tracing, gaze moves along the stimulus shape by a sequence of saccades (Reina and Schwartz, 2003, see also *Results*). The effect of saccades on the estimate of lead time between gaze and finger position is illustrated in figure 2.2. Suppose that a subject moves the finger along a straight line at a constant velocity. If saccades move gaze to a new position on the line and if gaze remains at this position until the hand has reached that position, the mean lead time of gaze, as obtained by cross-covariance, is larger for long fixation times (large saccades, figure 2.2a) than for short fixation times (small saccades, figure 2.2b).

In this study, we investigate the relative timing of gaze and finger position when subjects move their finger along a closed, curved trajectory. As an example, figure 2.3 shows simulations of gaze and finger position (gray and solid black line, respectively) for movements along a circle in the frontal (yz) plane, assuming a constant finger velocity and assuming that the finger moves perfectly along the circle. Furthermore, let us assume that gaze jumps to a new position at time t, and that this new position is equal to the finger position at time $t + t_{fix}$ (figure 2.3a). Moreover, assume that gaze stays at this future finger

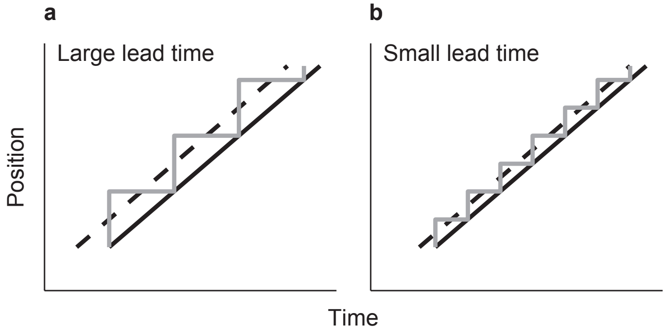

Figure 2.2 Illustration of the relation between fixation interval between saccades and time delay between gaze and finger position. **(a)** Assume that a subject is instructed to move the finger along a straight line at a constant velocity and that the subject does so by a sequence of saccades (gray line) with constant fixation times between saccades. Also assume that gaze moves to a new position as soon as the finger (solid black line) reaches the gaze position. A relatively small number of fixations (three in this example) with long fixation times between saccades results in a relatively large effective lead time (dashed line) of gaze relative to finger position. **(b)** A relatively large number of fixations (six in this example) with short fixation times results in a relatively small effective lead time of gaze relative to finger.

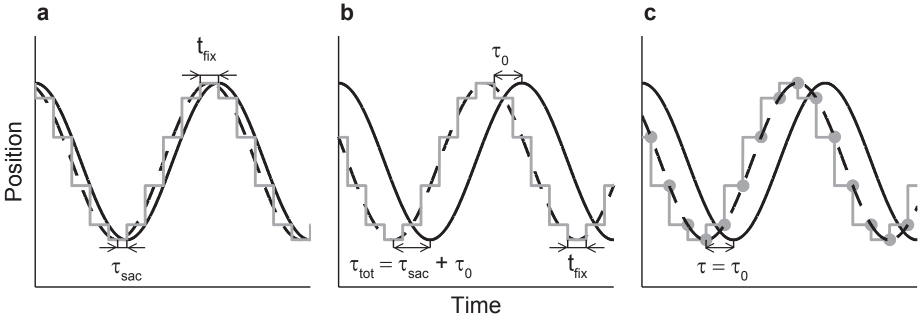

Figure 2.3 Schematic illustration of the analysis to calculate lead time of gaze relative to hand. **(a)** Graphical representation of one directional component of gaze position (gray line) and finger position (solid black line) while tracing a circle in the frontal (*yz*) plane at a constant velocity. t_{fix} is the subject's fixation time between saccades, which is constant in this example. In that case, maximum overlap between gaze and finger position, which corresponds to the time of the peak of the cross-covariance function between gaze and hand position, occurs when finger position is shifted by a time τ_{sac}, indicated by the dashed line. **(b)** Same as (a), but now gaze position leads hand position by an additional time τ_0. Maximum overlap occurs when finger position is shifted by a time $\tau_{tot} = \tau_{sac} + \tau_0$ toward the left (dashed line). **(c)** Same as (b), but the saccade onsets (gray dots) are interpolated by a cubic spline (dashed line). Maximum overlap between this dashed line and finger position occurs when finger position is shifted by $\tau = \tau_0$.

position until the finger has reached that position. The lead time of gaze with respect to finger position corresponds to the time shift that gives the best overlap between gaze and finger position, indicated by the dashed line in figure 2.3a. Since this lead time emanates from the fact that gaze leads the finger by a sequence of saccades, we call this the saccadic lead time τ_{sac}.

If we assume a constant fixation time between saccades, the saccadic lead time equals half the fixation time (i.e., $\tau_{sac} = \frac{1}{2} t_{fix}$), since this corresponds to the time shift that gives the best overlap between gaze and finger position (see the dashed line in figure 2.3a). Similarly, if there would be one single fixation with a duration t^i_{fix}, its corresponding individual saccadic lead time τ^i_{sac} would be equal to $\frac{1}{2} t^i_{fix}$. In general, fixation times are not constant. In order to find an average saccadic lead time τ_{sac} of a trial, each individual saccadic lead time τ^i_{sac} should be weighted according to the corresponding fixation time t^i_{fix}, resulting in

$$\tau_{sac} = \frac{\sum_i \tau^i_{sac} t^i_{fix}}{\sum_i t^i_{fix}} = \frac{1}{2} \frac{\sum_i (t^i_{fix})^2}{\sum_i t^i_{fix}} \tag{2.5}$$

which simplifies to $\tau_{sac} = \frac{1}{2} t_{fix}$ if all fixations have the same duration t_{fix}.

Next, we extend the model by assuming an additional lead time τ_0 (figure 2.3b). Thus, each saccade at time t brings gaze to a new position which is equal to the gaze position at time $t + t_{fix} + \tau_0$. This implies that gaze jumps to a new position before the finger has reached the previous gaze position. Figure 2.3b shows that in this model, the total lead time τ_{tot} is equal to the saccadic lead time plus τ_0. We will call τ_0 the primary lead time.

The model described above gives us the total lead time, but is insufficient to quantify the contribution of the saccadic and primary lead time separately from the data. Therefore, we determined all saccade onsets for each directional component (y and z). These saccade onset points were interpolated by a cubic spline (dashed line in figure 2.3c). One trial (1% of the data) was discarded because the number of saccade onset points was too small to produce a reliable interpolation curve. It is obvious that the primary lead time τ_0 corresponds to the difference in time between the measured finger position (solid black line) and interpolated line (dashed line), which can easily be determined by cross-covariance. This method also allows us to estimate the average lead time, since this is equal to the difference between the total lead time and primary lead time.

Effect of finger velocity on primary lead time The analyses described in the previous section provide the total lead time of gaze relative to finger position and its two components: a saccadic lead time, which is a function of the fixation times between saccades, and a primary lead time. Although the primary lead time is independent of fixation time, it may depend on finger velocity (Gielen et al., 2009). Therefore, we propose two hypotheses regarding the effect of finger velocity on the gaze-finger lead time. Our null-hypothesis is that the primary lead time is constant and independent of finger velocity. Alternatively, we hypothesize that gaze leads the finger by a constant distance. Therefore, we plotted the primary lead time as a function of mean tangential finger velocity $v = \sqrt{v_x^2 + v_y^2 + v_z^2}$ and calculated the correlation between primary lead time and mean finger velocity.

If the latter hypothesis is true, the primary lead time τ_0 is equal to lead distance Δs divided by the mean tangential finger velocity, and therefore, the primary lead time τ_0 as obtained from the cross-correlation should decrease for higher tangential finger velocities. We applied three different methods to obtain an estimate for Δs. The mean lead distance was obtained by fitting $\tau_0 = \Delta s / v$ for each subject by variation of Δs (method I). We used the bootstrap method ($n = 100$) to compute the standard deviation. In a second approach we calculated $\Delta s = v\tau_0$ for each trial, which gives the mean lead distance and standard deviation for each subject and for all data (method II). In addition, we determined the lead distance directly for every trial as the mean distance between gaze and finger position at each saccade onset (method III). We used a two-sample t test at the 5% significance level to test for significant differences between the lead distance distribution obtained by method I and II, and a Mann-Whitney U test at the 5% significance level to test for significant differences between method I and III, and method II and III.

2.3 Results

Behavior during tracking Figure 2.4a shows a quasi 3D view of stimulus (dashed line), gaze (gray line) and finger position (solid black line) for subject S5 tracking a target moving along the oblique Cassini shape. The dashed line is hard to distinguish from the solid line due to the almost perfect tracking by the subject. Figure 2.4b–d shows the corresponding frontal, top and side view, respectively, for one repetition of the stimulus. In the tracking condition, gaze follows the moving target quite well by smooth pursuit in three dimensions. Gaze and finger trajectories deviate more from the stimulus path in the depth direction (x) than in the frontal direction (y and z; compare panels b and c). In addition, gaze occasionally deviates from the target during blinks and small saccades. Data in figure 2.4 are representative for all subjects.

Figure 2.4e–g shows the corresponding time traces of stimulus (dashed line), gaze (gray line) and finger position (solid black line) for the x-, y- and z-component, respectively. The time traces show that gaze is superimposed almost perfectly on hand position in the y- and z-direction. In the x-direction (depth, figure 2.4e), the noise is larger than in the y- and z-directions due to small errors in measurement and calculation of vergence (see *Methods*). These results demonstrate that subjects are able to perceive the anaglyph stimuli correctly and that they have an accurate percept of the position of the moving target in 3D. In addition, the time traces show that gaze leads finger position by a small amount of time. This will be quantified in more detail later.

Behavior during tracing Figure 2.5a shows a quasi 3D view of stimulus (dashed line), gaze (gray line) and finger position (solid black line) of the same subject (S5) for tracing the very same shape as in figure 2.4. Figure 2.5b–d shows the corresponding frontal, top, and side view, respectively. For tracing, the azimuth and elevation components of gaze move along the completely visible shape by a sequence of saccades. During a saccade, gaze deviates from the stimulus path as a result of transient divergence (see figure 2.5c,e). This divergence originates from an asymmetry between abducting and adducting saccadic eye movements. Since the abducting eye has a higher acceleration in a horizontal saccade and is on-target somewhat earlier than the adducting eye, the binocular fixation point shows an outward-looping trajectory in depth during a saccade (Collewijn et al., 1997). In the x-direction (depth), these deviations can be as large as 5 cm for large saccades and are disproportionately larger for far than for near targets due to the nonlinear relation between vergence and distance.

Figure 2.5e–g shows the corresponding time traces of gaze (gray line) and finger position (solid black line) for the x-, y- and z-component, respectively. In the x-direction,

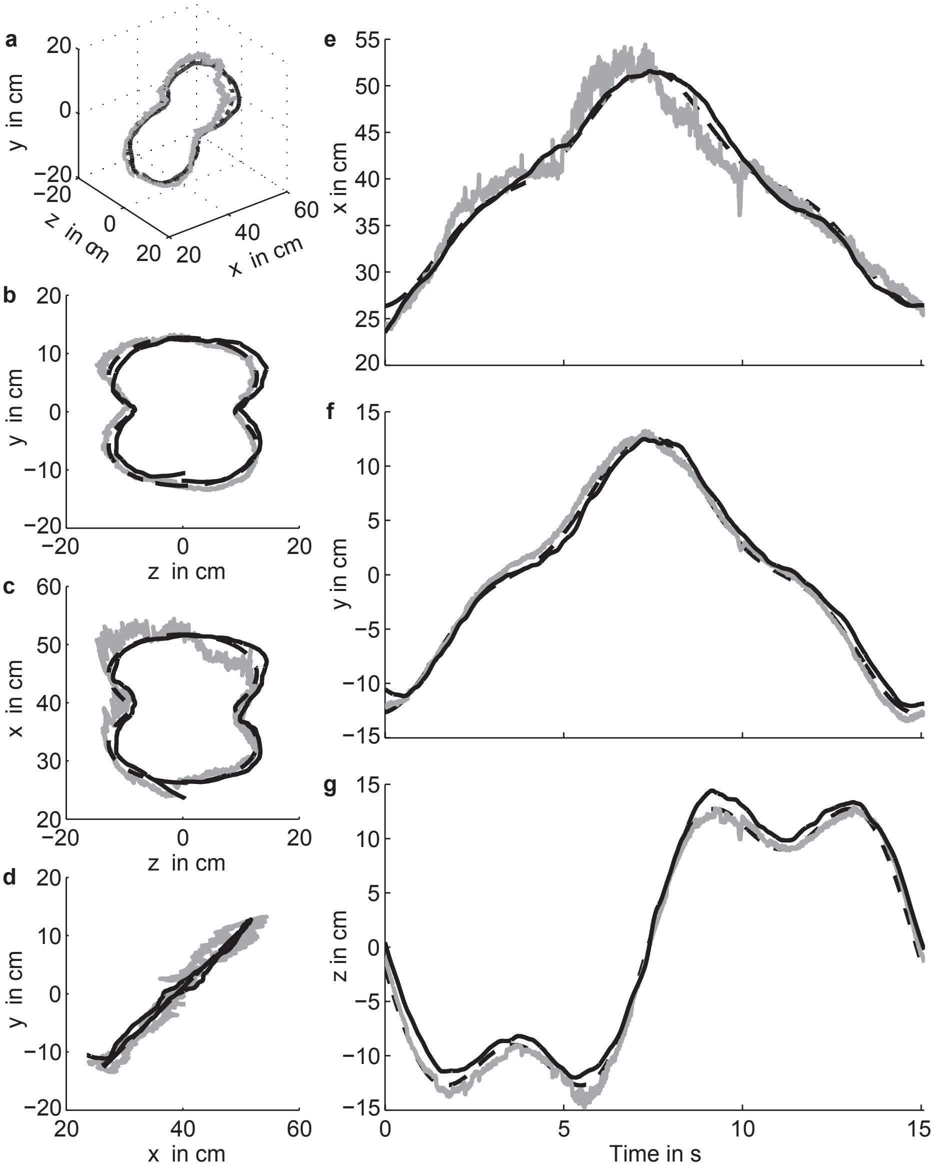

Figure 2.4 Tracking condition. Stimulus (dashed line), gaze (gray line) and finger position (solid black line) of subject S5 tracking the oblique Cassini shape. Data of one cycle is shown. **(a)** Quasi 3D view, **(b)** frontal view, **(c)** top view and **(d)** side view. **(e)–(g)** show the corresponding time traces for x-, y- and z-direction, respectively.

changes in gaze are slightly noisy, but otherwise smooth as usual for vergence eye movements, except for the transient divergence during saccadic gaze shifts (see expanded time trace in figure 2.5e). In contrast to the tracking condition, the y- and z-components of gaze are not smooth but consist of a sequence of saccades. Gaze jumps to a new position on

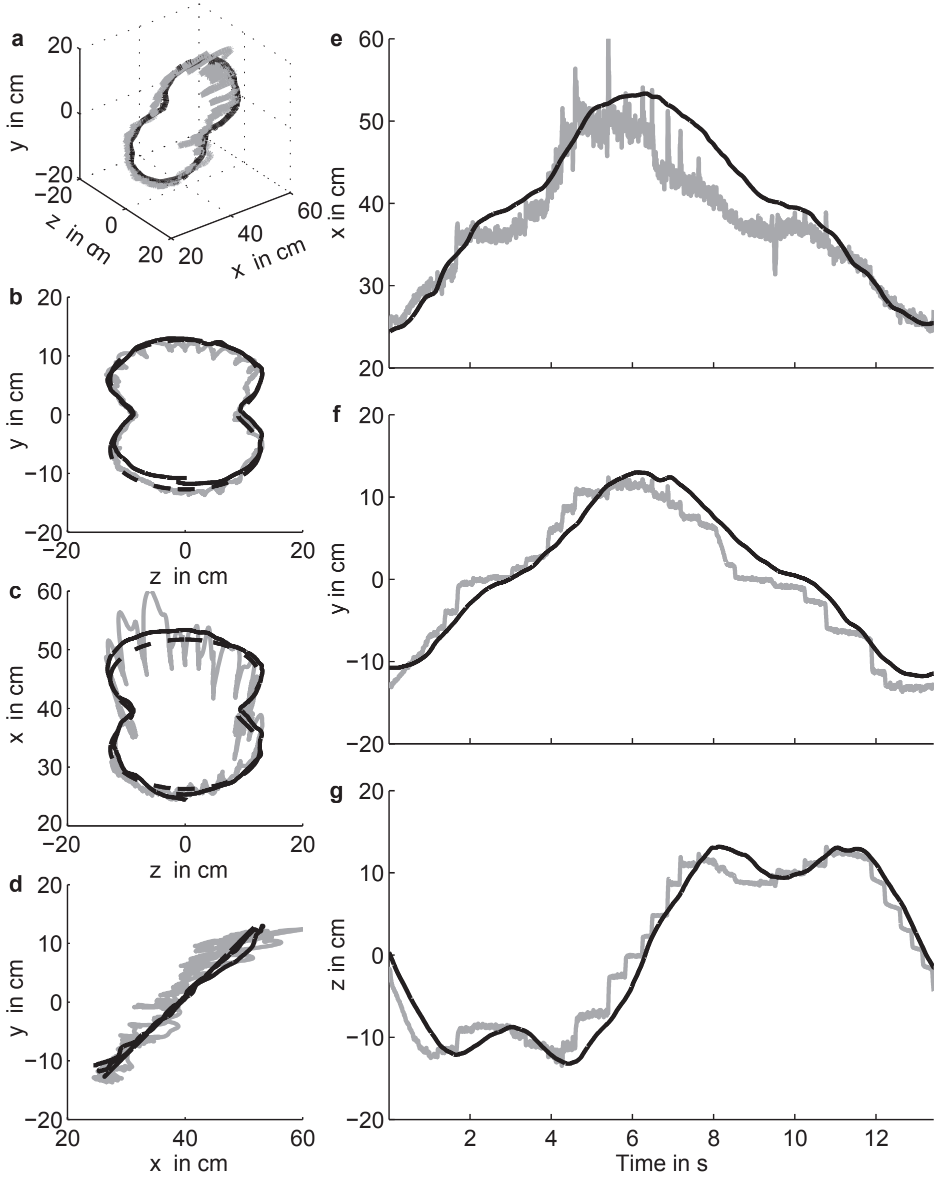

Figure 2.5 Tracing condition. Stimulus (dashed line), gaze (gray line) and finger position (solid black line) of subject S5 moving the finger (tracing) along an oblique Cassini shape. **(a)–(g)** as in figure 2.4. Small panels on the right show expanded time traces (panel e–g).

the shape and fixates there until the finger is close to this position. As soon as the finger is close to that position, a new saccade brings gaze to a next position on the shape (see expanded time trace in figure 2.5f,g). Gaze position clearly leads finger position for the y- and z-direction. Similar results were obtained for the Limaçon shapes and helices.

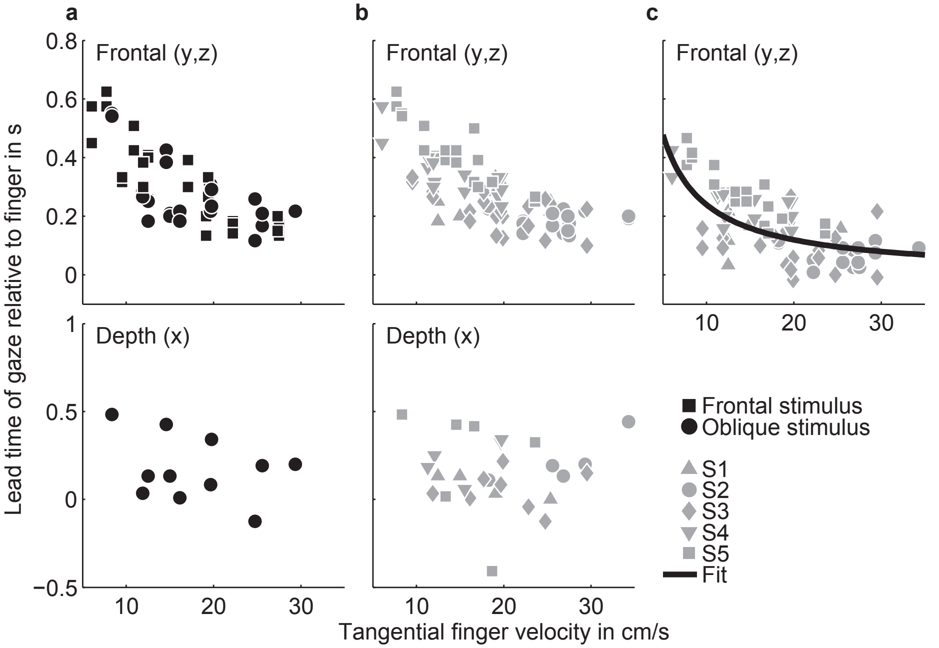

Figure 2.6 Lead times of gaze relative to finger for the tracing condition. The upper and lower panel show values for the frontal directions (y and z) and the depth direction (x), respectively. **(a)** Time of the peak of the cross-covariance function between gaze and finger position as a function of the mean tangential finger velocity. Only data for the Cassini and Limaçon stimulus shapes are shown. Squares and circles represent data for the frontal and oblique stimulus orientations, respectively. The lead times shown here represent the total lead time (see figure 2.3b). **(b)** Same as (a), but lead times of trials with the helices as stimulus shape are included as well. Different gray symbols refer to data from different subjects. **(c)** Time of the peak of the cross-covariance function between gaze position after interpolation of the saccade onsets with a cubic spline and finger position. The lead times shown here represent the primary lead time (see figure 2.3c). Different gray symbols refer to data from different subjects. The black line shows the best fit of $\tau_0 = \Delta s / v$ over all subjects.

Lead time in gaze-finger coordination As explained in the *Methods* section, the time of the peak of the cross-covariance between gaze and finger position gives a measure of the mean lead time of gaze relative to finger position. Figure 2.6a shows the mean lead time of gaze relative to the finger (corresponding to time of the peak of the cross-covariance function) in the y- and z-direction (upper panel) and depth (x-) direction (lower panel). Data of all subjects are shown, but only trials with the Cassini and Limaçon stimulus shapes are included (no helices). Squares and circles in figures 2.6a represent lead times for the frontal and oblique stimulus orientations, respectively. The lead times shown here represent the total lead time (see figure 2.3b). The lead times of gaze relative to the finger for the components in the frontal plane are not significantly different for the frontal and oblique stimulus orientations. This means that any depth components in the path do not affect the lead times for the components of gaze and hand in the frontal plane. We also tested whether lead times in the y- and z-direction (upper panel) were different for Cassini and Limaçon shapes with the frontal orientation (squares) versus the shapes with

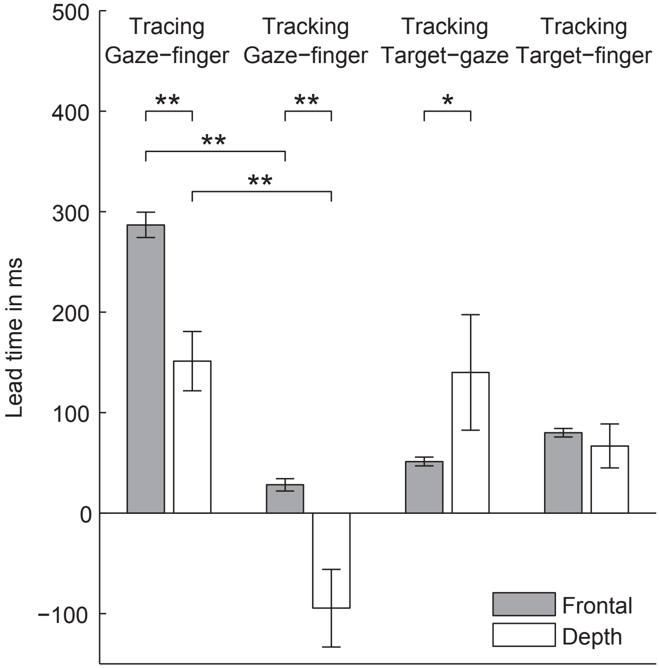

Figure 2.7 Lead times in the tracking condition. Lead time of gaze relative to finger (for tracing and tracking), target relative to gaze (tracking) and target relative to finger (tracking) in the frontal direction (gray bars) and depth (white bars). Values were obtained by averaging over all trials and subjects. Since the data show mean values over trials and subjects, we provide the standard error (SE, error bars) as a measure of the error in the estimate of the mean. Significant differences are indicated by $*$ ($p < 0.05$) and $**$ ($p < 0.01$). The negative gaze-finger lead time in depth for the tracking condition means that gaze lags behind finger position.

the oblique orientation (circles). We did not find a significant difference (Mann-Whitney *U* test, $p = 0.34$).

When saccades are involved in eye-hand coordination like in tracing, the time of the peak of the cross-covariance function depends on the fixation time between saccades and may depend on the velocity of tracing. In order to investigate this in detail, figure 2.6b shows the same data as in figure 2.6a, but lead times of trials with the helices as stimulus shape are included as well. Different gray symbols refer to data from different subjects. For the y- and z-directions (frontal plane) there is a significant correlation between lead time and tangential finger velocity ($r = -0.72$, $p < 0.01$, figure 2.6b, upper panel). This correlation is not significant in depth ($p = 0.91$, figure 2.6b, lower panel). Thus, a lower tracing velocity of the finger results in a larger lead time of gaze with respect to finger for the frontal plane, but not for the depth direction. The mean gaze-finger lead time is 287 ms (SE 13 ms, $n = 84$) in the frontal plane and 151 ms (SE 36 ms, $n = 28$) in depth (figure 2.7). The difference between the lead times in the frontal plane and depth is significant ($p < 0.01$).

These results for tracing are different from the results obtained for tracking. For tracking, we calculated the lead time of gaze relative to finger position, of target relative to

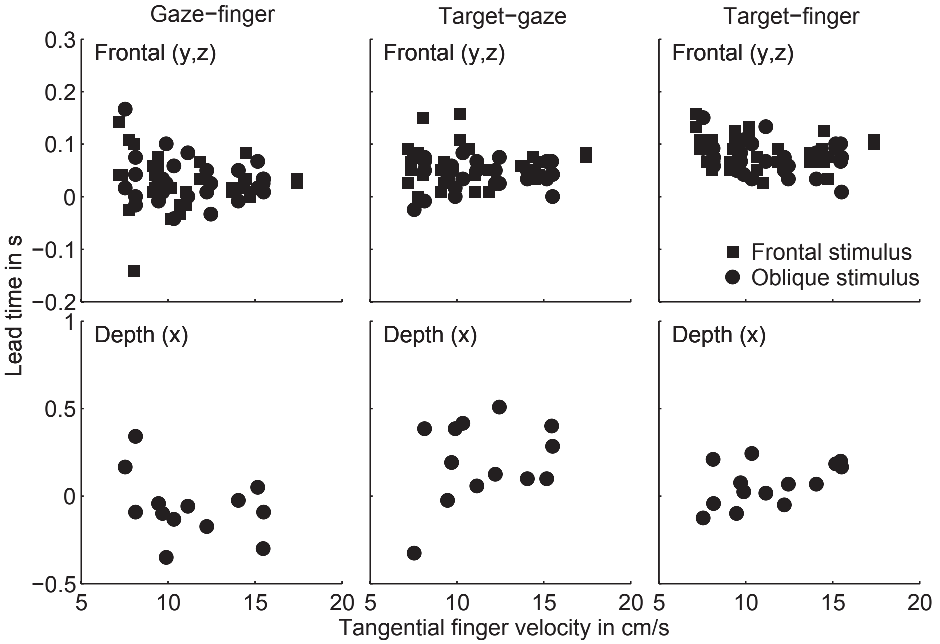

Figure 2.8 Lead times in the tracing condition. Time of the peak of the cross-covariance function between gaze and finger position (first column), target and gaze position (second column), and target and finger position (third column), as a function of the mean tangential finger velocity in each trial for the tracking condition. The upper and lower row show values for the frontal directions (*y* and *z*) and the depth direction (*x*), respectively. Squares and circles represent data for the frontal and oblique orientations, respectively, for the Cassini and Limaçon shapes.

gaze position, and of target relative to finger position, in the frontal and the depth direction, see figure 2.8. We subdivided the lead times in the frontal plane into trials for shapes in the frontal orientation (squares in figure 2.8) and in the oblique orientation (circles). Since we did not find a significant difference between frontal and oblique stimulus orientation (Mann-Whitney U test, $p > 0.1$) for all three lead times, data for both stimulus orientations were pooled. We calculated the correlation between the lead time of gaze relative to finger and mean tangential finger velocity for the frontal and depth directions. For both directions, this correlation was small and did not appear to be significant ($r = -0.12$, $p = 0.37$ for the frontal direction and $r = -0.35$, $p = 0.22$ for the depth direction). We also calculated the lead times averaged over all trials and subjects for the frontal and the depth direction. In the tracking condition, gaze and finger lag behind the moving target. For gaze, the mean delay is 51 ms (SE 4 ms, $n = 60$) in the frontal plane and 140 ms (SE 57 ms, $n = 14$) in depth. For the finger, the mean delay is 80 ms (SE 4 ms, $n = 60$) in the frontal direction and 67 ms (SE 22 ms, $n = 14$) in depth. As a result, gaze leads the finger on average by 28 ms (SE 6 ms, $n = 60$) in the frontal plane, but lags behind the finger by 95 ms (SE 39 ms, $n = 14$) in depth. The mean lead times of gaze relative to the finger in the tracking condition are significantly different from the mean lead times in the tracing condition ($p < 0.01$) both for the frontal and depth components (figure 2.7). In the *Discussion*, we will further elaborate on these findings.

Table 2.1 Saccadic lead times in milliseconds calculated as the difference between total lead time and primary lead time (method I) and obtained from fixation times according to equation 2.5 (method II). Values are given as mean ± SD over all tracing trials.

Subject	Method I	Method II
S1	93±50	119±29
S2	123±18	172±61
S3	125±56	149±21
S4	107±20	146±23
S5	142±27	169±23
All subjects	121±39	154±37

Effect of saccades on gaze-finger timing In the previous section we have shown that the lead time between gaze and finger position for tracing is on average 287 ms in the frontal direction (figure 2.7) and that this lead time varies with tangential finger velocity in the frontal plane (figure 2.6b, upper panel). Moreover, the mean lead time for the frontal direction is significantly different from the value for depth (151 ms, figure 2.7). In this section, we will investigate the effect of saccades on the relative timing of gaze and finger position.

As illustrated in figure 2.3 we hypothesize that the lead time of gaze relative to the finger in the frontal direction in the tracing condition is a combination of a saccadic lead time and a primary lead time. To test this hypothesis, we interpolated all saccade onsets with a cubic spline, as illustrated in figure 2.3c. Next, we calculated the mean gaze-finger lead time from the cross-covariance between the spline function and finger position for the frontal direction. The results are shown by the symbols in figure 2.6c. Different symbols refer to data from different subjects. Figure 2.6c gives the primary lead time as a function of tangential finger velocity in the frontal plane. The mean value for the primary lead time is 166 ms (SE 12 ms), which is significantly smaller (Mann-Whitney *U* test, $p < 0.01$) than the total mean lead time (287 ms; figure 2.6b, upper panel) of gaze relative to finger in the tracing condition. The correlation between primary lead time and finger velocity is significant ($r = -0.61$, $p < 0.01$).

In the previous section we found that the gaze-finger lead time in depth is 151 ms (SE 36 ms), which is significantly different from the total lead time of 287 ms (SE 13 ms) in the frontal direction (first two bars in figure 2.7). However, after correction for the saccadic lead time, the mean primary lead time in the frontal direction is 166 ms (SE 12 ms), which is not significantly different from the mean lead time in depth (Mann-Whitney *U* test, $p = 0.71$).

The difference between total lead time (figure 2.6b) and primary lead time (figure 2.6c) corresponds to the saccadic lead time (method 1). Table 2.1 shows the saccadic lead time in ms. Values are given as mean (SD) over all tracing trials. The saccadic lead time for the five subjects ranges from 93 to 142 ms. Figure 2.9 shows the histograms of the fixation times for all trials per subject (S1-S5), as well as the distribution of fixation times for all subjects. The solid and dashed line in each histogram indicate the median and mean value, respectively. The median fixation times for the five subjects range from 233 to 267 ms. As explained in the *Methods* section, the saccadic lead time is related to the length of the fixations in a trial (equation 2.5). As a check for consistency, we have also calculated the saccadic lead time from the individual fixations in each trial according to equation 2.5 (see table 2.1, method

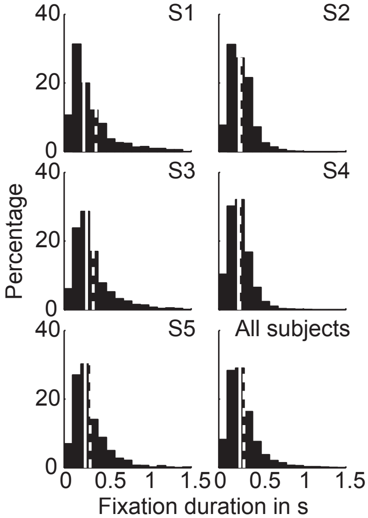

Figure 2.9 Fixation durations. Distribution histograms of the fixation times for subject S1–S5, and across all subjects. Values are obtained from individual fixations of each tracing trial. Solid and dashed lines indicate the median and mean value over all values in the histogram, respectively. The distribution of fixation times is given as a percentage of the total number of fixations.

2). For this method, the saccadic lead time for the five subjects ranges from 119 to 169 ms, which is larger than the corresponding lead times found by method 1. This difference is significant (Mann-Whitney U test) for subjects S2, S4, S5 and for all subjects pooled. We will give an explanation for this difference in the *Discussion*.

The general notion in the literature is that gaze leads finger position in time. Our null-hypothesis was that this lead time should be constant and independent of velocity of the finger. Yet, after correction for the saccadic lead time, we still find a significant negative correlation between the gaze-finger lead time and mean finger velocity. The data in figure 2.6c suggest an inverse relationship between lead time and tangential finger velocity. This inverse relationship is qualitatively in agreement with the hypothesis that gaze leads finger position by a constant displacement. This predicts $\tau_0 = \Delta s/v$, where τ_0 is the primary lead time, Δs the mean lead distance of gaze relative to finger position, and v the tangential finger velocity.

To test the hypothesis that gaze leads the finger by a constant displacement we fitted the relation $\tau_0 = \Delta s/v$ to the data in figure 2.6c by varying Δs. The best fit over all subjects for the primary lead time is shown by the solid line in figure 2.6c and corresponds to a mean lead distance of 2.6 cm (SD 0.1 cm). Fits for each subject separately, reveal that the range of lead distances is between 1.5 and 3.5 cm (table 2.2, method I).

Another method to determine the mean lead distance of gaze relative to finger is to calculate $\Delta s = v\tau_0$ using the primary lead time and the mean tangential velocity of each trial. The results demonstrate that the mean lead distance of gaze relative to finger position in the frontal plane for the tracing condition is 2.6 cm (SD 1.4 cm) with a range between 1.7 and 3.6 cm for all subjects (table 2.2, method II). For subjects S2, S4 and S5, and for the pooled dataset, the lead distance found by this method is close to the value obtained by

Table 2.2 Lead distance of gaze relative to finger position in cm computed as: (I) the best fit of $\tau_0 = \Delta s/v$ (SD obtained by bootstrap procedure with $n = 100$); (II) the product of finger velocity v and primary lead time τ_0; and (III) the distance between gaze and finger position at each saccade onset. Values are given as mean ± SD (median).

Subject	Method I	Method II		Method III	
S1	2.2±0.3	2.5±1.0	(2.6)[a]	3.8±2.5	(3.1)[b]
S2	1.5±0.2	1.7±1.0	(1.6)	2.9±2.3	(2.2)[b,c]
S3	1.5±0.2	1.8±1.7	(1.5)	3.0±1.9	(2.6)[b,c]
S4	2.9±0.2	3.3±0.8	(3.3)[a]	4.2±2.5	(3.9)[b]
S5	3.5±0.1	3.6±0.6	(3.6)	3.7±2.3	(3.3)
All subjects	2.6±0.1	2.6±1.4	(2.7)	3.6±2.4	(3.1)[b,c]

[a,b,c] Significant difference ($p < 0.05$) between the lead distance distribution obtained by methods I and II, methods I and III, and methods II and III, respectively.

the best fit to the data (method I) and is not significantly different from the value obtained by the best fit.

Alternatively, the lead distance is obtained directly by calculating the distance between gaze and finger position at each saccade onset for all tracing trials. The median lead distance obtained by this method has a range between 2.2 and 3.9 cm (table 2.2, method III). Compared to method II, method III gives significant differences for subject S2 and S3, and for the pooled dataset. Compared to the value obtained by the best fit (method I), method III yields significantly different results for the mean lead distance for all subjects, except subject S5. The median values obtained by method III are smaller (range 2.2–3.9 cm) than the mean values (range 2.9–4.2 cm; see *Discussion*). The analyses indicate that not lead time, but lead distance is approximately constant, resulting a lead time which is inversely proportional to the finger velocity.

2.4 Discussion

The dynamics of saccades and smooth pursuit, which are involved in the control of gaze in the frontal plane, are very different from that of the vergence system. This led us to suggest that the lead time of gaze relative to the finger is different in the frontal plane and in depth. Our results revealed that the lead time of gaze relative to the finger was not constant for tracing but inversely related to tangential velocity of the hand. The lead time is relatively large (about 500 ms) for small velocities and decreases to about 200 ms for finger velocities of about 30 cm/s (figure 2.6b). After correction for a saccadic lead time, the remaining lead time still decreases inversely with finger velocity (figure 2.6c). Our results can be explained by assuming that gaze leads finger position by a constant distance of about 2.6 cm.

The lead time of gaze relative to the finger was obtained from the cross-covariance between gaze and finger position. Since the lead time of gaze varied with tangential velocity, and since the tangential velocity varied along the Cassini and Limaçon shapes, the peak of the cross-covariance reflects the mean lead time over a range of velocities in a trial.

For tracing, the gaze-finger lead time has two components: a saccadic and a primary lead time. The saccadic lead time reflects the contribution of saccades to the total lead time and therefore depends on the fixation time between saccades. We estimated the saccadic lead time by taking the difference between total lead time and primary lead time (method 1) and from the individual fixation times according to equation 2.5 (method 2). The values found by method 2 are larger than for method 2, see table 2.1. This difference can be explained by considering figure 2.3a. In this figure, the fixation end points (or saccade onsets) are located exactly at the finger position curve (black line). However, in general the fixation end points will not perfectly superimpose on the finger position time trace because of measurement errors, motor noise and limited pointing accuracy of the subject. As a consequence, the fixation duration of a particular fixation will be slightly shorter or longer compared to the hypothetical situation in figure 2.3a. Assuming that the difference between the measured and hypothetical fixation time is $\pm\epsilon$ with equal probability, equation 2.5 becomes

$$\tau_{sac} = \frac{1}{2}\frac{\sum_i (t^i_{fix} \pm \epsilon)^2}{\sum_i (t^i_{fix} \pm \epsilon)} = \frac{1}{2}\frac{\sum_i (t^i_{fix})^2 + N\epsilon^2}{\sum_i t^i_{fix}} \tag{2.6}$$

with N the number of fixations. This equation shows that the saccadic lead time estimated from detected fixations is biased toward larger values (due to the term $N\epsilon^2$). However, the noise does not affect the value of the saccadic lead time obtained by cross-covariance (method 1). Thus, method 1 and 2 give the same results only if the fixation end points exactly superimpose on the finger position (figure 2.3a) or on the finger position shifted in time (figure 2.3c). If not, method 2 will yield systematically larger saccadic lead times than method 1.

The distribution of measured fixation times (figure 2.9) reveals a sharp peak for values less than 250 ms with a mean value exceeding 250 ms. For all subjects, the mean value exceeds the median value. This can be attributed to the fact that fixation times can only be positive. Therefore, any outliers correspond to large positive values, which implies that the mean value is biased towards larger values. This positive bias also affects the median value, but to a smaller extent.

Another consideration is that finger velocity and saccade interval might be related. For example, a higher movement velocity might imply a more rapid sequence of saccades with shorter intervals. If so, the inverse correlation between lead time of gaze and finger velocity might be an artifact of the inverse correlation between finger velocity and fixation time. To investigate this in more detail, we calculated the correlation between finger velocity and fixation duration for each subject. This correlation appeared to be small (range 0 to -0.3). In addition, we did not find a significant correlation between mean fixation interval and mean finger velocity ($p > 0.3$). Finally, the mean finger velocity was not significantly correlated to the number of saccades per second. Therefore, we conclude that our result of an inverse relation between lead time and tangential hand velocity is not an artifact of a hidden correlation between hand velocity and saccade frequency.

The results in figure 2.7 show that the mean lead times for tracking of gaze relative to the finger (28 and -95 ms for the frontal plane and depth, respectively) are much smaller than the corresponding lead times for tracing. In addition, figure 2.5 shows that gaze position deviates from the stimulus shape more for depth than for direction in the tracing condition. This is not due to an erroneous percept of stimulus depth. The almost perfect match between stimulus position, gaze and finger position for tracking indicates that subjects perceive the anaglyph stimulus quite well. Since the complete stimulus is visible in the tracing condition, it is highly unlikely that the percept of the stimulus path is inferior in the tracing condition. The less accurate match between stimulus path and gaze position in depth is in agreement with previous studies (Admiraal et al., 2003, 2004), which have shown that fixation accuracy on targets is less when visual information is available on target position relative to the environment, especially for the depth component. Moreover, Gonzalez et al. (1998) reported that the perceived depth of random dot stereograms is not affected by vergence, which suggests that imperfections of gaze in depth do not affect the accuracy of pointing in depth.

After correction for the saccadic lead time, we found a mean primary lead time of gaze relative to the finger in the frontal plane, which is close to the lead time for depth (166 ms and 151 ms, respectively). This might suggest that the underlying mechanisms may be similar. This is not true since the lead time of gaze varies with tangential finger velocity in the frontal plane, but not for depth. Moreover, the different results for tracking (i.e., a lead time of gaze of 28 ms in the frontal plane, but a lag of 95 ms in depth) suggest different mechanisms for tracking in the frontal plane and in depth.

Our results clearly demonstrate differences in the coordination of gaze and finger position for the frontal plane and depth. There is some evidence from the literature supporting this result. For example, several studies have demonstrated that direction and depth are processed separately as independent variables during updating across eye movements (Ghez et al., 1997; Henriques et al., 1998; Van Pelt and Medendorp, 2008) . Moreover, there is evidence that target depth and direction are processed in functionally distinct visuomotor channels (Flanders et al., 1992; DeAngelis, 2000; Cumming and DeAngelis, 2001; Vindras et al., 2005). Another difference is that gaze leads finger position in the tracking condition by 28 ms in the frontal plane, but lags behind the finger in depth by 95 ms. Although the lag between target and gaze depends on the predictability of the moving target (Collewijn and Tamminga, 1984), it seems highly unlikely that anticipation or predictability would be different for the frontal plane and for depth. It is also highly unlikely, that the velocity of the moving target or the finger velocity (typically less than 30 cm/s, corresponding to about 15 deg/s in this study) is too fast for the vergence system to track. This follows from results by Erkelens et al. (1989), who showed that errors between gaze and a moving target are less than 1 deg in the depth direction for movement velocities in the range between 10 and 40 deg/s. Therefore, we conclude that the different lead time of gaze relative to the finger for the frontal plane and for depth reflects differences in the dynamics of visuomotor control for version and vergence.

The results of our study suggest that feed-forward and (internal) feedback transformations, that are thought to be part of the servo-control system for eye-hand coordination (Wolpert et al., 1995), should not only deal with time delays in internal and sensory feedback loops, but also with spatial aspects. The latter seems obvious, but our study is the first that demonstrates that the visuomotor transformations generate a constant lead of gaze in space by about 2.6 cm. This distance is relatively small, and may be a compromise between a distance, which is small enough to have a sharp percept of target and finger position and long enough for planning the finger trajectory. If the aim is to lead the finger such that both the target and finger position are sharply represented on the retina, then it might be retinal eccentricity, rather than distance in space which is relevant. In that case the distance of 2.6 cm, which corresponds to about 2 deg in our study, will become smaller or larger if the distance of the stimulus shape is nearer or further away, respectively.

3

Gaze is driven by an internal goal trajectory in a visuomotor task

J.J. Tramper
A. Lamont
M. Flanders
C.C.A.M. Gielen

Published in *European Journal of Neuroscience*, 2012, doi: 10.1111/ejn.12107

3.1 Introduction

When subjects make hand movements to visual targets, gaze usually leads hand position by a series of saccades to task-relevant locations (Flanagan and Johansson, 2003; Hayhoe et al., 2003; Land et al., 1999; Neggers and Bekkering, 2001). In addition to saccades, smooth pursuit eye movements also contribute to these gaze changes to targets of interest. Smooth pursuit is classically regarded as an automatic feedback system, driven by retinal slip (Lisberger, 2010). However, increasing evidence suggests that the input to the smooth pursuit system is not just retinal slip. For example, anticipatory smooth eye movements can be cued in the direction of an upcoming stationary target (Blohm et al., 2005; Kowler and Steinman, 1979a,b) or moving target (Barnes, 2008; De Hemptinne et al., 2008). Moreover, pursuit is maintained when the target is temporarily occluded (Becker and Fuchs, 1985; Mrotek and Soechting, 2007), suggesting input from a short-term velocity memory to smooth pursuit (Orban de Xivry et al., 2008). In a study of Vercher et al. (1995), subjects had to track a visual target that was moved by their own, unseen arm. When the target unexpectedly moved opposite to the arm, smooth pursuit initially followed the direction of the arm rather than the visual target, suggesting that the initial pursuit could be driven by an efference copy related to the arm movement (Lazzari et al., 1997; Scarchilli et al., 1999). Gardner and Lisberger (2001) showed that the choice of which moving target to follow in smooth pursuit is coupled to the choice of the saccadic system. This raises the possibility of a cognitive input to the smooth pursuit system, in a situation where pursuit is interleaved with a series of saccades.

Recently, we showed that subjects fixate at a particular distance ahead of the hand when they move the hand along a well-defined path (Tramper and Gielen, 2011). This lead distance might reflect a compromise between exploring the future path and verifying that the hand moves along the path. We hypothesized that a similar mechanism might be active when subjects use a combination of saccades and smooth pursuit to guide their hands toward a goal in a complex environment. To investigate the role of saccades and smooth pursuit when subjects create their own internal representation of a future trajectory, we designed a video-game task in which subjects used their thumbs to move two cursors through two gates toward a final goal. The two cursors may facilitate a target selection mechanism for the smooth pursuit system. The stationary visual targets (gates and goal) served as possible targets for the saccadic system. As expected, this task elicited a series of saccades to sequentially fixate the stationary visual targets. In addition, we discovered a range of smooth eye velocities between saccades, when gaze was well ahead of the cursor positions. Gaze velocities during these segments were unrelated to the velocities of the cursors, suggesting that smooth pursuit was driven by some internal representation of the future cursor paths.

3.2 Methods

Subjects Six subjects (S1–S6) with ages between 22 and 27 years participated in this study. S3, S4 and S6 were male. All subjects were right-handed and none of them had any known neurological disorder. S1–S6 participated in experiment 1 and S1–S4 also participated in experiment 2 (see below). One subject (S4) was aware of the purpose of the experiment, whereas the others were naive. S3 and S6 had extensive experience with video games that use game controllers (S3 (age 22), 1–2 hours a day since age 20 years; S6 (age 24 years), 1–2 hours from childhood to age 17 years); the other subjects had no substantial experience. The study conformed the Code of Ethics of the World Medical Association (Declaration of Helsinki), printed in the *British Medical Journal* (18 July 1964). All subjects gave written informed consent prior to the start of the experiment, according to the institutional guidelines of the local ethics committee (CMO Committee on Research Involving Human Subjects, region Arnhem-Nijmegen, the Netherlands).

Experimental setup Subjects were seated in a chair with a high backrest in front of a $1.5 \times 1.1\text{-m}^2$ rear-projection screen in a completely darkened room. The subject's eyes were positioned at a distance of ~90 cm to the screen. The height of the chair was adjusted to align the subjects cyclopean eye with the center of the projection area. Head movements were restrained by a chin rest fixed to the chair.

Two-dimensional visual scenes were rear projected on the screen with a 3D-ILA SXGA projector (JVC DLA-S15U) with a refresh rate of 75 Hz. The scenes were generated by Open Graphics Library (OpenGL) with the Psychophysics Toolbox for Matlab. The exact distance between the subjects cyclopean eye and the screen was measured before each experiment, to adjust the size of the computer generated scene to a field-of-view of 45 deg in both the azimuth ϕ (horizontal) and elevation θ (vertical) directions.

Eye movements were recorded using the double magnetic induction (DMI) method (Bour et al., 1984; Bremen et al., 2007) and sampled at 1000 Hz using an NI PCI-6220 (National Instruments, Austin, Texas, USA) data acquisition card. To use the DMI method, the subject was seated in the center of a primary oscillating magnetic field with three orthogonal components with different oscillation frequencies, generated by a $3 \times 3 \times 3\text{-m}^3$ cubic frame. A gold-plated copper ring was placed on the subjects eye. A pick-up coil was placed in front of the eye in the frontal plane, and an 'anticoil' was connected antiparallel to the pick-up coil to cancel the contribution of the primary field. In this way, the pick-up coil only detected the secondary magnetic field generated by eye-orientation-dependent currents in the copper ring. The DMI method was chosen over the scleral search coil technique because subjects experience less discomfort wearing the ring than when wearing a scleral coil, which needs a wire to connect with the recording apparatus. After calibration, a precision of ~0.2 deg was achieved for both azimuth and elevation over a range of 45 deg.

Each subject held a wireless game controller (Microsoft XBOX 360 Wireless Controller for Windows) consisting of two thumb sticks to move two cursors in the scene by making thumb movements. The velocity of each of the cursors was proportional to the excursion of the corresponding thumb stick, which could be moved in all directions. The maximum cursor velocity in both the azimuth and elevation direction was 39.7 deg/s.

Experiment In experiment 1, S1–S6 were asked to move the left and right cursors, displayed as left-hand and right-hand icons, through two gates towards a final common goal, using the two thumb sticks on the game controller. Figure 3.1a gives a rough schematic of the game, with black and white reversed and objects not drawn to scale. We call the geometric arrangement of the gates and the goal the 'scene'. To successfully complete a trial, subjects had to reach the goal within 3 s while moving the left and right cursors

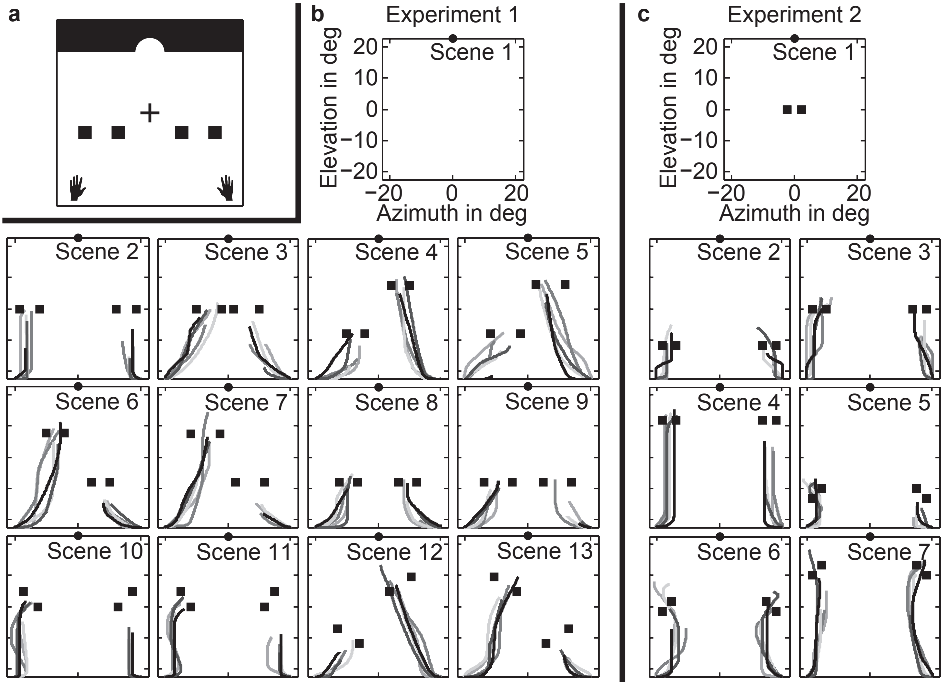

Figure 3.1 **(a)** Schematic of the video-game display, with left and right gates represented by pairs of squares, and a final common goal represented by an opening in a virtual wall at the top of the display. The black hand icons represent the initial position of the left and right cursors, respectively. The cross represents the location of initial gaze fixation. Icons are not to scale, and the screen background was black, not white, with gray objects. **(b)** Location of gates and goal of each scene for experiment 1. Each scene had a field-of-view of 45 deg, with azimuth and elevation running from –22.5 to 22.5 deg and consisting of one final goal (circle). Scenes 2–13 included two gates (squares) located at various positions. In scene 1, no gates were present. The size of the gate openings were 4.2 deg (scene 2), 6.2 deg (scene 3), 3.8 deg (scenes 4, 6, 8, 11), 7.2 deg (scenes 5, 7, 9), 4.6 deg (scene 10), and 6.6 deg (scenes 12, 13). Icons are not to scale. Each pair of lines with the same grayscale represents the left and right cursor trajectories of a single trial, for S2. Traces only show the trajectory between movement onset of the left (right) cursor until the time when gaze moved away from the left (right) gate. **(c)** Same as (b) for experiment 2. In scene 1, only one gate was present; scenes 2–7 included two gates. The size of the gate openings was 2.5 deg in all scenes.

through the left and right gates, respectively. In this way, we created a highly demanding visuomotor task, as vision had to be allocated carefully to observe the scene and guide both cursors through the gates within a very short time.

We presented thirteen different scenes: twelve gate scenes and one no-gate scene (figure 3.1b). Each scene had a black background and consisted of a goal represented by an opening in a virtual white wall with a width of 7.5 deg and located at $(\phi, \theta) = (0, 22.5)$ deg. Each gate was formed by a pair of gray squares, and the size of each square was 1.9 deg × 1.9 deg. The size of the gate openings were 4.2 deg (scene 2), 6.2 deg (scene 3), 3.8 deg (scenes 4, 6, 8, 11), 7.2 deg (scenes 5, 7, 9), 4.6 deg (scene 10), and 6.6 deg (scenes 12, 13).

Each trial started with a white fixation cross (size 0.4 deg) displayed at the center of the black screen, and the gates were invisible. The cursors had the shape of a left and right hand icon (size 2.1 deg × 2.5 deg and gray color) and were displayed at $(-20.5, -22.5)$ deg and $(20.5, -22.5)$ deg, respectively. Subjects were asked to fixate the cross until they moved one of the cursors, which caused the fixation cross to disappear and the gates to appear. No instructions on eye movements were given for the remaining part of the trial. When either cursor hit a gate obstacle (displayed as a square on the screen) or the upper boundary of the scene ($\theta = 22.5$ deg), the cursor stopped moving.

The experiment was divided into six blocks with 65 trials each. The position of the two gates changed on every trial, randomly selected from the set of thirteen different scenes, yielding 30 repetitions for each scene. To calibrate the eye movement signals, each block was preceded by a calibration trial in which subjects fixated on 36 calibration points, sequentially presented in a grid. The experiment started with instructions and one block of 65 practice trials to enable the subject to become familiar with the controller and the task (duration 5 min), and this was followed by the application of the DMI equipment (eye ring and pickup-coil, 3 min), the first calibration trial (1 min), the first block of trials (3.5 min), until all six blocks were completed. Each experiment took approximately 30 min in total.

In experiment 2, we tested S1–S4 in a different set of seven scenes (figure 3.1c). One scene consisted of a single gate located at $(\phi, \theta) = (0, 0)$ deg, and both cursors had to pass through that gate. The size of the gate openings was 2.5 deg. This experiment was divided into six blocks with 70 trials each. The position of the two gates changed on every trial, randomly selected from the set of seven different scenes, yielding 60 repetitions for each scene. All other experimental conditions were exactly the same as for experiment 1. The purpose of experiment 2 was to create a more difficult task by making smaller gate openings, thereby increasing the visual demand and requiring more accurate maneuvering of the cursors. This allowed us to investigate to what extent the results were influenced by the difficulty of the task.

Data preprocessing Eye position was calibrated with a parameterized self-organizing map (PSOM) (Essig et al., 2006). We adapted this method to make it suitable for calibration of gate position in the two-dimensional plane. The 36 calibration points were arranged in a Chebyshev-spaced grid to increase the calibration performance (Walter and Ritter, 1995). A trial was completed correctly if each of the following three criteria was met: (i) each cursor was navigated through its corresponding gate; (ii) each cursor reached the goal before the deadline of 3 s; (iii) the vertical cursor velocity was always positive (moving upwards) and larger than zero, except for the beginning and end of the trial. The last criterion was included to ensure that subjects moved each cursor in a smooth fashion without hitting one of the gate obstacles or going backwards. Figure 3.2a shows the percentage of correctly completed trials. Only correctly completed trials were used for further analyses.

Event detection We used an adaptive algorithm developed by Nyström and Holmqvist (2010) to classify gaze epochs as a fixation or a saccade. This algorithm uses a data-driven approach based on the signal-to-noise ratio to find the saccade onset and end thresholds, instead of predetermined parameters set by the user. As the noise in the raw voltage signals differed among subjects, owing to the exact placement of the DMI equipment, this method improved the event detection. We made the following adjustments to the algorithm. We set the initial peak velocity threshold for saccade onset to 80 deg/s, the minimum saccade duration to 10 ms and the minimum fixation duration to 50 ms. The

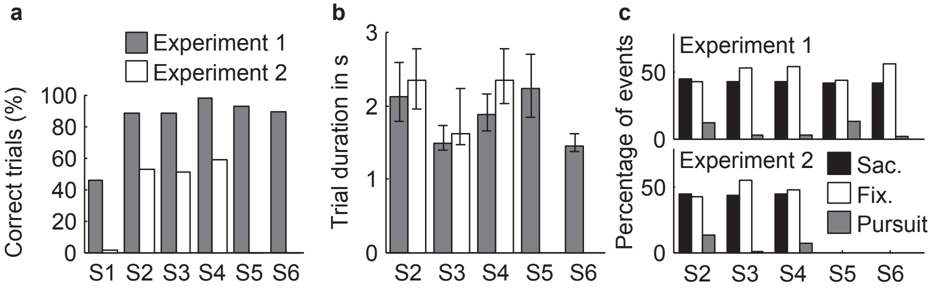

Figure 3.2 Task performance and classification of eye movements. **(a)** Percentage of trials completed correctly for S1–S6 for experiment 1 (gray) and for S1–S4 for experiment 2 (white). **(b)** Median trial duration for S2–S6 for experiment 1 (gray) and for S2–S4 for experiment 2 (white). Lower and upper error bars indicate the 5% and 95% percentiles, respectively. **(c)** Total percentage of saccades (black), fixations (white) and smooth pursuit segments (gray) in all scenes for for S2–S6 in experiment 1 (top panel) and for S2–S4 in experiment 2 (bottom panel).

maximum saccade velocity and maximum saccade acceleration were excluded as selection criteria. We extended the algorithm to also detect smooth pursuit. Therefore, we took all epochs which were initially classified as a fixation, and for each epoch we smoothed gaze velocity using a Savitzky-Golay filter with a span of 100 ms and order 2. Within that epoch, a series of subsequent data points was labeled as a smooth pursuit epoch if: (i) the gaze velocity in the elevation direction exceeded 3 deg/s; (ii) the gaze displacement was larger than 1 deg of visual angle; and (iii) the duration was larger than 50 ms. The remaining data points in the epoch were labeled as a fixation if the duration exceeded the minimum fixation duration. Otherwise, the remaining data points were merged with the smooth pursuit epoch.

3.3 Results

Overall performance As subjects had to maneuver two cursors via two gates to a final common goal at the top of the screen within 3 s and without hitting the gates, success rates varied across subjects. As indicated in figure 3.2a, S1 had great difficulty in both experiments, with only ~40% of trials being successfully completed in experiment 1 and almost no successful trials in experiment 2. This subject was therefore excluded from further analysis. The values for successful completion for the other subjects were, on average, 92% (range 89–98%) for experiment 1 and 54% (51–59%) for experiment 2, which confirmed that experiment 2 was more difficult. S2 and S5 tended to use more time to complete each trial (>2 s), especially compared with S3 and S6, who had an average trial duration of ~1.5 s (figure 3.2b).

Gaze data were analyzed by detecting saccades, and then classifying non-saccade segments as fixation or smooth pursuit (figure 3.2c). The subjects with longer trial durations generally had a larger number of smooth pursuit events, which constituted ~23% of all non-saccadic segments in S2 and S5, as compared with ~5% in the other subjects (figure 3.2c).

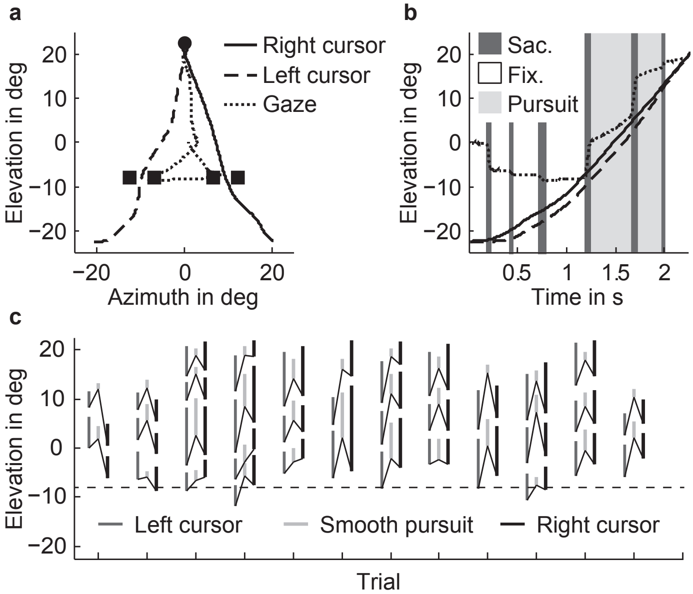

Figure 3.3 **(a)** Left cursor (dashed line), right cursor (solid line) and gaze (dotted line) paths for a single trial (S2, scene 8, experiment 1). The goal and gates are represented by the circle and squares, respectively. **(b)** Corresponding time traces in the elevation direction for gaze (dotted line), left cursor (dashed line), and right cursor (solid line). Shaded areas indicate either fixations (white), saccades (dark gray) or smooth pursuit (light gray). **(c)** Elevation position of smooth pursuit paths for trials of scene 8, experiment 1, shown as light gray lines (S2). The dark gray and black lines show the elevation position of the left and right cursor, respectively, in the same time frame as the corresponding smooth eye movement (light gray bar). The dashed line indicates the elevation position of the gates.

Figure 3.3a and b shows an example of a single trial where the first four non-saccade segments were classified as fixation, the next two segments were classified as smooth pursuit (figure 3.3b), and the last segment was classified as a fixation. In the last phase of the trial, after passing through the gates (after ~1.2 s), each cursor moved at a more or less constant velocity. In contrast, the smooth pursuit velocity was higher in the first smooth pursuit segment (between 1.3 and 1.7 s) than in the second (1.7–2.0 s; figure 3.3b). In general, gaze position was leading the position of the cursors throughout the entire movement (figure 3.3b). Smooth pursuit eye movements almost always occurred between the gates and the target, as indicated by the vertical light gray bars that are located above the dashed line in figure 3.3c, which represents the position of the gates. The thin solid lines in figure 3.3c connect the corresponding positions of the left and right cursors at the time of onset of pursuit. The segment of pursuit is always smaller than the segments of corresponding cursor movements, as pursuit velocity was much smaller than cursor velocity (figure 3.3b). At the onset of pursuit, the cursor positions were lagging behind the smooth eye movement. These observations are representative for all subjects and we will elaborate on each of these aspects in the following sections.

Saccade metrics In this section, we will investigate the extent to which saccadic eye movements and cursor movements are coupled. In figure 3.1b and c, showing trial data from S2, each pair of lines with the same gray scale represents the left and right cursor paths of a single trial. The traces only show the paths between movement onset of the left (right) cursor until the time when gaze moved away from the left (right) gate. For asymmetric scenes, such as scenes 6 and 7 of experiment 1 (figure 3.1b), gaze visited the lower gate first, and then moved away well before the cursor reached it. Thus, the right cursor paths in scenes 6 and 7 are truncated well beneath the right gate. However, gaze generally departed from the second gate around the time the cursor reached the gate. The same was true for symmetric scenes, except that, in this case, as there was no lower gate, the eye may have visited either the left or the right gate first. This behavior was consistent across the original experiment (experiment 1) and the more difficult experiment (experiment 2), and this strategy was similar across subjects.

For all scenes, the time when the cursor entered the gate and the time when gaze left that gate was correlated (Pearson's correlation coefficient $r = 0.68$, standard deviation (SD) 0.17, $p < 0.03$ for each scene). To investigate whether gaze was leading or lagging behind the cursors, we computed the time difference between the time when gaze left the gate and the time when the cursor entered the gate. A positive value means that gaze left the gate before the cursor entered the gate. Pooling data over all subjects, scenes, and experiments we found an average time difference of 122 ms (SD 235 ms). We then subdivided the scenes of experiment 1 according to the arrangement of the gates. For symmetric scenes, we found a time difference of 336 ms (SD 240 ms) for the gate that gaze visited first and a time difference of 42 ms (SD 138 ms) for the second gate. The values for experiment 2 were 203 ms (SD 236 ms) and –11 ms (SD 145 ms) for the first and second gate, respectively. The time differences for experiment 2 were significantly different from experiment 1 (two-tailed two-sample t test, first gate, $p < 10^{-18}$; second gate, $p < 10^{-8}$), which shows that the lead time between gaze and cursors decreased in the more difficult situation when the cursors had to pass smaller gates.

For the asymmetric scenes in experiment 1, we found a time difference of 125 ms (SD 166 ms) for the first gate and a time difference of 27 ms (SD 139 ms) for the second gate. The difference between symmetric and asymmetric scenes from experiment 1 was significant for the first gate (two-tailed two-sample t test, $p < 10^{-51}$) but was not significant for the second gate ($p = 0.09$). Thus, the relative timing between gaze and cursors was dictated by scene geometry (symmetric versus asymmetric arrangements of the gates) as well as gate geometry (small versus large gate openings).

Saccade endpoints were generally ahead (positive elevation) of cursor location. This was true for all subjects, both cursors, and both experiments (figure 3.4, top row). We also considered separately the saccade endpoints that were interleaved between gaze segments classified as smooth pursuit (figure 3.4, bottom row). S3 and S6 (the subjects with short trial durations) had relatively few of these events, but it is still clear that the endpoints of these saccades were generally ~5 deg above cursor location. This result corresponds to our previous observations on pursuit location in figure 3.3c.

Smooth pursuit As the endpoints of saccades that were interleaved with smooth pursuit (figure 3.4, bottom row) correspond to the location of smooth pursuit onset, the results in figure 3.4 demonstrate that not only the saccades, but also the segments of smooth pursuit,

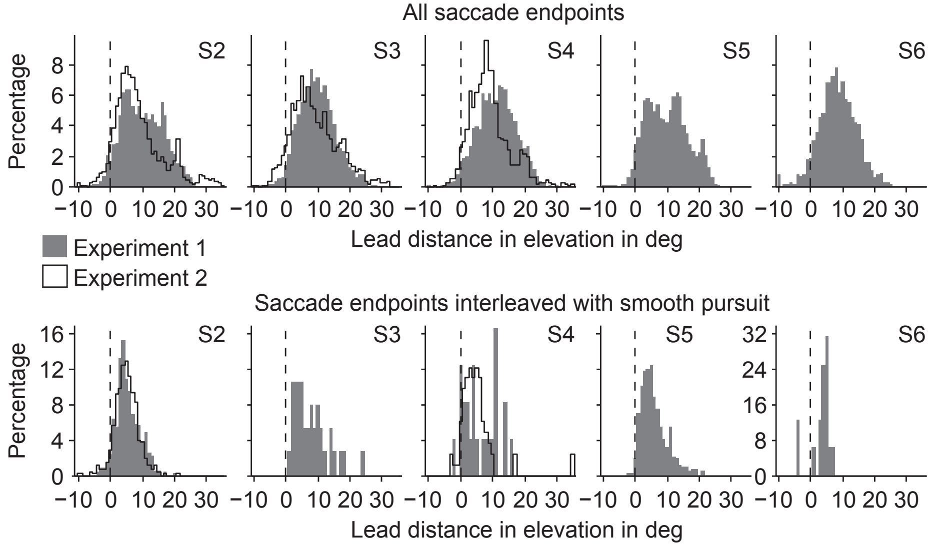

Figure 3.4 Saccade endpoints are ahead of cursor location. Histograms are shown of lead distances in the elevation direction for S2–S6 in experiment 1 (gray bars) and for S2–S4 in experiment 2 (black line). For each saccade, the lead distance was calculated as the elevation of gaze position minus the elevation of cursor position at the end of a saccade. Data for left and right cursors were pooled. The dashed lines mark the lead distance of 0 deg. The top row shows data for all saccade endpoints. The bottom row shows data for saccade endpoints for saccades that were interleaved with smooth pursuit eye movements. S3 did not show saccades interleaved with smooth pursuit in experiment 2.

started ahead of the cursor location. Thus, gaze position during smooth pursuit did not match the location of one of the cursors. This raised the question of whether smooth pursuit velocity was related to the cursor velocity, as predicted by the retinal-slip model. This velocity could be the velocity of either the left or right cursor, depending on which one was being pursued, or the average velocity of both cursors. To test this hypothesis, we took the average velocity in the elevation direction of each of the gaze segments that were classified as smooth pursuit, and did the same for the corresponding left and right cursor segments. As shown for all subjects in figure 3.5a, we used these velocities to compute the Pearson correlation between smooth pursuit velocity and the velocity of the left (+) and right (×) cursor, and the average velocity of both cursors (∘). When considering all r-values together, we found a significant correlation between smooth pursuit velocity and cursor velocity in 60% of the cases. For these cases, the correlation was weak, and could be either positive or negative, ranging from −0.3 to 0.4, where a negative correlation corresponds to a situation where pursuit velocity decreased when cursor velocity increased.

Thus, the lack of correlation indicates that smooth pursuit velocity was not related to cursor velocity (figure 3.5a), and non-saccadic events always showed a unimodal continuum of cursor velocity. To further explore this finding, we performed an additional analysis in which we took all non-saccade epochs (smooth pursuit and fixations), and focused on the elevation component of gaze. If smooth pursuit velocity was indeed related to cursor velocity, we would expect the gaze velocity in these non-saccade epochs to

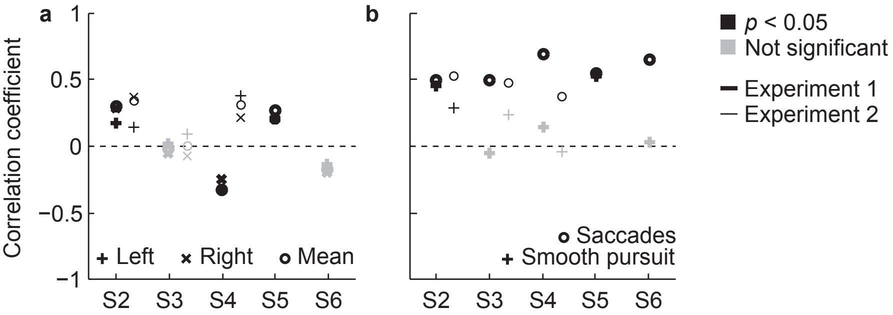

Figure 3.5 Smooth pursuit velocity correlates with distance-to-goal and not with cursor velocity. Pearson's correlation coefficients (r-values) are represented by bold symbols (experiment 1) or regular symbols (experiment 2). Significant ($p < 0.05$) and non-significant values are shown in black and gray, respectively. **(a)** Correlation between smooth pursuit velocity and the velocity of the left (+) and right (×) cursor, and the average velocity of both cursors (∘), computed by taking the average velocity in elevation direction of each of the gaze segments that were classified as smooth pursuit and the average velocity in elevation direction for the corresponding left and right cursor segments. **(b)** Correlation between smooth pursuit velocity (same segments as in (a)) and the average distance between gaze and the final goal (+). Same for saccade peak velocity (∘).

show a bimodal distribution, with one peak centered around zero velocity (fixation) and a second, smaller peak centered around 30 deg/s, which would approach the speed of the cursors (average of both cursors across subjects in the second half of trials was 34.7 deg/s (SD 4.7 deg/s)). Our data did not show this. Instead, the velocities of all non-saccade segments followed a distribution with a single peak (figure 3.6a). When all scenes were pooled, most subjects showed a peak centered at zero velocity (fixation) and a tail in the positive (upward) direction. In one special scene where the gates were absent (experiment 1, scene 1), subjects showed fewer fixations and more smooth pursuit segments. In this case, all subjects had a distribution of gaze velocities with a tail in the positive direction and showed a positive drift in the unimodal gaze velocity distributions. We repeated this analysis using two-dimensional gaze velocities and obtained similar results.

The lack of correlation indicates that smooth pursuit velocity was not related to cursor velocity (figure 3.5a), and that non-saccadic events always showed a unimodal continuum of gaze velocities (figure 3.6a). In addition, smooth pursuit was interleaved with saccades which took gaze well ahead of cursor location (figure 3.4). This behavior is different from regular 'catch-up' saccades, which bring the fovea back onto a retinal target during fast or unpredictable target motion. This led us to hypothesize that the slow eye movements did not simply represent an ocular following of the moving cursors. Instead, we considered that smooth pursuit might work in conjunction with the saccades, to drive the control of the movements of the cursors, upwards towards the final goal.

To test this hypothesis, we calculated, for each smooth pursuit segment, the average distance between gaze and the final goal of the cursors, and correlated this distance with the average smooth pursuit velocity of that segment (r-values marked with '+' in figure 3.5b). For the subjects with a high portion of smooth pursuit eye movements (S2 and S5, see figure 3.2c), we found that smooth pursuit velocity was positively correlated ($r = 0.45$, $p < 10^{-24}$, S2, experiment 1; $r = 0.29$, $p < 10^{-7}$, S2, experiment 2; $r = 0.52$, $p < 10^{-33}$, S5)

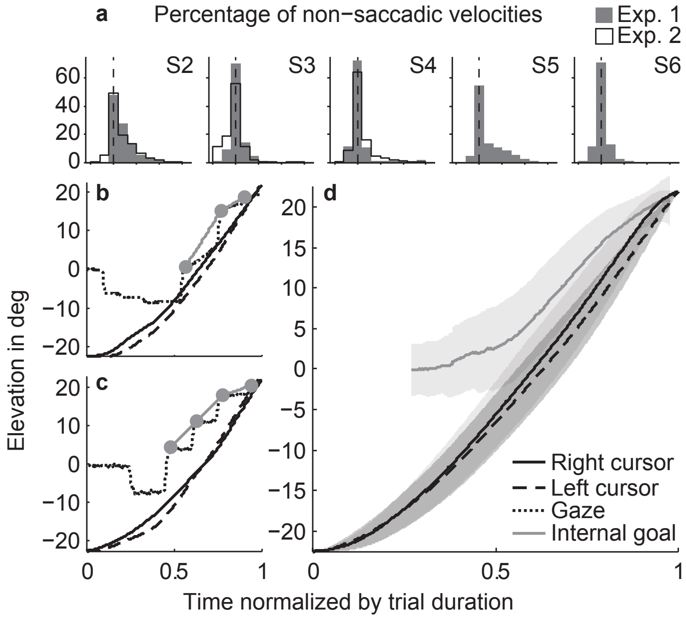

Figure 3.6 Gaze follows a goal trajectory ahead of the cursors with a unimodal distribution of non-saccadic gaze velocities, which argues against ocular following of the cursors. **(a)** Histograms of gaze velocities during fixations and smooth pursuit for S2–S6 in experiment 1 (gray) and for S2–S4 in experiment 2 (white). For each non-saccadic segment (i.e., fixations and smooth pursuit), we calculated the mean gaze velocity in the elevation direction. The dashed lines mark the gaze velocity of 0 deg/s, as would be expected for steady fixation. **(b)** left cursor (dashed line), right cursor (solid black line) and gaze (dotted line) position in the elevation direction as a function of time (normalized by trial duration) for a single trial of S2, scene 8, experiment 1. The gray line shows the linear interpolation of saccade endpoints (gray dots) occurring beyond the final gate. **(c)** Same as for S4. **(d)** Left (dashed line) and right (solid black line) cursor position in the elevation direction averaged over all subjects, scenes, and experiments. The gray line shows the average over all interpolated gaze epochs (see gray lines in (a) and (b)), representing the internal goal trajectory. Shaded areas represent the SD. Trial durations were between 1.5 and 3 s (see figure 3.2b).

with the distance to the goal. Thus, gaze appeared to slow down when approaching the final goal by slowing down pursuit. This result explains the range in correlations found between pursuit and cursor velocity (figure 3.5a). The degree to which subjects accelerated the cursors to the maximum velocity differed among subjects. Subjects who quickly accelerated the cursors had a constant cursor velocity (equal to the maximum velocity) during the second part of the movement, where the smooth pursuit events occurred. This yielded a correlation coefficient around zero. Subjects who accelerated the cursor more gradually had an increasing cursor velocity during the second part of the movement, resulting in a negative correlation, as the pursuit velocity decreased towards the end of the movement. In some cases, subjects decelerated the cursors when they approached the final goal, resulting in a positive correlation.

An interesting question arises as to whether saccades also become slower (and therefore smaller) when approaching the final common goal of the cursors. To answer this question, for each trial we took the series of saccades between the gates and the final goal, and we correlated the peak velocity of each saccade (except the last one, see below) with distance-to-goal measured as the Euclidean distance between saccade onset and goal (r-values marked with '∘' in figure 3.5b). Notice that, for the last saccade in each series, the saccade endpoint is equal (or close) to the final goal. Thus, for these saccades, it is trivial that saccade velocity is correlated with distance-to-goal, as smaller saccades have lower peak velocities. For the other saccades, the endpoint could be anywhere between the gates and the goal. For all subjects, we found significant correlations between 0.37 ($p < 10^{-5}$) and 0.69 ($p < 10^{-33}$), confirming that the saccades that brought the eye via intermediate locations on the screen to the goal also slowed down as they approached the goal.

In summary, we found that gaze followed a goal trajectory that consisted of a series of saccades interleaved with smooth pursuit (figure 3.6b) or fixations (figure 3.6c). This goal trajectory, revealed by performing a linear interpolation of the saccade endpoints and averaging the outcome over all trials (figure 3.6d), was always ahead of the movement of the cursors, and slowed down in the final stretch, while the cursors maintained a more or less constant velocity. Pursuit velocity was not related to velocity of one of the cursors, but was often related to distance of gaze relative to the final goal, with a positive correlation between pursuit velocity and distance-to-goal. The same was true of saccade velocity. Thus, a combination of fast and slow eye-movements, driven by an internal goal trajectory, seems to guide the cursor movements.

3.4 Discussion

In this study, we investigated the role of saccades and smooth pursuit when subjects created their own internal representation of a future trajectory to guide two cursors in a video game. We found that gaze led the cursors toward the final common goal in a series of saccades, as illustrated in figure 3.6, and, especially for two slower subjects, also segments of slow goal-directed eye movements. Surprisingly, these segments of smooth pursuit did not correlate with the position and velocity of the moving cursors on the screen, but seemed to follow an internal trajectory ahead of the cursor movements. To our knowledge, this study is the first to demonstrate that gaze can lead self-generated movements in a visuomotor task by a combination of saccades and smooth pursuit, and that smooth pursuit can be used proactively to plan and guide a future movement.

When visually guided hand movements are executed, saccades often lead the hand to spatial target locations (Sailer et al., 2005; Land, 2006). In a reaching task in which the demand for vision was manipulated, it was shown that gaze moved to the next location as the demand at the previous location decreased (Sims et al., 2011). Our study shows that, in addition, the relative timing between gaze and cursor movements depends on the demand for vision at the next event. For asymmetric scenes, we found that gaze was directed toward the first (lower) gate and moved on to the next (upper) gate about 125 ms before the cursor entered the first gate. However, for the symmetric scenes, this strategy could become problematic, as each cursor enters its respective gate nearly simultaneously, whereas gaze cannot be directed to both gates simultaneously. In these cases, subjects directed their gaze toward the second gate ~336 ms before the cursor entered the first gate, which was more than 2.5 times earlier than for the asymmetric scenes. However, at the second gate, there was no urge for gaze to quickly move on to the next event—the distance between the second gate and the final goal was >10 deg of visual angle for all scenes. Therefore, lead times at the second gate were much smaller than those at the first gate. This result implies a flexible coupling between gaze and the thumb movements, depending on scene geometry, in contrast to previous studies that have suggested a fixed 'yoking' of eye and hand (Neggers and Bekkering, 2000, 2001).

In a previous study, eye and hand movements were measured during tracking of a target that made an unpredictable change in direction. The investigators incorporated conditions whereby the hand and eye tracked the target separately, as well as in combination (Engel and Soechting, 2003). They found that, for combined eye-hand tracking, the latency for a change in direction of the eye movement increased to approach the latency of the hand movement, as compared to the latency in the eye-alone tracking. The hand did exactly the opposite; that is, it decreased its latency with respect to hand-alone tracking. In our study, both smooth pursuit and saccade velocity decreased over time during the second part of the movement. This is nicely illustrated by figure 3.6, which shows that the deceleration of gaze during the second part of the trial reduced the distance between gaze and the cursors, and thus improved the visual guidance of the cursors to the final common goal. Taken together, these observations demonstrate a flexible coupling between gaze and cursors in which gaze tends to join the cursors and vice versa.

This hypothetical compromise between eye and cursor trajectories might reflect a compromise between exploring the future path and verifying that the cursors move along the path. Recently, we suggested that such a strategy could explain why the eye leads the fingertip by a fixed distance, using a series of fixations interleaved with saccades, when the finger traces a fully visible target path (Tramper and Gielen, 2011). We also showed that interpolating the saccade endpoints revealed the goal trajectory of the eye along the path, which leads the hand position along the path. In the present study, we used the same analysis, which revealed an internal goal trajectory for gaze that was not following the moving cursors visible on the screen (figure 3.6). Instead, gaze was leading the cursors.

It is possible to generate pursuit in absence of a foveal stimulus (see section 3.1), e.g. when subjects were instructed to pursue the mid-point between two peripherally located targets that moved sinusoidally (Barnes and Hill, 1984). In these cases, smooth eye velocity is highly correlated with the movement of peripheral targets. We found that smooth pursuit velocity slowed down when the eyes approached the final goal of the cursors, whereas the cursor velocity remained rather constant. This explains why smooth pursuit velocity was correlated with the distance remaining between gaze location and the goal, but was not well correlated with hand velocity. Thus, during smooth pursuit, gaze did not follow the average movement of the extra-foveal cursors but followed a different, self-generated target trajectory. To distinguish this target from imaginary moving targets or occluded targets, we call this an internal target.

The observation of pursuit eye movements in the absence of a moving target is not new. First, there are glissades at the end of saccades. However, as the duration of glissades is short (~24 ms; Nyström and Holmqvist, 2010), they cannot explain the pursuit of inter-saccadic intervals of several hundred of milliseconds, as in our study. Moreover, Frens and Van der Geest (2002) demonstrated that glissades are absent when scleral search coils are used. Therefore, they may also be absent with the DMI methods used in this study, in which subjects use a ring on the sclera. Post-saccadic enhancement (Lisberger, 1998) just after saccades may well contribute to our inter-saccade pursuit, but this is consistent with our interpretation. Moreover, anticipatory pursuit has been reported when the subject expects the target to move and pursuit is subject to modulation by attention (Kowler, 1990). Our data reveal a new type of pursuit in the absence of a physically moving target, which has not been reported before. All these findings together indicate that pursuit is much more flexible than previously thought, and our study shows a clear functional role for such flexibility in a natural task involving hand-eye coordination.

Recently, scientists have debated the traditional view that the smooth pursuit and saccadic system are two distinct neural systems (Keller and Missal, 2003; Krauzlis, 2004). In this study, we found that both smooth pursuit as well as saccadic eye movements slowed down when approaching the common target for the two hands. This result provides behavioral evidence that both systems can work together to follow the same, internal trajectory in complex visuomotor tasks. It is known that saccades anticipate the future location of gaze before the actual eye movement is made (Duhamel et al., 1992). Recently, it has been shown that the same holds for smooth pursuit, where attention is allocated ahead of the pursuit eye movement (Khan et al., 2010). Our result fitsperfectly with the idea that both visual attention and gaze are biased in the direction of the goal to plan and guide upcoming movement.

4

A POMDP model of eye-hand coordination

T. Erez
J.J. Tramper
W.D. Smart
C.C.A.M. Gielen

Published in *Proceedings of the Twenty-Fifth AAAI Conference on Artificial Intelligence*, 2011

4.1 Introduction

Eye-hand coordination is an integral part of many human activities, and has been the subject of scientific inquiry for more than a century. This domain poses an interesting challenge of motor intelligence: the uncertainty inherent to the world's state requires active disambiguation; with foveal vision being a limited resource, effective behavior requires task-dependent allocation of information-gathering activity (gaze shift) and goal-directed behavior (hand reaching).

When trying to predict the eye's motion, a common null hypothesis is to assume the gaze is directed to visually-salient features of the scene (Koch and Ullman, 1985). However, here we consider tasks whose goal is the motion of the hand, with the eye playing a supportive role. In this case, the assumption that only image heuristics (such as saliency) account for the eye's movement seems unlikely. The top-down effects of the motor task on visual behavior are an active area of study (Peters and Itti, 2008; Rothkopf et al., 2007). Here we step away from neuroscientific investigation of visual processing, and abstract the eye's effect as a localized reduction in observation noise (section 4.3: *Observation*). This allows us to take a broader perspective on tasks which require coordination of information-seeking behaviors.

Todorov and Jordan (2002) propose the paradigm of optimal control as a framework for the study of motor coordination, and normative models (Körding, 2007) harness simulation and numerical optimization for the study of neural mechanisms. Algorithms of optimal control often rely on the principle of *certainty equivalence* (Stengel, 1994), which posits a separation between estimation and control: given an estimate of the current state of the world, the best action can be identified by considering a deterministic, fully-observable system in the same state. This separation allows for efficient computation, because optimal control can focus only on the deterministic system, and estimation can be safely ignored during motion planning. However, this separation does not hold in tasks which involve information-seeking behavior.

In order to capture the coupling between perception and action inherent to eye-hand coordination, we model this domain as a continuous-state partially-observable Markov decision processes (POMDP; Kaelbling et al., 1998; Sondik, 1971). The POMDP framework is designed to tackle domains with state uncertainty, and allows us to consider goal-directed actions and task-relevant information-pickup in a single optimization problem. The continuous POMDP model is described in section 4.3. High-dimensional, continuous POMDPs are notoriously hard to solve; here we use a deterministic belief update heuristic, described in section 4.2.

The domain of eye-hand coordination exhibits a large degree of task-specific behavioral diversity (Carpenter, 1988)—some circumstances elicit the use of saccades, while others elicit smooth pursuit. This is a modeling challenge, because we must allow for the emergence of a variety of possible solutions, depending on the specific instantiation of task parameters. Our POMDP model meets this requirement, as different parameter settings generate different motion patterns. In section 4.4 we discuss the role of the various parameters in shaping the resulting behavior.

Our model finds an optimal motion pattern of the hands and the eye, allowing for the emergence of coordination from first principles, without imposing heuristics. In order to test the model, we present a behavioral experiment in which human subjects perform the same eye-hand coordination task. The experiment and results are described in section 4.5; we find that simulation and experimental results are mostly congruent, demonstrating the validity of the model.

4.2 Solving high-dimensional, continuous POMDPs

In POMDP terminology, the agent is said to occupy a *belief* state, which is a distribution over all possible states, representing the agent's ambiguous sense of the world. For the most part, the POMDP literature focuses on finding globally-optimal solutions for discrete domains. Previous studies of continuous POMDPs (Brooks, 2009; Brunskill et al., 2008; Porta et al., 2006) focus on finding a globally-optimal solution for domains with only one or two dimensions. Several recent studies (Erez and Smart, 2010; Miller et al., 2009; Prentice and Roy, 2009) propose an alternative approach to continuous POMDP optimization—finding the optimal behavior by planning deterministic trajectories through belief-space. In this paper, we use the Nominal-Belief heuristic (Miller et al., 2009), replacing the stochastic observation with its maximum-likelihood counterpart (Erez and Smart, 2010) during planning. The resulting belief dynamics are deterministic, and therefore amenable to efficient optimization algorithms. However, since planning takes place in the belief domain, the optimization still accounts for the state's ambiguity (as this information is represented by the various belief states). Therefore, the resulting behavior strikes a balance between information-seeking and goal-directed action, despite the marginalization of the stochastic processes.

Definitions Formally speaking, we consider a discrete-time POMDP defined by a tuple $\langle S, A, Z, T, \Omega, R, N\rangle$, where: S, A and Z are the state space, action space and observation space, respectively; $T(s', s, a) = \Pr(s'|s, a)$ is a transition function describing the probability of the next state given the current state and action; $\Omega(z, s, a) = \Pr(z|s, a)$ is the observation function, describing the probability of an observation given the current state and action; and $R(s, a)$ is a reward function, and a terminal reward $R^N(s)$. In this paper we consider an undiscounted optimality criterion, where the agent's goal is to maximize the expected cumulative reward within a fixed time horizon of N time steps.

The *belief state* $b \in B$ is a probability distribution over S, where $b^i(s)$ is the likelihood of the true state being s at time i. Ignoring the effect of feedback control, the reward associated with a belief is simply the expected value over this state distribution:

$$R^i(b, a) = \mathop{\mathrm{E}}_{s\sim b}\left[R^i(s, a)\right]. \tag{4.1}$$

Given the current belief b, an action a and observation z, the updated belief b' can be calculated by applying Bayes's rule. However, in the continuous case B is infinite-dimensional, and therefore the belief update must be approximated by some estimation filter.

The deterministic belief update heuristic We study continuous stochastic dynamics of the form $ds = f(s, a)dt + q(s, a)d\zeta$, where ζ represents continuous-time Brownian motion. For a given state s and action a, integrating this continuous dynamics over a small time-step τ results in a normal distribution over the next state s': $T(s', s, a) = \mathcal{N}(s'|F(s, a), Q(s, a))$, where the mean is propagated with the Euler integration

$$F(s, a) = s + \tau f(s, a), \tag{4.2}$$

and the covariance $Q = \tau q^{\mathsf{T}} q$ is a time-scaling of the continuous stochastic process $qd\zeta$. Similarly, we focus on observation distributions of the form $\Omega(z, s, a) = \mathcal{N}(z|w(s), W(s, a))$, where w is a deterministic observation function, and W describes how the current state and action affect the observation noise.

Given a Gaussian prior on the initial state, we approximate the infinite-dimensional b by a single Gaussian: $\hat{b}(s) = \mathcal{N}(s|\hat{s}, \Sigma)$, where the covariance Σ belongs to the space of symmetric, positive-semidefinite matrices $\mathcal{M} \subset \mathbb{R}^{n \times n}$. Therefore, the belief space $\hat{B}$ is parameterized in this case by the product space $v \in S \times \mathcal{M}$. In the limit of $\tau \to 0$, and given a Gaussian prior, this approximation is accurate. (Note that this single-Gaussian approximation fails when the domain includes discontinuities and unilateral constraints (e.g., joint limit constraints, or confining walls); in such cases, a different formulation of the belief is needed (Erez and Smart, 2010).)

In order to approximate the belief update, we use the Extended Kalman Filter (EKF) (Stengel, 1994). Given the current belief $\hat{b}$, action a and observation z, we calculate the partial derivatives of the dynamics and the observation functions around $\hat{s}$: $w_s = \partial w / \partial s$ and $F_s = \partial F / \partial s$. We find the uncorrected estimation uncertainty $H = F_s \Sigma F_s^{\mathsf{T}} + Q(\hat{s}, a)$ and calculate the new mean $\hat{s}'$ by the innovation process:

$$\hat{s}' = F(\hat{s}, a) - K(z - w(\hat{s})), \tag{4.3}$$

where $K = H w_s (w_s^{\mathsf{T}} H w_s + W(\hat{s}, a))^{-1}$ is the *Kalman gain*. Finally, the new covariance Σ' is given by:

$$\Psi(\hat{s}, \Sigma, a) = H - H w_s (w_s^{\mathsf{T}} H w_s + W(\hat{s}, a))^{-1} w_s^{\mathsf{T}} H^{\mathsf{T}}. \tag{4.4}$$

The deterministic belief update is obtained by taking the expectation of equations 4.3 and 4.4 with respect to the observation variable z. Since equation 4.3 is linear in z, the expectation operator replaces z with its mean $w(\hat{s})$, causing the second term of equation 4.3 to vanish. Therefore, the maximum-likelihood estimate of the next belief's mean is reduced to the deterministic dynamics 4.2. By virtue of the EKF being a first-order filter, the calculation in 4.4 is independent of z, and so the next belief's covariance is the same, regardless of the value of z. In summary, the maximum-likelihood estimate for the next belief is formed by by combining 4.2 and 4.4: $\hat{b}'(s) = \mathcal{N}\big(s|F(\hat{s}, a), \Psi(\hat{s}, \Sigma, a)\big)$.

Planning in the belief domain The belief update heuristic of the previous section (together with equation 4.1) define a problem of deterministic optimal control in a high-dimensional continuous space, with non-linear dynamics and non-quadratic reward. To find a locally-optimal solution, we may use trajectory optimization; here we use Differential Dynamic Programming (DDP), a second-order algorithm that has been successfully applied to high-dimensional, non-linear control domains (Abbeel and Ng, 2005; Tassa et al., 2008).

4.3 A POMDP model of eye-hand coordination

We model the position of the gaze target in the frontal plane, as well as the position of the hands' end-effectors in that plane. In addition, the model's state includes the (a priori unknown) planar positions of a target and four obstacles. The agent's task is to guide both hands to the target while passing between a pair of obstacles, using the eye's gaze to locally disambiguate portions of the scene (figure 4.1). By solving for an optimal motion plan, we generate a coordinated movement of hands and eye through the scene. The model and the resulting motion are best illustrated by a short movie, available at `youtu.be/PxvLIaoLn2o`.

State, action, and transition function The system's state is the concatenation of the planar positions of the agent's state and the environment's state. The agent has kinematic control of gaze fixation point ($s_e \in \mathbb{R}^2$) and two hands ($s_{h_1}, s_{h_2} \in \mathbb{R}^2$); the agent's state also includes a scalar time-lag variable (s_k), which measures the time from the last saccade. The environment's state specifies the positions of the target (s_T) and obstacles ($s_{b_i}, i = 1 \ldots 4$). This leads to a 17-dimensional state space.

The state update is subject to process noise whose magnitude is constant in time but varies between the elements of the scene. For example, the state update equation for the target position is:

$$s'_T = s_T + \sigma_c \xi, \tag{4.5}$$

with ξ being a two-element vector of zero-mean normally-distributed random variables with unit variance (same equation holds for s_{b_i}, the state dimensions describing the positions of the obstacles). The parameter σ_c scales the process noise for the target and obstacles (see discussion in section 4.5: *Process noise*).

The agent controls six continuous action variables, specifying the displacement of the hands and eye at every time step. For example, the state update equation for the hand's position is:

$$s'_{h_1} = s_{h_1} + a_{h_1} + \sigma_h \xi, \tag{4.6}$$

where σ_h is a model parameter that sets the magnitude of the process noise affecting the hand; the same equation holds for s_{h_2} and s_e, and their corresponding controls. We eliminate any uncertainty in the eye's position by not subjecting it to process noise ($\sigma_e = 0$).

It is known that the brain's processing of visual information is impaired (even if not completely inhibited) during a saccade. Furthermore, it has been shown (Thorpe et al., 1996) that even after the eye's gaze settles on the new target, it takes some time before visual information is available for some tasks. We model this effect with an auxiliary state variable s_k, which measures the time elapsed from the last saccade. This variable integrates linearly when the eye's velocity is zero, and becomes very low otherwise:

$$s_k' = \tau + \frac{s_k}{1 + \alpha \|a_e\|}, \tag{4.7}$$

where τ is the time-step length, and α is some large coefficient (we use $\alpha = 1000$). Like the eye's position, this auxiliary variable is also not subject to any process noise, and therefore needs no estimation.

Observation In a POMDP, the agent receives stochastic observations, through which it infers the true state of the system. Here, the agent may observe the state of all the scene's elements, and the observation of every element's position is randomly drawn from a normal distribution centered at the true underlying value; the agent has accurate observation of the eye's position, as well as the time since the last saccade.

The covariance of the observation of each scene element depends on its position relative to the eye's gaze. Let $d_* = \|s_* - s_e\|$ be the Euclidean (planar) distance between a scene element and the eye's gaze point ($*$ standing for either a hand, a target or an obstacle), and let $g(d)$ be a function that scales the width of this element's observation distribution; this function models foveated vision, so it is low around $d = 0$, and high farther away. We chose to model g as a sigmoid: given a width parameter η and a slope parameter l, we look at the scaled distance

$$\tilde{d}(s_*, s_e) = (\|s_* - s_e\| - \eta)/l_d, \tag{4.8}$$

and compute:

$$g(\tilde{d}) = \sigma_o\Big(0.5 + \frac{\tilde{d}}{2\sqrt{\tilde{d}^2 + 1}}\Big), \tag{4.9}$$

with σ_o being the maximal observation covariance due to peripheral vision (see discussion in section 4.4). The width of the human fovea is about 2 deg; in our experimental setup, this translates to 7% of the scene's width, and so we set $\eta = 0.035$, and $l_d = 0.005$.

Modeling post-saccadic perceptual delay In order to model the time delay due to processing of visual information, we added a term to the observation's covariance that is sigmoidal in the elapsed time since the last saccade. We scale the elapsed time s_k: $\tilde{t} = (\mu - s_k)/l_k$, and compute

$$k(s_k) = \alpha\Big(0.5 + \frac{\tilde{t}}{2\sqrt{\tilde{t}^2 + 1}}\Big). \tag{4.10}$$

We set $\mu = 150$ ms and $l_k = 30$ ms following Thorpe et al. (1996), and α is some large coefficient (we use $\alpha = 1000$). Therefore, the observation's covariance remains high for the first 120 ms after a saccade; at 150 ms this term drops, allowing the elements within the fovea to be observed accurately. Put together, the distribution of the observation for any scene element $*$ (target or obstacles) is:

$$\omega(o_*|s_*, s_e, s_k) = \mathcal{N}\Big(s_*, \mathbf{I}_2 \cdot (k(s_k) + g\big(\tilde{d}(s_*, s_e)\big)\Big). \tag{4.11}$$

Proprioception Proprioception is an independent channel of observation for the hands' positions. We model this by bounding from above the covariance of the hands' observation (as given by equation 4.11) by a fixed value σ_p, the observation noise of proprioceptive observations. Therefore, the distribution of observations for the hands is:

$$\omega(o_*|s_*, s_e, s_k) = \mathcal{N}\Big(s_*, \mathbf{I}_2 \cdot \max(\sigma_p, k(s_k) + g\big(\tilde{d}(s_*, s_e)\big)\Big)\Big). \tag{4.12}$$

The reward function The reward function has two parts: running reward and terminal reward. The terminal reward is a penalty (cost) that is quadratic in the distance of the hands from the target: $R_N(s) = c_T\Big(\big\|s_{h_1} - s_T\big\|^2 + \big\|s_{h_2} - s_T\big\|^2\Big)$. The running reward has two cost terms:

$$R(s, a) = -c_b \sum_{i=1}^{2} \sum_{j=1}^{4} \delta(s_{h_i}, s_{b_j}) - a^{\mathsf{T}} M a \tag{4.13}$$

where δ is the delta function penalizing collision between hand and obstacle, and the quadratic action cost is given by the second term, with M being a diagonal matrix assigning weight 1 to the hands' displacement, and 0.01 to the eye's displacement.

The only non-quadratic term is the obstacle cost. In a deterministic system, the use of a delta-function would yield unrealistic motion, as the hand might pass at epsilon distance from the obstacle. However, since we plan in belief space, we use the belief cost function (equation 4.1). The obstacle-related belief cost is the expectation of this delta-function under the normal distribution describing the joint uncertainty in the positions of the hand and the obstacle. Therefore, the belief-cost due to the obstacles is a Gaussian, which can be computed in closed form.

4.4 Exploring the model's behavioral diversity

As mentioned in section 4.1, the domain of eye-hand coordination exhibits a diverse array of behaviors, and a candidate model should allow for an equally-diverse array of solutions. Our model employs three categories of parameters: the coefficients of the cost function, the coefficients describing the process noise, and parameters that determine the state-dependent observation noise. In this section, we discuss the model's parameters, and the behavioral diversity they enable.

The cost function parameters Our simulations suggest that the cost parameters are simple to choose, as the wrong value often leads to absurd behavior: for example, if the target cost parameter c_T is not big enough compared to the hands' action cost, the hands do not reach the target; increasing the target cost fixes the problem, and increasing it even more makes no difference (because the residual is already zero). The obstacle cost parameter c_b leads to interesting behavioral diversity—when it is very big (relative to the hand action cost), the hands increase their velocity as they pass between the obstacles, and if it is very small, the hands choose a shorter path that gets dangerously close to the obstacle. Such behaviors are conceivable in certain scenarios, but the human subjects in our experiment (section 4.5) exhibited neither.

Process noise While the observation noise is state-dependent, the process noise in equation 4.2 is constant. Two values need to be determined—σ_h, the process noise associated with the hands, and σ_c, the process noise associated with the static elements of the scene (target and obstacles). When the hands are not subject to process noise ($\sigma_h = 0$), the eye only looks at the obstacles, and when the static scene elements are not subject to noise ($\sigma_c = 0$), the eye's gaze shifts preemptively (before the hand reaches the obstacles), as one glance is enough to perfectly and permanently disambiguate their position.

In contrast, when the hands are subject to a significant process noise, the eye performs smooth pursuit, following each hand along its path as it approaches the obstacles. This allows the agent to be certain of the hand's position at the mission-critical moment, when it is near the obstacles. Similarly, applying some process noise to the static scene elements causes the eye's gaze to remain fixed on the obstacles until the hand passed through the obstacle pair, so as to ensure that no uncertainty accumulates before the hand reaches the obstacle.

Another two parameters of behavioral relevance are σ_p (the maximal observation covariance of the hands' positions) and σ_o (the maximal observation covariance of the static scene elements), appearing in equations 4.11 and 4.12. When the first is small, no smooth pursuit will emerge, as the agent has a reliable source of information of the hands' positions. When the second is small, saccades will be inhibited, as peripheral vision provides observations that are good enough.

4.5 Comparing the model's solution to human subjects' behavior

In order to conflate simulation results with human motor behavior, we tested six subjects in an eye-hand coordination task. Subjects were equipped with a game controller consisting of two thumbsticks to move a left and right virtual hand in a two-dimensional scene projected on a large screen. Subjects were asked to move each virtual hand through a pair of obstacles and reach a common goal within 3 s. The position of the two gates changed at every trial, randomly rotating between 12 different arrangements (each scene was repeated thirty times). The scene was presented to the subjects at a field-of-view of 45 deg. Before each trial, subjects had to fixate at the center of the screen. No instructions were given regarding eye movements during a trial. Eye movements were recorded using the double magnetic induction method (Bour et al., 1984).

The first row of panels in figure 4.1 shows the results of subject S5 for a single trial. The blue and red line represents the subject's trajectory of the left and right virtual hand, respectively. Gaze fixations are represented by green dots. The obstacles and target are

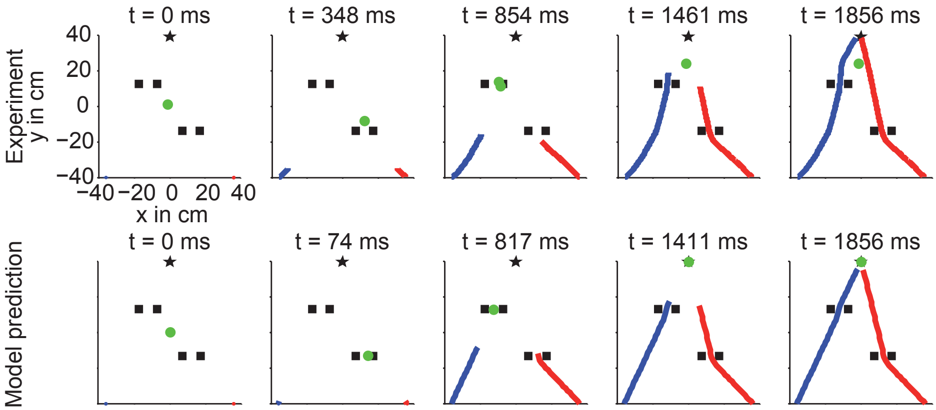

Figure 4.1 First row: Gaze fixations (green dots) and left/right hand trajectories (blue/red line) of subject S5 for a single trial, plotted in a two-dimensional plane. The obstacles and target are depicted by black squares and a star, respectively. Subsequent panels show a snapshot of the subject's behavior at the onset of a new fixation. Second row: POMDP model prediction.

depicted as black squares and a star, respectively. The subsequent panels show a snapshot of the subject's behavior at the onset of a new fixation. The first panel shows that the subject initially fixates at the center of the screen, with the hands a the starting position at the bottom of the scene. After 348 ms, the gaze saccades toward the right obstacle pair to assist the right hand in passing the obstacles (second panel). Before the right hand has reached the obstacle pair, gaze already jumps to the left obstacle pair at t = 854 ms (third panel). Note that this jump consist of one large saccade (from the right to the left gate) followed by a small, so-called correction saccade which is a well known phenomenon for large saccades (Carpenter, 1988). When the right hand approached the gate, a saccade is made toward a new location between the left gate and target (fourth panel) to guide both hands to the final goal, which was reached after 1.85 s from the beginning of the trial (last panel).

In the second row with panels, we plotted the hand trajectories and gaze trajectory as solved by the POMDP model. In order to compare the subject's behavior with the model predictions, we set the model's time limit equal to the subject's trial duration. The first panel shows the initial state of gaze and hand position. After 74 ms, gaze saccades to the right gate (second panel), which is earlier than the corresponding saccade of subject S5. Since the initial fixation was not preceded by a saccade, the model did not include a post-saccadic perceptual delay during the initial fixation, resulting in a short fixation duration. When the right hand reached the gate at t = 817 ms (third panel), gaze moved to the left gate to guide the left hand through the obstacles. At t = 1411 ms the left hand had passed the gate and gaze jumps toward the target (fourth panel) and stayed there until the end of the trial (last panel). Note that the timing of the second and third saccade is well in accordance with the subject's behavior.

We compared the predictions of the POMDP model with the experimental results of all trials and subjects on three criteria: (1) the order and location of fixations, (2) the trajectory of left and right hand, and (3) the relative timing of gaze and hands. Figure 4.2 shows

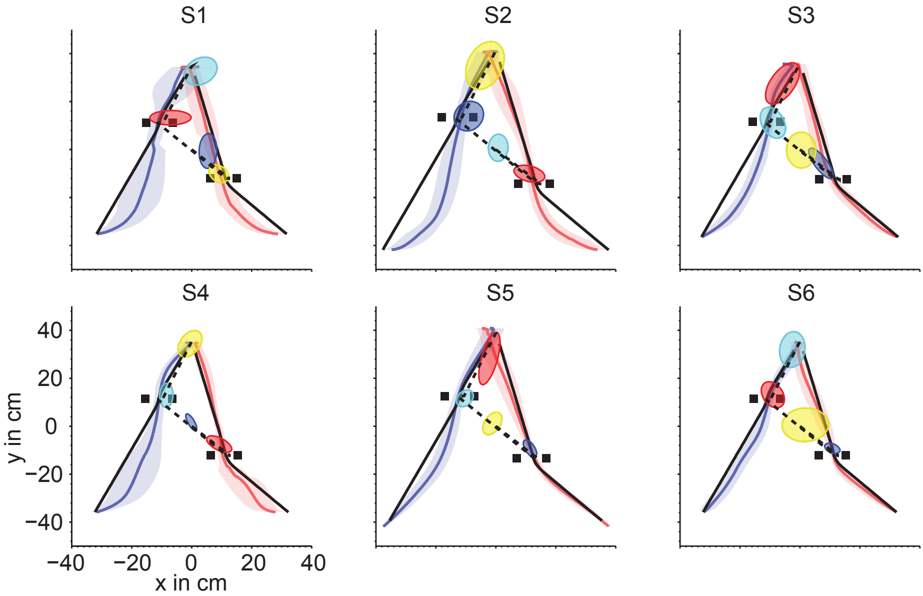

Figure 4.2 Trial averages of gaze fixations and hand trajectories for all subjects for the same scene as in figure 4.1. Clusters of gaze fixations are represented by colored ellipses (two SD). Hand trajectory is represented by the trial average (solid line) and the variability (shaded area, size of one SD) for left (blue) and right (red) hand. The dashed and black solid lines represent the model's solution for gaze and hand trajectories, respectively.

the trial average of all subjects for the same scene. The variability in hand position is represented by the shaded area (one standard deviation). Clusters of gaze fixations are represented by colored ellipses (two standard deviations). For this scene, the subjects' order of fixations (i.e., initial fixation, right obstacle pair, left obstacle pair, target) is in agreement with the model predictions. However, when the gates were located close to the initial fixation location at the center of the screen, or when the gates were sufficiently large, subjects do not direct their gaze to the relevant obstacles in the scene, but instead use their peripheral vision to perform the task. This behavior was found in two of the twelve scenes (17%), except for subject S3, which showed this behavior in nine scenes (75%).

The subjects fixate approximately between an obstacle pair, in agreement with the model predictions. The precise fixation location differs slightly between subject and model. Some subjects make slightly smaller saccades than the model. This undershoot is a known phenomenon (Carpenter, 1988) and is thought to reflect properties of the human saccadic system, which were not included in our model. In 62% of the scenes, the predicted fixation locations lay within the cluster of measured gaze fixations.

The right hand's trajectory predicted by the model matches the measured path for subjects S3, S5 and S6 almost perfectly, whereas the left hand shows a slightly curved trajectory. For the other subjects, both hands reach the target via a more curved trajectory than predicted by the model. For all subjects and scenes, the predicted hand trajectory was located within one standard deviation of the measured hand trajectories for 72% of the time. A control experiment revealed that even in absence of any obstacles, subjects tend to move the hands in an inward-curved trajectory whereas the model predicts a straight line (i.e., the shortest path). In that case subjects fixate at positions in the middle, between both hands. A plausible explanation for this behavior is that subjects use their peripheral vision to guide both hands to the target, relying on the heightened capacity to perceive motion through peripheral vision (McKee and Nakayama, 1984) (a feature which we did not try to model).

In addition to correctly predicting the spatial location of eye fixations and hand positions, the model also predicts the timing of gaze relative to hand position. This is illustrated in figure 4.1, which shows that gaze jumps from the initial gaze position at the start of each trial to the right obstacle pair, and from there to the left pair of obstacles after 0.9 s, when the right hand approached the obstacles. After another 0.6 s, gaze jumps from the left pair of obstacles to the target. By tuning the value of the parameter describing the obstacles' process noise, we recover this temporal pattern in our model.

4.6 Conclusion

This paper presents a POMDP model of hand-eye coordination, and demonstrates that the optimal solution is congruent with the behavior of human subjects performing the same task even with minimal assumptions on the actual parametric forms and numerical values. However, it is important to note that we do not argue for the biological plausibility of the computational techniques; instead, this normative model may allow us to test our understanding of what (we believe) the brain "should" do.

Experiments of eye-hand coordination tasks yield a diverse set of behaviors, according to the particular experimental setup. Our model captures this feature, as it can produce qualitatively-different behavior when the values of these parameters change (as explained in section 4.4). Here, we demonstrate how the model can be congruent with one particular experimental setup; this naturally guided our choice of parameter values to a particular region.

5

Time-integrated position error accounts for sensorimotor behavior in time-constrained tasks

J.J. Tramper
B. van den Broek
W. Wiegerinck
H.J. Kappen
C.C.A.M. Gielen

Published in *PLoS ONE*, 2012, 7(3): e33724

5.1 Introduction

In the past decade, it has become clear that many properties of human motor coordination can be well explained using the framework of stochastic optimal feedback control (Todorov and Jordan, 2002; Scott, 2004; Todorov, 2004; Kappen, 2005a). Successful applications have been reported for the manipulation of objects (Todorov and Jordan, 2002; Nagengast et al., 2009), the stability to accuracy trade-off (Liu and Todorov, 2007), bimanual responses to perturbations (Diedrichsen, 2007), visual feedback during hand movements (Saunders and Knill, 2004; Sims et al., 2011), cooperation between players (Braun et al., 2009b), risk sensitivity (Nagengast et al., 2010, 2011), and adaptation (Chhabra and Jacobs, 2006; Chen-Harris et al., 2008; Izawa et al., 2008). This framework uses optimization techniques to find a control law that minimizes a cost function associated with the actions necessary to perform a specific task. This cost function is closely related to what the system is trying to achieve. For sensorimotor control, the cost function therefore includes a component which is related to the effort necessary to complete the goal. The value of this effort-related penalty component, the control cost, increases quadratically with the magnitude of the control signal. In addition, the cost function generally includes a component related to the performance of the task. For goal directed movements, task performance can be modeled by including an end cost which penalizes the squared difference between the position of the effector (e.g., hand or cursor on a screen) and the goal at the end of the trial (Harris and Wolpert, 1998). This end cost component thus reflects the accuracy in achieving the goal.

In daily life we have to make decisions based on limited information from a noisy environment. Not only must we decide *what* the optimal sequence of actions should be, we must also decide *when* these actions should be executed. This is especially true for motor tasks in which subjects are required to complete the task within a particular time interval. For example, a tennis player has to hit the ball at the right angle and within a narrow time interval when the ball is within the reach of the player. Several studies have investigated such time-constrained motor tasks (Diedrichsen, 2007; Liu and Todorov, 2007; Izawa et al., 2008; Nagengast et al., 2009, 2010, 2011; Sims et al., 2011). Typically, the observed behavior has been modeled by minimizing a weighted combination of the control cost and the end cost, which corresponds to minimizing the effort and maximizing the task performance. Such a model predicts that subjects arrive on target exactly at the final time. Another strategy might be that subjects try to reach the target position well before the final time to avoid the risk of missing the target. To test this, we have investigated whether minimizing the effort and maximizing the task performance is sufficient to predict human motor behavior in time-constrained sensorimotor tasks. In addition to this standard model, we postulate a new model that includes an additional cost criterion which penalizes deviations between the position of the effector and the target throughout the trial, forcing arrival on target well before the final time.

To investigate which model gives the best fit to the data and whether that model is generic, we tested the models in two different time-constrained tasks. In the first task, subjects had to control a joystick to move a ball on a screen to hit a target at the end of a fixed time interval. In the second task, the single target was replaced by two targets. Now subjects were asked to steer the ball to one of the targets. They were free to choose which one. Previous work has shown that the subject's behavior may depend on the level of uncertainty in the task (Nagengast et al., 2010, 2011). Therefore, we superimposed noise with different amplitudes on ball position to introduce uncertainty about future ball positions. This allowed us to investigate the ability of the models to predict motor behavior in two different tasks and at different levels of uncertainty.

The results show that a simple cost function representing a trade-off between effort and performance is insufficient to describe the observed behavior in our experiment. The model that we propose predicts that subjects steer the ball to the target position well before the final time is reached, which is in agreement with the observed behavior. This result is consistent for all noise amplitudes and for both tasks.

5.2 Methods

Subjects We have tested subjects in two different tasks. Twelve subjects (seven males) aged between 21 and 28 years participated in these tasks. Four of them (labeled as S1–S4) took part in the one-target task, four (S9–S12) in the two-target task and four (S5–S8) in both tasks. All subjects were right-handed and none of them had any known neurological or motor disorder. All subjects were naive regarding the purpose of the experiment. Subjects gave written informed consent prior to the start of the experiment according to institutional guidelines of the "Commissie Mensgebonden Onderzoek" (or CMO, translated: "Committee for research on human subjects") of the Radboud University Medical Center Nijmegen.

Experimental procedures Subjects were seated in a chair, such that their eyes were located 70 cm in front of a 160 × 160 cm^2 rear-projection screen. A white ball and one or two white targets on a dark background were rear-projected on the screen with an LCD projector (JVC DLA-S10) with a refresh rate of 75 Hz. The ball and target were represented by a dot with a diameter of 1.5 cm and a vertically oriented bar with a size of 0.5 × 4 cm^2, respectively. The ball moved from the left to the right at a constant velocity and subjects could control the vertical velocity of the ball by a joystick. The joystick could only move up- or downward in a range between −55 and 55 deg. The length of the joystick handle was 17 cm. Joystick output was measured at a sample rate of 75 Hz. To avoid a bias in the ball's movement when the joystick was near the neutral position, the output was set to zero for excursions in the range between −2 and 2 deg. Above (below) this threshold, the velocity signal increased (decreased) linearly with joystick excursion angle.

The size of the computer-generated animated scene on the screen was 147 × 109 cm^2. We defined a coordinate system with time t in the horizontal direction, where the left and right boundaries of the animation corresponded to the start ($t = 0$) and end ($t = t_f$) of each trial. The range $[0, t_f]$ corresponded to a distance of 147 cm. The vertical direction was represented by normalized coordinates $y \in [-1, 1]$, where $y = -1$ and $y = 1$ defined the lower and upper boundary of the animation, respectively. The maximum excursions of the joystick corresponded to a control $u = +1$ (upward) and $u = -1$ (downward).

In the one-target task, the target was located in the middle at the right of the screen ($y = 0$, see figure 5.1a). The ball started at the left side of the screen at a random vertical position between −0.5 and 0.5 and moved at a constant horizontal velocity of 49 cm/s to the right, reaching the right boundary after three seconds ($t_f = 3$ s). The subject's task was

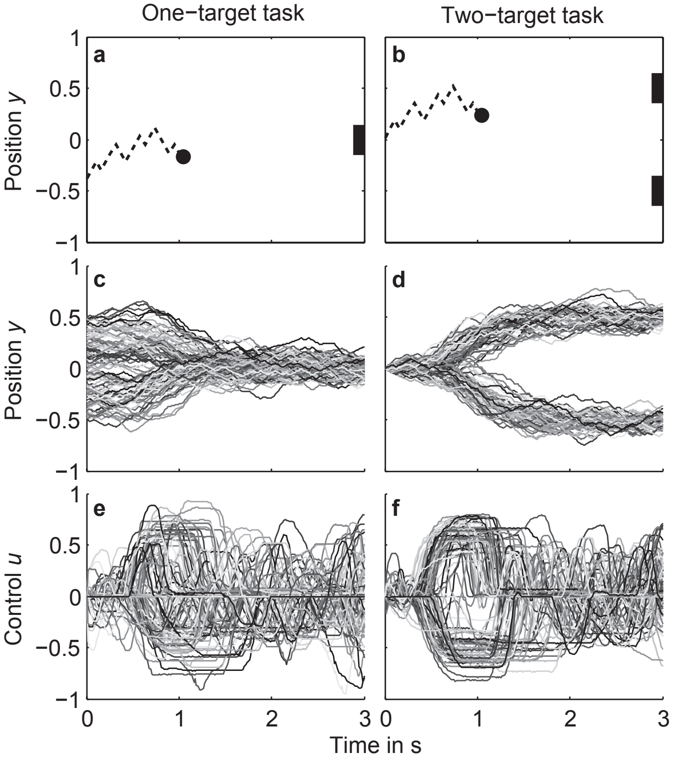

Figure 5.1 Schematic of the tasks. **(a)** In the one-target task (left panel), subjects had to control a joystick to move a ball on a screen to hit a target (rectangle) at time $t = 3$ s. The ball (circle) started at a random vertical position between –0.5 and 0.5 at the left of the screen and moved at a constant horizontal velocity to the right. Subjects could move the ball up- or downwards. Gaussian white noise was superimposed on the vertical ball position to introduce uncertainty about future ball positions. The dashed line illustrates the trajectory of the ball. **(b)** In the two-target task (right panel), two targets were present at vertical positions –0.5 and 0.5. The ball started at vertical position $y = 0$ at the left of the screen. Subjects were asked to steer to one of the targets and they were free to choose which one. All other experimental conditions were exactly the same as for the one-target task. **(c)** Ball position time traces (100 trials) of subject S6 performing the one-target task with noise amplitude $\nu = 0.009$. **(d)** Same for the two-target task. **(e)** Control signal time traces corresponding to the ball position time traces in panel c (100 trials) of subject S6 performing the one-target task with noise amplitude $\nu = 0.009$. **(f)** Same for the two-target task.

to hit the target by steering the ball up- or downwards. Thus, the subject was unable to manipulate the horizontal position of the ball. No instruction was given as to whether the movement should meet any criteria, except to hit the target with the ball.

Gaussian white noise was superimposed on the vertical position of the ball to introduce uncertainty about future positions. Thus, in the absence of a control signal the displacement of the ball described a Wiener or 'random walk' process. At each time step, the vertical position y_t at time t was updated according to $y_{t+dt} = y_t + u_t dt + d\xi_t$, with u_t the subject's control signal at time t (units s^{-1}), dt the time step size (13.3 ms), and $d\xi_t = \pm\sqrt{\nu dt}$ pseudo-random Gaussian white noise at time t with amplitude ν (units s^{-1}). Subjects were tested in four consecutive blocks with 100 trials each, with a noise amplitude ν of consecutively 0 (no noise), 0.009, 0.04, and 0.08. For each noise amplitude, the same pseudo-random sequences were used such that each subject was subjected to exactly the same noise realizations. Each block with 100 trials was preceded by five trials to familiarize subjects with the task. These five trials were not included in the data analysis.

In the two-target task, we replaced the single target by two targets at vertical positions −0.5 and +0.5 (see figure 5.1b). In each trial, the ball started at vertical position $y = 0$. Subjects were now asked to steer the ball to one of the targets. They were free to choose which one. All other experimental conditions were exactly the same as for the one-target task.

Standard model with end cost only We used stochastic optimal feedback control to predict the subject's control and corresponding position of the ball for each noise amplitude and for both tasks. The dynamics of the control problem was described by the stochastic differential equation

$$dy = udt + d\xi \tag{5.1}$$

with y_0 and y_f the initial and final ball position along the vertical axis. Equation 5.1 shows that a change in vertical position y was caused by a control action u and noise $d\xi$. We defined a cost function with two components. First, we included the cumulative control cost proportional to the integral of the square of the control during the trial, which is defined by

$$C_u = \int_0^{t_f} \tfrac{1}{2} Q_u u(t)^2 dt, \tag{5.2}$$

where Q_u is a positive constant. Second, we added an end cost proportional to the squared difference between the ball's end position y_f and the target position y^*, which is defined by

$$C_f = \tfrac{1}{2} Q_f (y_f - y^*)^2, \tag{5.3}$$

where Q_f is a positive constant. The optimal control problem was to find the control sequence $u(t)$ which minimizes the sum of the control cost C_u and the end cost C_f. For the one-target task, the optimal control solution can be solved analytically (Kappen, 2005b). Because the dynamics was stochastic (except for the case with noise amplitude $\nu = 0$), we consider the expectation value of the cost function over all possible future realizations of the Wiener process, which we minimize over all possible controls:

$$C_{total} = \left\langle \tfrac{1}{2} Q_f (y_f - y^*)^2 + \int_0^{t_f} \tfrac{1}{2} Q_u u^2 dt \right\rangle_{y_0}, \tag{5.4}$$

where the first and second component represent the end cost and control cost, respectively.

The subscript y_0 on the expectation value indicates an expectation over all stochastic trajectories starting in y_0. For this problem, the optimal cost-to-go $J(y,t)$ at time t and position y can be computed exactly (Kappen, 2005b), and is given by

$$J(y,t) = \nu Q_u \ln\left(\frac{\sigma}{\sigma_1}\right) + \frac{\sigma_1^2}{2\sigma^2} Q_f (y - y^*)^2, \tag{5.5}$$

with $\sigma^2 = \nu(t_f - t)$ and $1/\sigma_1^2 = 1/\sigma^2 + Q_f/(Q_u \nu)$. The optimal control is proportional to the partial derivative of $J(y,t)$ to y (Kappen, 2005b):

$$u(y,t) = -\frac{1}{Q_u}\frac{\partial J(y,t)}{\partial y} = -K(t)(y - y^*) \tag{5.6}$$

with

$$K(t) = \frac{1}{Q_u/Q_f + t_f - t} \qquad (Q_u/Q_f \geq 0). \tag{5.7}$$

where t_f is the trial duration (final time). Equations 5.6 and 5.7 show that the optimal control u increases with increasing deviation from the final position $y - y^*$, and with t getting closer to t_f. Note that these theoretical predictions imply that the optimal control is independent of the noise amplitude ν.

To derive the optimal control solution for the two-target task we consider the same dynamical system as for the one-target task (equation 5.1). In the second task the system had to reach one of two targets at locations $y^* = -a$ and $+a$ at a future time t_f. For this task, the end cost is defined by

$$C_f = \tfrac{1}{2} Q_f (|y_f| - a)^2 \qquad (Q_f \geq 0). \tag{5.8}$$

The optimal control is given by

$$u^*(y,t) = -K(t)\left(y + a\,\mathrm{sign}(y)\frac{-\psi_-(y,t) + \psi_+(y,t)}{\psi_-(y,t) + \psi_+(y,t)}\right) \tag{5.9}$$

with

$$\psi_\pm(y,t) = \sqrt{\frac{K(t)Q_u}{Q_f}}\exp\left(-\frac{K(t)}{2\nu}(|y| \pm a)^2\right)\left(\tfrac{1}{2} + \tfrac{1}{2}\mathrm{erf}\left(\sqrt{\frac{Q_f}{2\nu(t_f - t)K(t)Q_u}}\,\mu_\mp(y,t)\right)\right)$$

and

$$\mu_{\mp}(y,t) = \frac{K(t)Q_u}{Q_f}\Big(\mp |y| + Q_f Q_u^{-1} a(t_f - t)\Big). \tag{5.10}$$

(see *Appendix S1* for the derivation). The optimal control in the noiseless condition ($\nu = 0$) is obtained by taking the limit $\nu \to 0$ which gives

$$u^*(y,t) = -K(t)(y - a\,\mathrm{sign}(y)). \tag{5.11}$$

For $\nu = 0$, this model shows that the optimal strategy would be to steer the ball in a straight line from the initial position to the nearest target by exerting a constant control, in agreement with the prediction of deterministic optimal control (Vinter, 2010).

Extended model with position cost The standard model described above assumes that the optimal control solution can be found by minimizing a cost function with a control cost and end cost component, which corresponds to a compromise between minimizing the subject's effort and maximizing the performance. In this study, we investigate whether such a model is sufficient to account for human motor control in a task where subjects have to reach a goal within a particular time interval $[0, t_f]$. Therefore, we extended the standard model by introducing an additional cumulative cost that penalizes deviations between ball position and target position during the trial. This cost criterion tends to steer the ball to the vertical target position y^* well before the final time t_f and is defined by

$$C_y = \int_0^{t_f} \tfrac{1}{2} Q_y V(y(t))dt, \tag{5.12}$$

where

$$V(y(t)) = \Big(\tanh\big(D(y(t) - y^*)\big)\Big)^2 \tag{5.13}$$

for the one-target task where the target was located at $y^* = 0$, and

$$V(y(t)) = \begin{cases} \Big(\tanh\big(D(y(t) + a)\big)\Big)^2 & \text{if } y(t) \le 0 \\ \Big(\tanh\big(D(y(t) - a)\big)\Big)^2 & \text{if } y(t) > 0 \end{cases} \tag{5.14}$$

for the two-target task where the two targets were located at $y^* = -a$ and a. The parameters Q_y and D have positive values. V is zero when the ball's vertical position is equal to the target position. It increases approximately quadratically when the distance between ball and target is small and less than quadratically for larger distances. The position cost is constrained to a finite value when the distance between ball and target is large, eliminating the effect of outliers. This particular shape of V was chosen because previous experiments on sensorimotor learning showed that subjects implicitly use a cost function that is subquadratic for large errors (Körding and Wolpert, 2004), i.e., outliers tend to be ignored. This extended model minimizes the expected cost that is now given by

$$C_{total} = \left\langle \tfrac{1}{2} Q_f y_f^2 + \int_0^{t_f} \tfrac{1}{2} Q_u u(t)^2 dt + \int_0^{t_f} \tfrac{1}{2} Q_y V(y(t)) dt \right\rangle_{y_0} . \tag{5.15}$$

The optimal expected cost-to-go at time t and position y can be written as

$$J(y,t) = -\lambda \ln \left\langle \exp\Big(-\frac{1}{\lambda} C_f(y_f) - \frac{1}{\lambda} \int_t^{t_f} \tfrac{1}{2} Q_y V(y(t')) dt' \Big) \right\rangle_y , \tag{5.16}$$

where C_f is the end cost function, $\lambda = Q_u \nu$, and y satisfies the uncontrolled dynamics $dy = d\xi$ (Kappen, 2005b). The optimal control was calculated by taking the gradient of the optimal expected cost-to-go. A closed form solution for the optimal expected cost-to-go in general does not exist. Therefore, we inferred the optimal control solution approximately by taking the following approach. From the dynamic programming principle (Bellman, 1957) and equation 5.16 it follows that the optimal expected cost-to-go satisfies

$$J(y,t) = -\lambda \ln \left\langle \exp\Big(-\frac{1}{\lambda} J(y_{t+\Delta t}, t+\Delta t) - \frac{1}{\lambda} \int_t^{t+\Delta t} \tfrac{1}{2} Q_y V(y(t)) dt \Big) \right\rangle_y \tag{5.17}$$

for any time step $0 < \Delta t \leq t_f - t$. We approximated this equation by

$$\begin{aligned} J(y,t) &\approx -\lambda \ln \left\langle \exp\Big(-\frac{1}{\lambda} J(y_{t+\Delta t}, t+\Delta t) \Big) \right\rangle_y + \tfrac{1}{2} Q_y V(y) \Delta t \\ &= -\lambda \ln \int_{-\infty}^{\infty} \frac{1}{\sqrt{2\pi\nu\Delta t}} \exp\Big(-\frac{1}{\lambda} J(y', t+\Delta t) - \frac{(y'-y)^2}{2\nu\Delta t} \Big) dy' + \tfrac{1}{2} Q_y V(y) \Delta t. \end{aligned} \tag{5.18}$$

We set $\Delta t = 1/75$ s since the sample rate in the experiments was 75 Hz. With equation 5.18, we computed the optimal expected cost-to-go at any time prior to the end time, starting at the end time where $J(y, t_f) = C_f(y_f)$, and then going backwards in time steps of size Δt. We approximated the spatial integral in equation 5.18 by a sum that was obtained by discretizing space into steps of size $dy' = 0.007$. The optimal control was derived by taking the gradient of the optimal expected cost-to-go:

$$u(y,t) = -\frac{1}{Q_u} \frac{\partial J(y,t)}{\partial y}. \tag{5.19}$$

Since the cost function of this model contains the position cost as an additional component, we call this model the 'extended model'. We call the model with end cost only the 'standard model'. The extended model gives the same solution as the standard model if the position cost parameter Q_y is zero (equations 5.12 and 5.13). For $Q_y > 0$, the extended model gives solutions which cannot be obtained by the standard model.

Data analysis In most of the trials, subject S5 showed a fragmentary, discontinuous control signal in which periods of high control were alternated with periods of no control throughout the trial. This was especially true for the noiseless condition. The other subjects showed a rather smooth, continuous control signal in most of the trials. Since the optimal control models assume a continuous control signal, subject S5 was excluded from the analysis.

For each task, subject, and noise amplitude we determined the model performance of the extended model with position cost and that of the standard model with end cost only using a 100-fold cross-validation. From each block with 100 trials, 50 trials were randomly drawn. From this subset of 50 trials, 45 trials were randomly selected to train both models to find the optimal model parameters. This was done by minimizing the mean square error (MSE) between the optimal control u^* according to the model and the actual control u in the training data:

$$\mathrm{MSE} = \frac{1}{N_s}\sum_{s=1}^{N_s}\frac{1}{N_t}\sum_{t=t_a}^{t_b}\Big(u_s(t+\tau) - u^*(y_s(t), t|\Theta)\Big)^2, \tag{5.20}$$

where $u_s(t+\tau)$ is the control according to the data at time $t+\tau$ in trial s, $y_s(t)$ is the position of the ball at time t in trial s, $u^*(y_s(t), t|\Theta)$ is the model control at time t and position $y_s(t)$ given the model parameters Θ, and $N_s = 45$ represents the number of trials. For both models we set $Q_u = 1$, resulting in $\Theta = Q_f$ for the standard model and $\Theta = \{Q_f, Q_y, D\}$ for the extended model. We introduced a sensorimotor delay τ of 200 ms to take into account the time that it typically took for subjects to respond to changes in ball position during the task (Day and Lyon, 2000; Franklin and Wolpert, 2008). The results did not depend crucially on the value of the time delay (see *Discussion*). The summation over time t runs from $t_a = 0.8$ s to $t_b = 2.8$ s, which corresponds to $N_t = 150$ since the sample rate was 75 Hz. The lower bound of 0.8 s was chosen to include only responses well after the subjects' reaction time, which had a median value of 0.47 s (25th and 75th percentile was 0.31 s and 0.68 s, respectively). The upper bound of 2.8 s was chosen to account for the sensorimotor delay (0.2 s). Each model was tested on the remaining five trials, yielding a test error for the standard and the extended model. The test error was computed from equation 5.20, with summation over the test samples ($N_s = 5$), and given the model parameters Θ that minimized the mean square error between the model and the training data.

The paired difference between the test errors of both models was considered as an estimate of the performance of the extended model with position cost relative to the standard model with end cost only. Therefore, we performed a two-sided sign test under the null hypothesis that the paired differences 'test error of standard model' minus 'test error of extended model' have median zero, against the alternative that they do not have median zero at the 5% significance level.

5.3 Results

Responses in the one-target task In the one-target task, subjects were asked to steer a virtual ball from the left side of the screen toward a single goal at the right (figure 5.1a). As an example, figure 5.1 shows the ball position (panel c) and corresponding control (panel

e) of a representative subject (S6) for $\nu = 0.009$. Each line represents a single trial (total 100 trials) starting at a position y in the range between -0.5 and 0.5.

The average observed behavior was obtained by averaging the single trials for each subject and condition (figure 5.2). Since the task was symmetric relative to $y = 0$, we did not find systematic differences in behavior between trials starting at $y < 0$ and $y > 0$ for the majority of subjects and conditions (see below). Therefore, we calculated the average over trials (solid gray line) by first inverting the sign of the position and corresponding control signal for trials starting at $y < 0$ and then taking the average over all trials. The shaded area represents the standard deviation. Subject S4 showed different behavior between trials starting at $y > 0$ and trials starting at $y < 0$ for $\nu > 0$. Therefore, the results of this subject should be interpreted as the average behavior between trials starting at $y > 0$ and trials starting at $y < 0$.

Since subjects could only manipulate the vertical position of the ball, they always reached the horizontal target position (i.e., the right boundary of the screen) at $t = 3$ s. However, they were free in choosing the time at which they reached the vertical target position $y^* = 0$. The time at which subjects reached the vertical target position differed substantially among subjects. This difference in behavior is most pronounced when considering the average ball trajectories for the noiseless condition ($\nu = 0$, first row). Subject S6 is an example of a subject who reached $y^* = 0$ very early (at about 1.5 s) which was well before the final time of 3 s, resulting in an average ball trajectory that was curved. The corresponding control (fifth row) peaked just before $t = 1$ s and gradually decayed, reaching values close to zero after about 1.5 to 2 s. Subject S7 shows different behavior. This subject reached the target very close to the deadline $t_f = 3$ s by exerting a more or less constant control. The other subjects (S1–S4, S8) showed intermediate behavior, i.e., they reached $y^* = 0$ between 1.5 and 3 s.

The strategy subjects used to steer the ball toward the target is consistent across different noise levels for the majority of subjects (S1–S3, S6–S8). Subject S4 is an exception to this consistency since he reached the vertical target position relatively early in the noiseless condition, but reached the target close to the final time when the noise was increased ($\nu > 0$). Note that all subjects had a reaction time of about 0.5 s before they started moving the ball.

Model performance for the one-target task The black dashed and solid line in figure 5.2 represent the average model fit of the standard model and of the extended model with position cost, respectively. In the first 0.5 s, the control was set to zero to account for the subjects' reaction time. The majority of subjects reached the vertical target position well before the final time of 3 seconds. This behavior is inconsistent with the standard model (dashed line) which predicted a constant control and a straight trajectory reaching the target approximately at $t_f = 3$ s. The predictions by the extended model (solid line) were in close agreement with the curved ball trajectory. This means that the position cost, which is a function of the distance between the ball and the target position during the trial, is essential to fit the behavior of the majority of the subjects.

Subject S7 (all noise levels) and subject S4 ($\nu > 0$) ended at the vertical target position close to the final time by applying a more or less constant control. This strategy was consistent with the standard model, where subjects minimized the control cost and end cost, but not the position cost. Fitting both models to the data of these subjects gave more

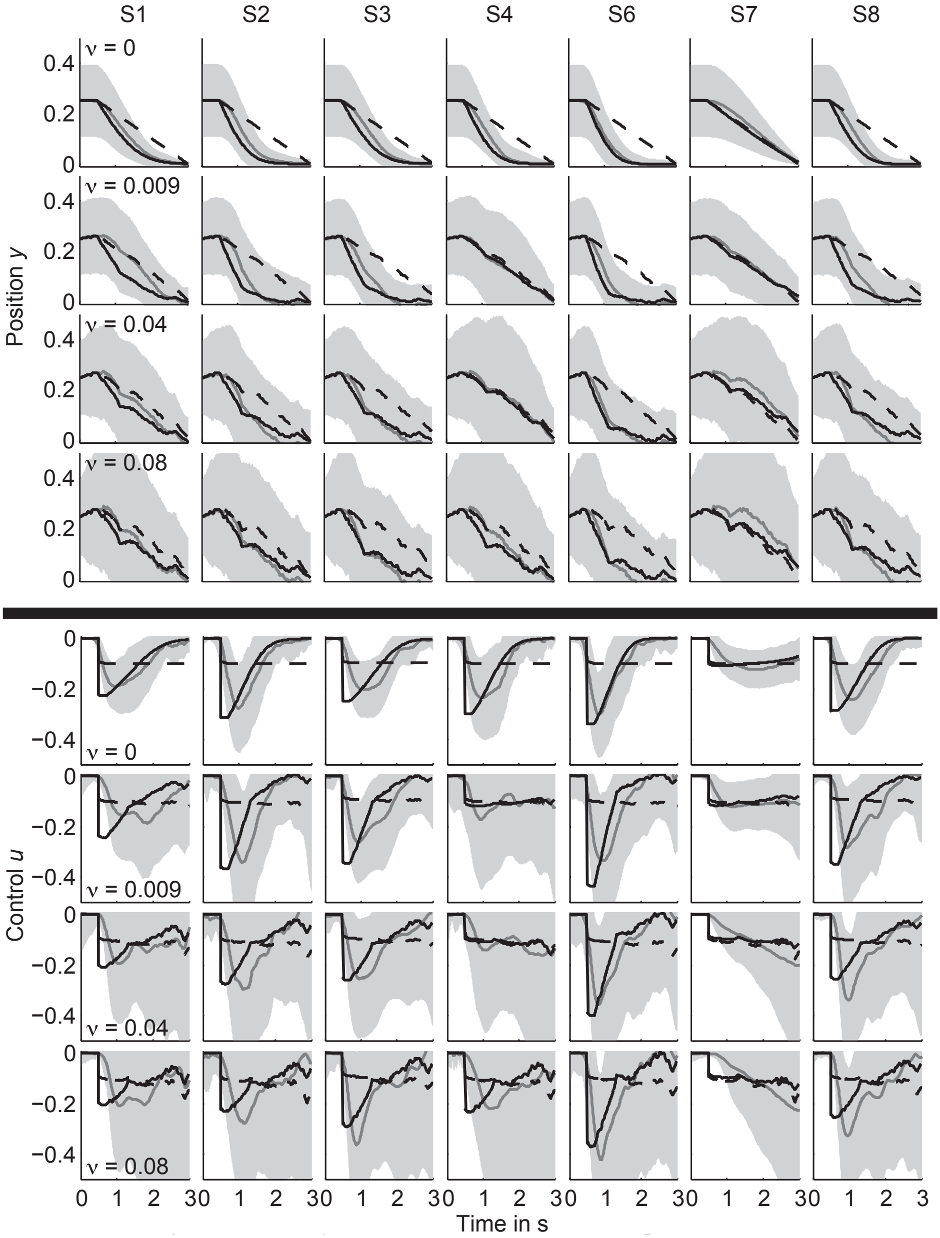

Figure 5.2 Behavior and model predictions for the one-target task. Top panels: average ball position displayed as mean (gray solid line) and standard deviation (gray shaded area) for all noise amplitudes (rows) and subjects (columns). The black dashed and solid line represent the average fit of the standard model and the extended model, respectively. Bottom panels: same for the control signal. Subject S5 was discarded (see *Methods*).

or less the same result for both models. The reason is that for these cases the optimal value for parameter Q_y in the extended model (see equation 5.15) was close to zero, which reduced the extended model to the standard model.

To investigate whether the extended model with position cost gave a better prediction of the data than the standard model with end cost only, we computed the test error for each model, which provided a measure how well the model fitted the data (see *Methods* for details). Figure 5.3 shows the test error of the standard model minus the test error of the extended model ('test error difference') for all subjects and noise amplitudes. Values are given as the median over 100 validation runs. The lower and upper error bars represent the 25th and 75th percentile, respectively. Thus, a positive value means that the extended model gave a better prediction than the standard model. A value of zero means that there was no difference between the models. Conditions for which the extended model gave a significantly better prediction than the standard model are indicated by $*$ ($p < 0.05$) or $**$ ($p < 0.01$).

For all subjects and noise amplitudes, the predictions by the extended model were better in agreement with the data than the predictions by the standard model, even when the test error difference was close to zero. The reason is that we used a non-parametric sign-test, which ranks the values according to their sign without making any assumptions on the underlying distribution. The results of figure 5.3 reveal conditions for which the test error difference was positive and conditions for which this value was virtually zero. A positive test error difference means that including the position cost in the model improved the model prediction, corresponding to the strategy of steering the ball toward the desired target position well before the final time. A test error difference near zero means that the standard model with end cost only is sufficient to describe the observed behavior and that subjects steer the ball in a straight line reaching the target approximately at the time limit.

For subjects S1–S3, S6 and S8 the test error difference was clearly positive for all noise amplitudes. Thus, for these subjects the behavior in the one-target task can best be described by a model that includes the position cost in its cost function, irrespective of the level of uncertainty in the task. Subject S4 showed a positive test error difference for $\nu = 0$, whereas for $\nu > 0$ this value was virtually zero. Thus, this subject chose different strategies based on the level of uncertainty. For subject S7, the test error difference was virtually zero for all noise amplitudes, which means that including the position cost hardly improved the model prediction. This behavior was consistent across all noise amplitudes.

Responses in the two-target task In the previous sections, we found that a standard optimal control model with a control cost component and end cost component was insufficient to describe the behavior found in the one-target experiment for the majority of subjects. We found that the extended model gave a good fit of the data of the one-target experiment. Here, we investigate whether the extended model could also correctly predict the behavior in other time-constrained tasks. Therefore, we designed a second task in which subjects had to move the ball to either of two targets (see *Methods* for details). We selected a new group of seven subjects (S6–S12), three of which (S6–S8) also participated in the one-target task. The remaining four subjects (S9–S12) were naive with respect to the aim and procedure of the experiment to check whether the results of the second task could have been influenced by participation in the first task. As an example, figure 5.1 shows the

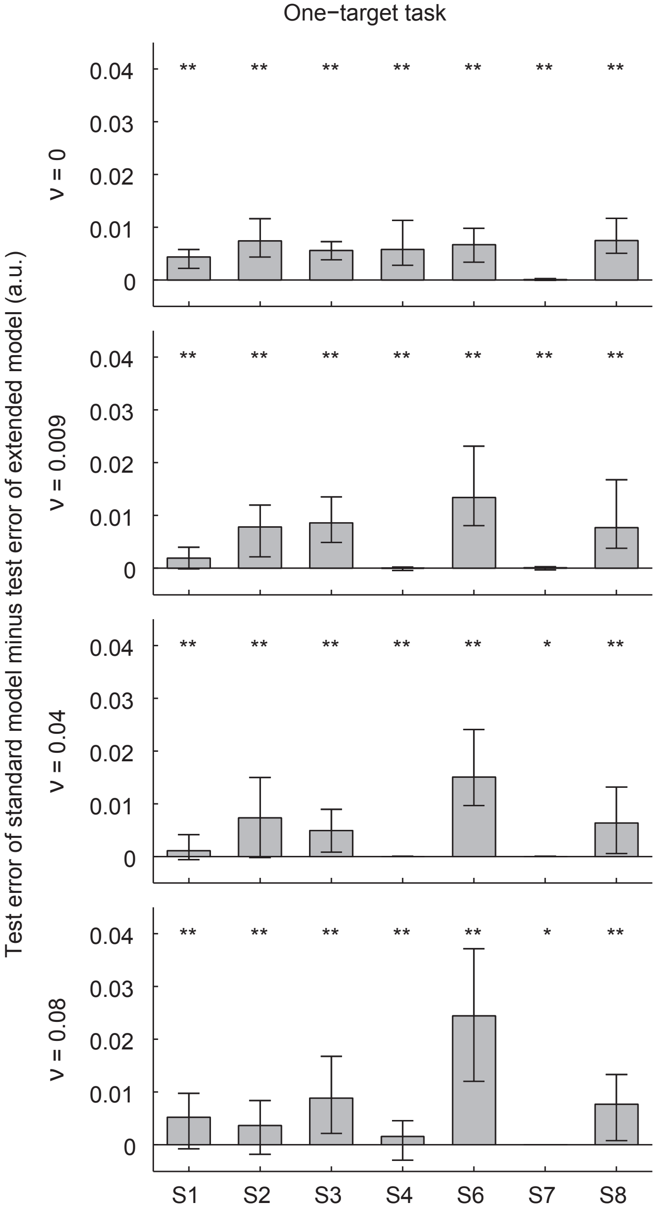

Figure 5.3 Model performance for the one-target task. Test error of standard model minus test error of extended model for all subjects and noise amplitudes. Values are given as the median over 100 cross-validation runs. The lower and upper error bars represent the 25th and 75th percentile, respectively. A positive value means that the extended model gave a better fit than the standard model. A value of zero means that there was no difference between the models. Conditions for which the extended model gave a significantly better prediction than the standard model are indicated by $*$ ($p < 0.05$) or $**$ ($p < 0.01$). Subject S5 was discarded (see *Methods*).

ball position (panel d) and corresponding control (panel f) of a representative subject (S6) for $\nu = 0.009$. Each line represents a single trial (total 100 trials) starting at a position $y = 0$.

The average observed behavior was obtained by averaging the single trials for each subject and condition (figure 5.4). Since the task was symmetric relative to $y = 0$, we did not find systematic differences in control for trials in which subjects aim for the upper and lower target, except for the sign. The only exception was subject S8, who steered the ball to the upper target only in the noiseless condition. We took the average over trials after inverting the sign of the position and corresponding control signals aiming for the lower target ($y = -0.5$), as if all trials were made to the upper target ($y = +0.5$). The gray line and shaded area represent the mean and standard deviation over 100 trials, respectively.

The time at which subjects reached the vertical target position differed substantially among subjects. This difference in behavior is most pronounced when considering the average ball trajectories for the noiseless condition ($\nu = 0$, first row). Subject S6 is an example of a subject who reached $y^* = 0$ very early (at about 2 s) which was well before the final time of 3 s, resulting in an average ball trajectory that was curved. The corresponding control (fifth row) peaked at about $t = 1$ s and gradually decayed, reaching values close to zero after about 1.5 to 2 s. Subjects S9 and S10 show different behavior. These subjects reached the target very close to the deadline $t_f = 3$ s, resulting in a straight path, by exerting a more or less constant control. The other subjects (S7, S8, S11, S12) showed intermediate behavior, i.e., they reached $y^* = 0$ between 1.5 and 3 s.

The strategy subjects used to steer the ball toward the target is consistent across different noise levels for subjects S6, S8 and S12. Subjects S7 and S11 reached the vertical target position relatively early in the noiseless condition, but reached the target close to the final time when the noise was increased ($\nu > 0$). Subject S9 shows the opposite behavior. Subject S10 is consistent across different noise levels except for $\nu = 0.009$, where this subject started moving the ball toward the target relatively late in the trial. All subjects had a reaction time of about 0.5 s before they started moving the ball.

Model performance for the two-target task The black dashed and solid line in figure 5.4 represent the average model fit of the standard model and of the extended model with position cost, respectively. In the first 0.5 s, the control was set to zero to account for the subjects' reaction time. In this task, we found similar results as for the one-target task. The majority of subjects reached the vertical target position well before the final time of 3 seconds, which was inconsistent with the standard model (dashed line) but consistent with the extended model (solid line). This means that also for the two-target task, the position cost is essential to fit the behavior of the majority of the subjects. In some conditions subjects ended at the vertical target position close to the final time (e.g. S9, S10 for $\nu = 0$; S7, S10 for $\nu = 0.08$), which was consistent with the standard model where subjects minimized the control cost and end cost, consistent with the standard model where subjects minimized the sum of control cost and end cost, and where no position cost appeared.

To investigate whether the extended model gave a better prediction of the data than the standard model, we repeated the analysis that we used for the one-target task. Figure 5.5 shows the test error of the standard model minus the test error of the extended model for all subjects and noise amplitudes. Values are given as the median over 100 validation runs. The lower and upper error bars represent the 25th and 75th percentile, respectively.

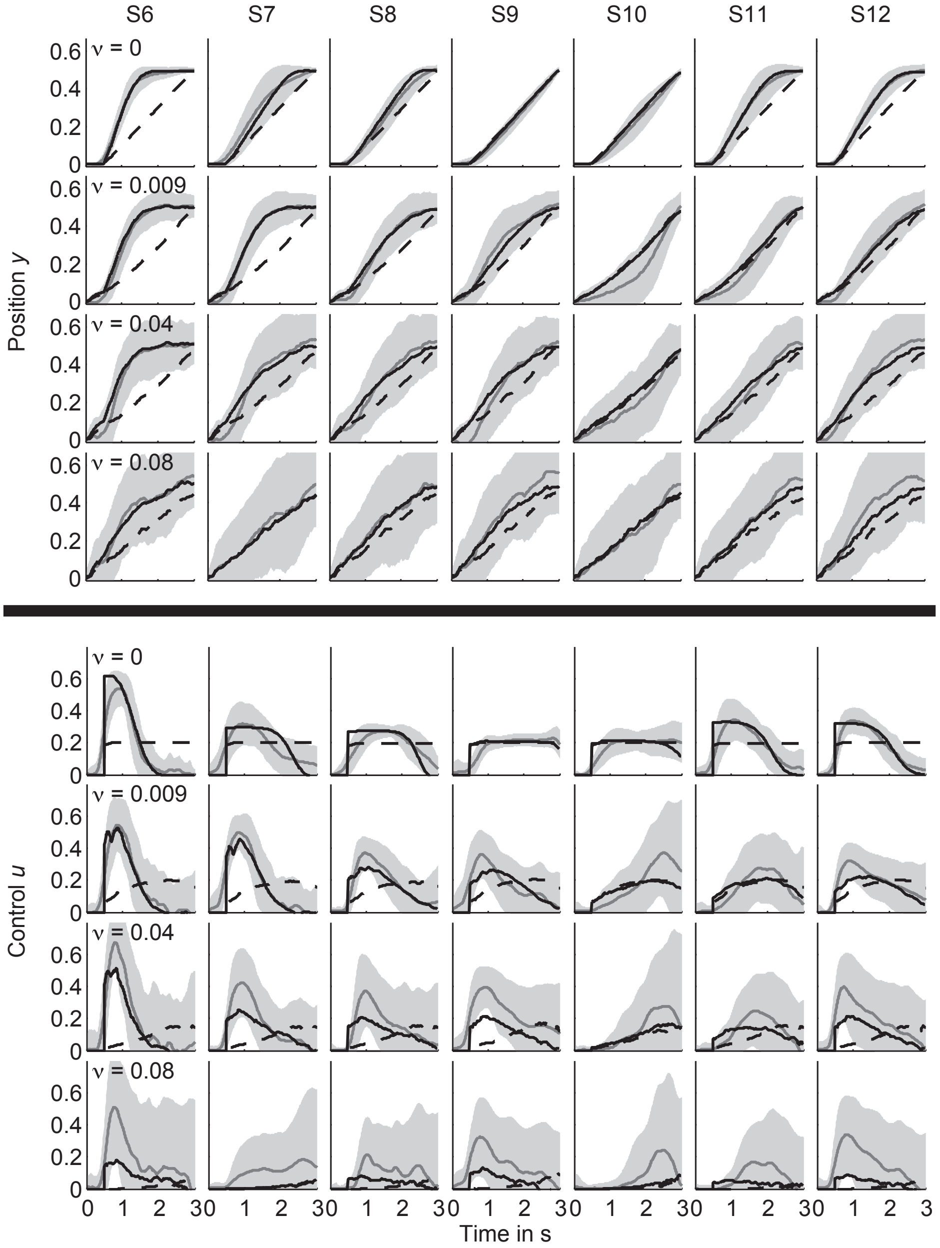

Figure 5.4 Behavior and model predictions for the two-target task. See figure 5.2 for details.

Conditions for which the extended model gave a significantly better prediction than the standard model are indicated by ** ($p < 0.01$).

For all subjects and noise amplitudes, the predictions by the extended model were significantly better in agreement with the data than the predictions by the standard model, even when the test error difference was close to zero. This result is in agreement with that of the one-target task (see figure 5.3). For subjects S6, S8, S11 and S12 the test error difference was clearly positive for all noise amplitudes, corresponding to a strategy in which the ball was steered toward the desired target position well before $t_f = 3$ s. Subject S10 showed a test error difference close to zero for all noise amplitudes, corresponding to a strategy in which the ball moved in a straight line and arrived at the target position approximately at $t_f = 3$ s. For subject S7, the test error difference was close to zero for $\nu = 0.08$, but positive for the other noise amplitudes. Considering the group of subjects that participated in both experiments (i.e., S6–S8), we conclude that for S6 and S8, the behavior in the two-target task was similar as for the one-target task.

5.4 Discussion

In this study, we used optimal control theory to predict human motor behavior in two different time-constrained motor tasks. We investigated whether minimizing the usual cost function consisting of a control and end cost component is sufficient to describe the observed behavior. Therefore, we tested eight subjects in the one-target task in which they had to hit a target at a final time of $t = 3$ s. As a null hypothesis, we postulated the standard model that assumes that subjects minimize the integrated quadratic control and the squared distance between the ball and the target at the end of the trial. We extended the standard model by including a position cost component in the cost function, which penalized deviations between the position of the ball and the target throughout the trial. This cost component ensures that subjects steer the ball to the target position well before the final time. Both models were trained on a subset of the data to compute the model parameters, and tested on the remaining data to obtain the model performance. The results show that the majority of subjects steer the ball such that they reach the vertical target position well before the final time. This behavior was consistent across different noise levels. For all subjects and noise levels, the predictions by the extended model were better in agreement with the data than the predictions by the standard model. This result rejects our hypothesis that a simple cost function representing a trade-off between effort and performance is sufficient to describe the observed behavior. To investigate whether the extended model is generic, we tested another group of subjects in the two-target task in which they had to hit one of two targets at the fixed final time. For this task, the predictions by the extended model were also in good agreement with the experimental data, much better than for the standard model.

Recently, Nagengast et al. (2010) used a similar task in which subjects controlled a virtual ball undergoing Brownian motion (noise) towards a target that had to be reached at a final time of one second. Subjects were required to minimize an explicit cost that was a combination of the final positional error of the ball (end cost) and the integrated control cost. They proposed the use of a risk-sensitive optimal controller that incorporated movement cost variance either as an added cost (risk-averse controller) or as an added value (risk-

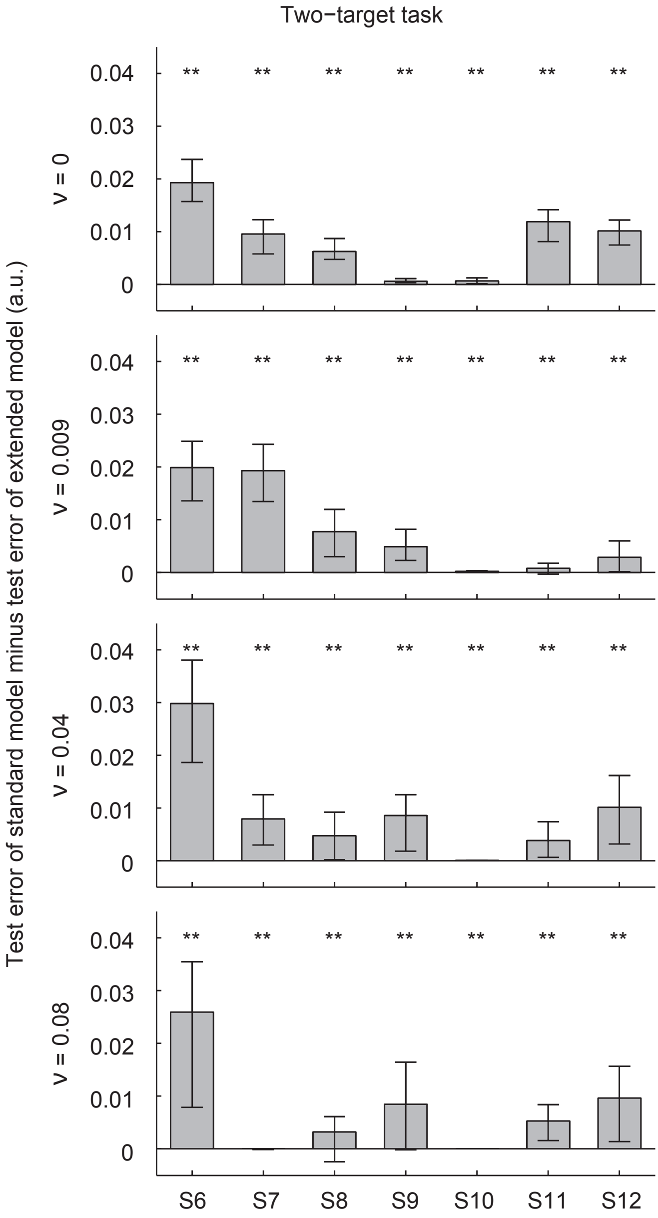

Figure 5.5 Model performance of the two-target task. See figure 5.3 for details.

seeking controller). This raises the question whether our results could also be explained by risk sensitivity. Therefore, we fitted the risk-sensitive model of Nagengast et al. to our data. For the conditions with stochastic dynamics ($\nu > 0$), we reproduced their finding that this risk-sensitive model fitted the data better than the risk-neutral model, which is equal to the standard model in this study (see *Appendix*). However, in our experiment, we also included a noiseless condition ($\nu = 0$) in which the movement of the ball was completely deterministic. For the noiseless condition, a risk-sensitive model gives exactly the same predictions as a risk-neutral model. Our results show that for the noiseless condition, a risk-neutral model that minimizes the control and the final positional error is insufficient to predict the observed behavior. Thus, our results cannot be explained by risk sensitivity.

How can we explain that subjects show a different behavior in the task of Nagengast et al. (2010) and our one-target task, while both tasks were rather similar? In the experiment of Nagengast et al. (2010), subjects received feedback about the control cost and end cost during each trial, and about the average total cost across trials. Their subjects were requested to minimize the sum of the control cost and end cost, corresponding to the standard model. If subjects would steer the ball to the vertical target position before the final time, their control cost would increase. Since subjects were requested to minimize the control cost and end cost, they adjusted their behavior such that it was in agreement with the standard model. In addition, although their task was very similar to ours, the dynamics of the system differed substantially. We used a first order dynamics to relate the control to the ball position, that is, a control action changed the vertical velocity of the ball (equation 5.1). Nagengast et al. (2010) used a second order dynamics in which a control action acted as a force on a frictionless mass (the ball) causing it to accelerate or decelerate. In our experiment, subjects could move the ball with the joystick toward a desired position, which could then be maintained by simply exerting no control. In their experiment, subjects could move the ball toward a desired position, but in order to maintain that position, subjects had to decelerate the ball by exerting control opposite to the movement direction. This may have affected the subjects' control strategy.

Braun et al. (2009a) have used a cumulative position-dependent cost function to model reaching tasks. In their study no final time was assumed, but instead, the movement time resulted as a consequence of the cumulative position cost. Even though they used an infinite horizon model, it suggests that the cumulative position cost may have the same effect as in our study. Therefore, we implemented an infinite horizon model in our experiments (see *Appendix*). We found that the optimal control in the infinite horizon model is similar to the optimal control in the finite horizon model. This demonstrates that introducing a position cost consistently predicts that subjects steer the ball such that it arrives at the vertical target position before the final time, irrespective of the time horizon.

In our experiment, we asked subjects to hit the target but we did not gave any instructions as to whether the movement should meet any criteria. This raises the question why subjects would minimize the position error over time. Todorov (2004) stated that the cost that is relevant to the sensorimotor system may not directly correspond to our intuitive understanding of 'the task' and so its detailed form should be considered a relatively free parameter. Thus, the explicit instruction to the subjects of the task's goal may not necessarily reflect the goal that the sensorimotor system implicitly tries to achieve. This is consistent with our results showing that the subjects' strategy can be predicted by a model that also minimizes the position cost, although this was not an explicit aim of the task.

However, this does not explain what the cause of this position cost might be. One likely explanation is that maintaining a constant control throughout the trial is more difficult than producing a large control in the beginning of the trial and some corrective movements at the end. Thus, if the trial duration is large, a control strategy that spreads the control equally over the available time would probably be extremely difficult to achieve, even though this strategy is the optimal strategy according to the standard model. The trial duration in our experiments was set to 3 s, which is rather long for a typical hand or arm movement. This suggests that a relatively long trial duration causes subjects to move faster toward the target compared to short trial durations. This hypothesis could be tested in future work. An alternative explanation is that subjects avoid the risk of missing the target and therefore steer the ball toward the target before the final time.

One can argue that including a third component in the cost function of the extended model will by itself give a better prediction since it adds two additional free parameters compared to the standard model (i.e., Q_f for the standard model; Q_f, Q_y and D for the extended model; $Q_u = 1$ for both models). However, the model predictions do not depend on the number of free parameters since we applied cross-validation to both models. The additional free parameters in the extended model could cause so-called overfitting when these parameters were not relevant for the task. In that case, the extended model would give a worse fit than the standard model, resulting in negative values of the test error differences in figures 5.3 and 5.5. At the contrary, these figures show that on average, the extended model gives a significantly better prediction than the standard model.

The extended model includes one fixed parameter, the sensorimotor delay τ, which was set to 200 ms (see *Methods*). To investigate the sensitivity of the model to this parameter, we also did the cross-validation procedure for $\tau = 150$ ms, which was equal to the value chosen by Nagengast et al. (2010). Similar to the extended model with $\tau = 200$ ms, we calculated the test error of the standard model minus the test error of the extended model, yielding 100 error values for each of 64 conditions (8 subjects × 4 noise amplitudes × 2 tasks). For each condition, we tested whether the median obtained by the model with $\tau = 150$ ms was equal to the median obtained by the model with $\tau = 200$ ms (Mann-Whitney U test). For six conditions, we found a significant difference ($0.02 < p < 0.05$). For the remaining 58 conditions, the difference was not significant ($p > 0.05$). These results show that the extended model is not sensitive to the precise value of the sensorimotor delay within the range of 150 to 200 ms for the majority of conditions tested in this study.

In our model, we included a quadratic end cost and a position cost that was quadratic only locally (around the target position) and leveled off further away from the target to reduce the effect of outliers. Note that in this experiment, the difference in model prediction between a quadratic or a locally quadratic end cost function will be small, since the ball's final position is scattered around the target position (see figures 5.2 and 5.4, first row) which is within the quadratic region of both functions. The position cost, however, depends on the ball's position relative to the target position throughout the trial. Initially, the ball's position is in general relatively far from the desired target position, resulting in large errors. For sensorimotor learning, it has been shown that people use a cost function that increases approximately quadratically for small errors but less than quadratically for large errors (Körding and Wolpert, 2004). Therefore, we used a $\tanh^2$-function (equation 5.13 and 5.14) which fulfills these criteria and which sets an upper bound on the position cost.

For the two-target task, the standard model gives an additional, more subtle theoretical prediction. In the beginning of the trial, it is best to steer towards $y = 0$ (between the targets) and delay the choice which target to aim for if the noise amplitude is large. In our experiments, the standard model predicts only a very small control toward $y = 0$ in the first 0.5 seconds, even for the highest noise amplitude ($\nu = 0.08$). Thus, according to the standard model this so-called symmetry breaking is barely measurable in our experiments. Moreover, the symmetry breaking vanishes when the position cost is introduced. This explains why we found that subjects never steered the ball away from the target towards $y = 0$ during the first part of the trial, even not for the highest noise amplitude.

The results of our study show that a model that only minimizes control effort and maximizes performance cannot describe human motor behavior in a time-constrained sensorimotor task. A model that also accounts for the deviation from the goal throughout the task execution gives a significantly better fit the observed behavior.

5.5 Appendix

In this appendix, we derive a risk-sensitive optimal control model for the one-target and two-target task. We discuss the model performance. As an alternative to the finite horizon models presented in this study, we discuss the application of infinite horizon models.

Derivation of the risk-sensitive model In this section, we derive the risk-sensitive optimal control for the one-target and two-target task. For the basic model with end cost only, this solution can be obtained analytically. The dynamics of the control problem is given by the stochastic differential equation $dy = u(y,t)dt + d\xi$ (see equation 5.1). The total cost function of this control problem is equal to the sum of an end cost function and a cumulative control cost function, resulting in

$$C_{total} = \left\langle C_f(y_f) + \int_0^{t_f} \tfrac{1}{2} Q_u u(y(t),t)^2 dt \right\rangle_{y_0},$$

(see equation 4) with end cost function

$$\begin{aligned} C_f(y_f) &= \begin{cases} \tfrac{1}{2} Q_f (y_f + a)^2 & \text{if } y_f \leq 0 \\ \tfrac{1}{2} Q_f (y_f - a)^2 & \text{if } y_f > 0 \end{cases} \\ &= \tfrac{1}{2} Q_f (|y_f| - a)^2 \end{aligned}$$

with $a \geq 0$. Note that $a = 0$ gives the control problem for the one-target task and $a = 0.5$ for the two-target task. As derived in Kappen (2005b), the optimal cost-to-go satisfies

$$J_\theta(y,t) = \begin{cases} \langle C_f(y_f) \rangle_y & \text{if } \theta = \frac{1}{\nu Q_u} \\ -\frac{\nu Q_u}{1-\theta \nu Q_u} \ln Z_\theta(y,t) & \text{if } \theta \neq \frac{1}{\nu Q_u}, \end{cases}$$

where

$$Z_\theta(y,t) = \Big\langle \exp\Big(- \frac{1-\theta\nu Q_u}{\nu Q_u} C_f(y_f)\Big)\Big\rangle_y$$

and y represents the path for uncontrolled dynamics. A general derivation of the optimal cost-to-go in stochastic optimal control problems can be found in Kappen (2005b). First, we consider the case $\theta = \frac{1}{\nu Q_u}$. For this case, the optimal cost-to-go can be rewritten by substituting the end cost function, which yields

$$\begin{aligned} J_\theta(y,t) &= \Big\langle \tfrac{1}{2} Q_f\big(|y_f| - a\big)^2 \Big\rangle_y \\ &= \tfrac{1}{2} Q_f\Big(\langle y_f^2\rangle_y - 2a\langle |y_f|\rangle_y + a^2\Big). \end{aligned}$$

The expectation value $\langle y_f^2\rangle_y$ is given by

$$\langle y_f^2\rangle_y = \Big\langle \Big(y + \int_t^{t_f} d\xi\Big)^2 \Big\rangle_y = y^2 + \nu(t_f - t).$$

The distribution of $|y_f|$ conditioned on y is a reflected Brownian motion (Karatzas and Shreve, 2000) and reads

$$\mathbb{P}\Big(|y_f| \in dy' \Big| y\Big) = \frac{1}{\sqrt{2\pi\nu(t_f - t)}}\Big(\exp\Big(-\frac{(|y| + y')^2}{2\nu(t_f - t)}\Big) + \exp\Big(-\frac{(|y| - y')^2}{2\nu(t_f - t)}\Big)\Big)dy' \quad (y \geq 0).$$

We use this distribution to find the expectation value $\langle |y_f|\rangle_y$, which is given by

$$\begin{aligned} \langle |y_f|\rangle_y &= \int_0^\infty y' \mathbb{P}\Big(|y_f| \in dy' \Big| y\Big) \\ &= \frac{2\nu(t_f - t)}{\sqrt{2\pi\nu(t_f - t)}} \exp\Big(-\frac{y^2}{2\nu(t_f - t)}\Big) + y \operatorname{erf}\Big(\frac{y}{\sqrt{2\nu(t_f - t)}}\Big). \end{aligned}$$

The optimal control u^* is proportional to the partial derivative of the optimal cost-to-go $J_\theta(y,t)$ to y and is given by

$$\begin{aligned} u^*(y,t) &= -\frac{1}{Q_u}\frac{\partial}{\partial y} J_\theta(y,t) \\ &= \frac{Q_f}{Q_u}\Big(\operatorname{erf}\Big(\frac{y}{\sqrt{2\nu(t_f - t)}}\Big)a - y\Big). \end{aligned}$$

Next, we consider the case $\theta \neq \frac{1}{\nu Q_u}$. $Z_\theta(y,t)$ is a path integral that satisfies

$$
\begin{aligned}
Z_\theta(y,t) &= \left\langle \exp\Big(-\frac{Q_f(1-\theta\nu Q_u)}{2\nu Q_u}(|y_f|-a)^2\Big)\right\rangle_y \\
&= \int_0^\infty \exp\Big(-\frac{Q_f(1-\theta\nu Q_u)}{2\nu Q_u}(y'-a)^2\Big)\mathbb{P}\Big(|y_f| \in dy' \Big| y\Big) \\
&= \psi_-(y,t) + \psi_+(y,t),
\end{aligned}
$$

where

$$
\psi_\pm(y,t) = \frac{1}{\sqrt{2\pi\nu(t_f-t)}}\int_0^\infty \exp\Big(-\frac{Q_f(1-\theta\nu Q_u)}{2\nu Q_u}(y'-a)^2 - \frac{(|y|\pm y')^2}{2\nu(t_f-t)}\Big)dy'.
$$

We define two new functions:

$$
K(t) = \frac{Q_f}{Q_u + (1-\theta\nu Q_u)Q_f(t_f-t)}
$$

and

$$
\mu_\mp(y,t) = \frac{K(t)Q_u}{Q_f}\Big(\mp |y| + (1-\theta\nu Q_u)Q_fQ_u^{-1}(t_f-t)a\Big).
$$

We use these functions to rewrite the expression for $\psi_\pm(y,t)$, which yields

$$
\begin{aligned}
\psi_\pm(y,t) =& \frac{1}{\sqrt{2\pi\nu(t_f-t)}}\exp\Big(-\frac{K(t)(1-\theta\nu Q_u)}{2\nu}(|y|\pm a)^2\Big) \\
&\int_0^\infty \exp\Big(-\frac{Q_f(y'-\mu_\mp(y,t))^2}{2\nu(t_f-t)K(t)Q_u}\Big)dy' \\
=& \sqrt{\frac{K(t)Q_u}{Q_f}}\exp\Big(-\frac{K(t)(1-\theta\nu Q_u)}{2\nu}(|y|\pm a)^2\Big) \\
&\Big(\tfrac{1}{2} + \tfrac{1}{2}\mathrm{erf}\Big(\sqrt{\frac{Q_f}{2\nu(t_f-t)K(t)Q_u}}\mu_\mp(y,t)\Big)\Big)
\end{aligned}
$$

under the condition that

$$
0 < Q_u + (1-\theta\nu Q_u)Q_f(t_f-t).
$$

Otherwise $\psi_\pm(y,t) = \infty$. The optimal control is given by

$$
\begin{aligned}
u^*(y,t) &= \frac{\partial}{\partial y}\frac{\nu}{1-\theta\nu Q_u}\ln Z_\theta(y,t)\\
&= Z_\theta(y,t)^{-1}\Big(\frac{\nu}{1-\theta\nu Q_u}\frac{\partial}{\partial y}\psi_-(y,t)+\frac{\nu}{1-\theta\nu Q_u}\frac{\partial}{\partial y}\psi_+(y,t)\Big).
\end{aligned}
$$

Finally, we rewrite the optimal control in terms of $K(t)$ and $\psi_\pm(y,t)$. Let

$$
\begin{aligned}
&\frac{\nu}{1-\theta\nu Q_u}\frac{\partial}{\partial y}\psi_\pm(y,t)\\
&= -K(t)\Big(y \pm a\ \mathrm{sign}(y)\Big)\psi_\pm(y,t)\mp\\
&\quad\frac{\mathrm{sign}(y)}{\sqrt{2\pi\nu(t_f-t)}}\frac{K(t)Q_u}{Q_f}\frac{\nu}{1-\theta\nu Q_u}\exp\Big(-\frac{K(t)(1-\theta\nu Q_u)(|y|\pm a)^2}{2\nu}-\frac{Q_f\mu_\mp(y,t)^2}{2\nu(t_f-t)K(t)Q_u}\Big)\\
&= -K(t)\Big(y \pm a\ \mathrm{sign}(y)\Big)\psi_\pm(y,t)\mp\\
&\quad\frac{\mathrm{sign}(y)}{\sqrt{2\pi\nu(t_f-t)}}\frac{K(t)Q_u}{Q_f}\frac{\nu}{1-\theta\nu Q_u}\exp\Big(-\frac{|y|^2}{2\nu(t_f-t)}-\frac{1-\theta\nu Q_u}{2\nu Q_u}Q_f a^2\Big).
\end{aligned}
$$

After substituting this equation we find

$$
u^*(y,t) = -K(t)\Big(y + a\ \mathrm{sign}(y)\frac{-\psi_-(y,t)+\psi_+(y,t)}{\psi_-(y,t)+\psi_+(y,t)}\Big).
$$

We can verify that this equation equals the case $\theta = \frac{1}{\nu Q_u}$, since

$$
\lim_{\theta\to\frac{1}{\nu Q_u}}\psi_\pm(y,t) = \tfrac{1}{2}+\tfrac{1}{2}\mathrm{erf}\Big(\frac{\mp|y|}{\sqrt{2\nu(t_f-t)}}\Big).
$$

The optimal control for the case $\theta = \frac{1}{\nu Q_u}$ is given by

$$
\begin{aligned}
\lim_{\theta\to\frac{1}{\nu Q_u}} u^*(y,t) &= -\frac{Q_f}{Q_u}\Big(y - a\ \mathrm{sign}(y)\ \mathrm{erf}\Big(\frac{|y|}{\sqrt{2\nu(t_f-t)}}\Big)\Big)\\
&= -\frac{Q_f}{Q_u}\Big(y - a\ \mathrm{erf}\Big(\frac{y}{\sqrt{2\nu(t_f-t)}}\Big)\Big).
\end{aligned}
$$

Note that the optimal control for the standard model is found by taking $\theta = 0$.

Model performance of the risk-sensitive model In the standard model, the performance criterion of minimizing the expected cost-to-go (equation 5.4) assumes that the certainty equivalent, i.e., the maximal cost one is willing to pay for certain rather than the uncertain cost associated to the control problem, equals the expected cost-to-go. The resulting control problem is said to be risk-neutral. When the certainty equivalent is higher or lower than the expected cost-to-go, the performance criterion is adjusted to minimize an exponentially weighted cost-to-go (Fleming, 2006):

$$\frac{1}{\theta}\ln\left\langle \exp\left(\theta C_f(y_f)+\theta\int_0^{t_f}\tfrac{1}{2}Q_u u(y(t'),t')^2dt'\right)\right\rangle_{y_0}, \tag{5.21}$$

where θ is a parameter that quantifies the risk sensitivity. If θ is negative then the certainty equivalent is lower than the expected cost-to-go and the controller is said to be risk seeking, and if θ is positive then the certainty equivalent is higher than the expected cost-to-go and the controller is said to be risk averse, and the case $\theta = 0$ is the risk-neutral case (Van den Broek et al., 2010).

In the control task with one target located at zero, we choose an end cost function that is quadratic around the target location (equation 3 with $y^* = 0$). The optimal control is given by

$$u^*(y,t) = -K(t)y$$

with

$$K(t) = \frac{Q_f}{Q_u + (1-\theta\nu Q_u)Q_f(t_f - t)} \tag{5.22}$$

under the condition that

$$0 < Q_u + (1-\theta\nu Q_u)Q_f(t_f - t), \tag{5.23}$$

otherwise no optimal control exists (see previous section). In the control task with two targets located at −0.5 and +0.5, we choose an end cost function that is quadratic around the target locations (equation 5.8). The optimal control is given by

$$u^*(y,t) = -K(t)\big(y-\bar{a}\big) \tag{5.24}$$

where $K(t)$ is as given by equation 5.22,

$$\bar{a} = -a\,\mathrm{sign}(y)\frac{-\psi_-(y,t)+\psi_+(y,t)}{\psi_-(y,t)+\psi_+(y,t)},$$

with $a = 0.5$ and

$$\begin{aligned}\psi_\pm(y,t) = &\sqrt{\tfrac{K(t)Q_u}{Q_f}}\exp\Big(-\tfrac{K(t)(1-\theta\nu Q_u)}{2\nu}(|y|\pm a)^2\Big)\\ &\Big(\tfrac{1}{2}+\tfrac{1}{2}\mathrm{erf}\Big(\sqrt{\tfrac{Q_f}{2\nu(t_f-t)K(t)Q_u}}\,\mu_\mp(y,t)\Big)\Big)\\ &=\tfrac{K(t)Q_u}{Q_f}\Big(\mp|y|+(1-\theta\nu Q_u)Q_f Q_u^{-1}(t_f-t)a\Big),\end{aligned}$$

and under the condition (5.23) for the optimal control to exist (see previous section for a derivation). We obtain the optimal control for the case that $\theta = \frac{1}{\nu Q_u}$ by taking the limit:

$$\lim_{\theta\to 1/\nu Q_u} u^*(y,t) = -\frac{Q_f}{Q_u}\Big(y - a\,\mathrm{erf}\Big(\frac{y}{\sqrt{2\nu(t_f-t)}}\Big)\Big).$$

We consider the risk-sensitive model as an alternative to the extended model to explain the subjects' behavior. For the noiseless condition ($\nu = 0$) the dynamics is completely deterministic and the risk-sensitive model reduces to the standard model: in the absence of noise, the expectation value in equation 5.21 vanishes and the exponentially weighted cost reduces to the total cost in the standard model. Therefore, we do not include the noiseless condition in this section. Note that the extended model does give a different prediction than the standard model for $\nu = 0$. The results show that the extended model yields a significantly better prediction than the standard model (figures 5.3 and 5.5).

For a noise amplitude $\nu > 0$, the risk-sensitive model gives different predictions than the standard model. Figure 5.6 shows the model performance of the risk-sensitive model compared to the standard model for the one-target (left panel) and two-target task (right panel). Values are given as the median over 100 cross-validation runs. The lower and upper error bars represent the 25th and 75th percentile, respectively. Conditions for which the test error of the standard model was significantly different from the test error of the risk-sensitive model (two-sided sign test, $\alpha = 0.05$) are indicated by ** ($p < 0.01$). For all subjects and tasks, the test error of the standard model minus the test error of the risk-sensitive model is significantly larger than zero. Thus, the risk-sensitive model gives a significantly better prediction of the subjects' behavior than the standard model.

Figure 5.7 shows the value of the risk-sensitivity parameter θ for all subjects in the one-target (top panel) and two-target task (bottom panel). Values are given as the median over 100 cross-validation runs. The lower and upper error bars represent the 25th and 75th percentile, respectively. Subsequent data points in triplets correspond to noise amplitudes ν of 0.009, 0.04 and 0.08, respectively. For the majority of the subjects, the risk sensitivity decreases from highly risk-sensitive for $\nu = 0.009$ to approximately risk-neutral for $\nu = 0.08$. From these observations we conclude that the risk-sensitive model can describe the subject behavior at nonzero noise levels, although it would require a risk sensitivity that depends on the noise level.

Infinite horizon models The stochastic optimal control model considered by Braun et al. (2009b) is discrete in time, has an infinite time horizon, a dynamics of the form

$$y_{t+1} = y_t + u_t + \text{“signal-dependent noise”},$$

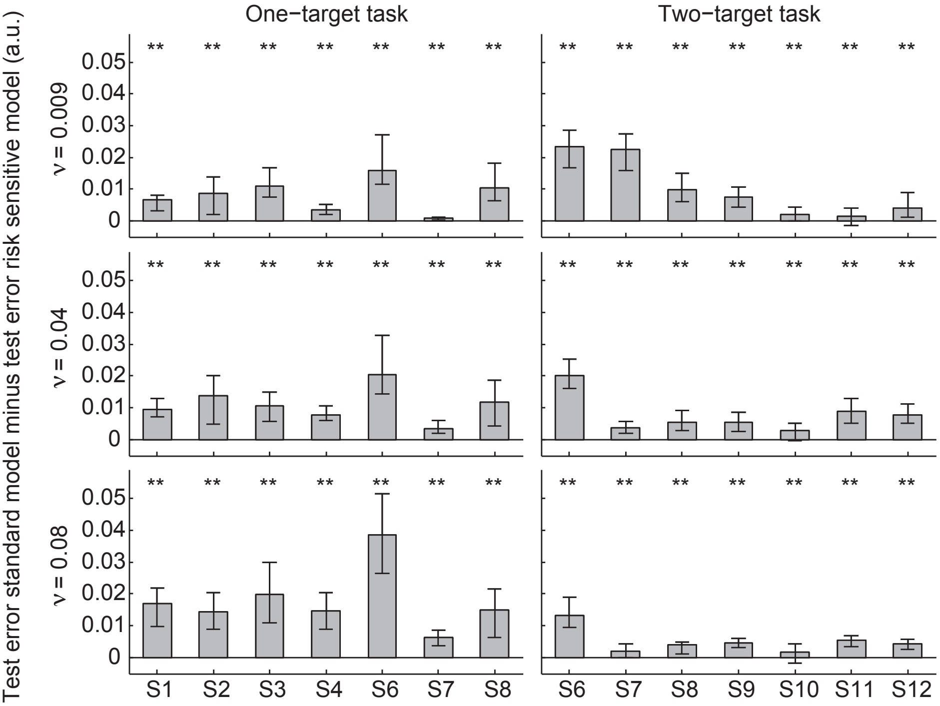

Figure 5.6 Model performance of the risk-sensitive model. Test error of standard model minus test error of risk-sensitive model ('test error difference') for all subjects and noise amplitudes, for the one-target (left panel) and two-target task (right panel). Subject S5 has been discarded. Values are given as the median over 100 cross-validation runs. The lower and upper error bars represent the 25th and 75th percentile, respectively. Conditions for which the test error of the standard model was significantly different from the test error of the risk-sensitive model (two-sided sign test, $\alpha = 0.05$) are indicated by $**$ ($p < 0.01$).

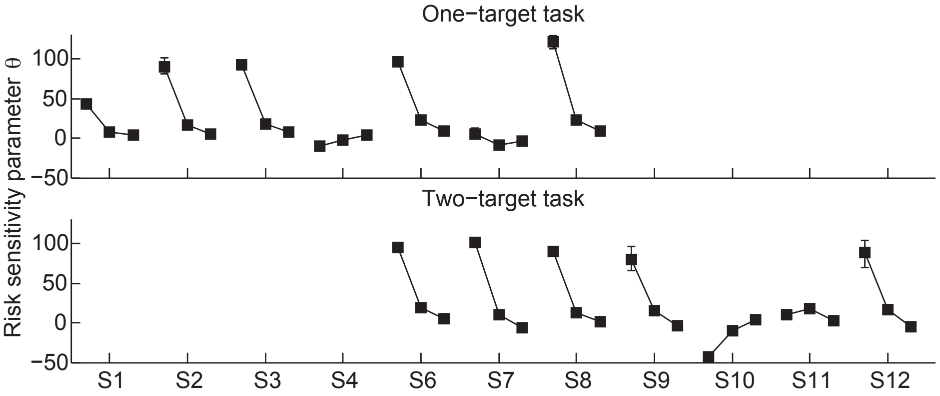

Figure 5.7 Risk sensitivity. Value of the risk-sensitivity parameter θ in the one-target (top panel) and two-target task (bottom panel). Subject S5 has been discarded. Values are given as the median over 100 cross-validation runs. The lower and upper error bars represent the 25th and 75th percentile, respectively. Each subsequent data point corresponds to a noise amplitude ν of 0.009, 0.04 and 0.08, respectively.

and a cost function of the form

$$\text{Cost } J = \tfrac{1}{2}\Big\langle \sum_{t=0}^{\infty} \left(Qy_t^2 + Ru_t^2\right)\Big\rangle, \tag{5.25}$$

where Q and R are constants. The noise is signal-dependent (Harris and Wolpert, 1998), which means that the noise is zero when the state y is zero. This implies that if the state is zero ($y_t = 0$) then it is optimal to perform zero control ($u_t = 0$) at the present time (t) and all future times, because by doing so the state will remain zero ($y_{t+1} = y_t + u_t +$ "noise" $= 0 + 0 + 0$), and the contribution to the cost is zero ($Qy_t^2 + Ru_t^2 = 0$) when the state and the control are zero. An important consequence of using signal-dependent noise is that the cost will not blow up as time proceeds.

If the noise is not signal-dependent, as it is in our experiments, the cost (equation 5.25) will blow up either due to $\sum_{t=0}^{\infty}\langle Qy_t^2\rangle$ blowing up because the state is perturbed by noise that is not sufficiently corrected for by the control, or due to $\sum_{t=0}^{\infty}\langle Ru_t^2\rangle$ blowing up because perturbations of the state due to noise are too much corrected for. Therefore, we consider an alternative infinite horizon model without signal-dependent noise. The dynamics of the control problem are described by

$$dy_t = u(t)dt + d\xi$$

with a cost function

$$C_{total} = \lim_{t_f\to\infty} \frac{1}{t_f}\Big\langle \int_0^{t_f} \tfrac{1}{2}Q_u u(t)^2 dt + \int_0^{t_f} \tfrac{1}{2}Q_y V(y(t))dt \Big\rangle_{y_0}.$$

This is the expected cost in the finite horizon model with end time t_f, but with no end cost and averaged over time and in the limit where the end time goes to infinity. The cost function optimized over the control is the optimal expected cost-to-go J and satisfies the Hamilton-Jacobi-Bellman equation

$$\min_u \left(\tfrac{1}{2}Q_u u^2 + \tfrac{1}{2}Q_y V + u\frac{\partial}{\partial y}J + \tfrac{1}{2}\nu\frac{\partial^2}{\partial y^2}J\right) = c,$$

where c is some constant (Borkar, 2005). It follows that the optimal control u^* satisfies

$$u^* = -Q_u^{-1}\frac{\partial}{\partial y}J \tag{5.26}$$

and that the optimal expected cost-to-go J satisfies the HJB equation

$$-\tfrac{1}{2}Q_u^{-1}\Big(\frac{\partial}{\partial y}J\Big)^2 + \tfrac{1}{2}Q_y V + \tfrac{1}{2}\nu\frac{\partial^2}{\partial y^2}J = c.$$

Since the path cost function V does not depend on time, there is no explicit time dependence in the HJB equation, hence its solution J will also not explicitly depend on time. In the one-target task, we choose a path cost of the form

$$V(y) = \Big(\tanh Dy\Big)^2,$$

where D is a constant. Using the relations

$$\begin{aligned}\frac{\partial}{\partial y}\ln\cosh Dy &= D\tanh Dy\\ \frac{\partial^2}{\partial y^2}\ln\cosh Dy &= D^2\frac{1}{(\cosh Dy)^2}\\ &= D^2\Big(1-(\tanh Dy)^2\Big),\end{aligned}$$

one verifies by substitution that the optimal expected cost-to-go is given by

$$J(y) = G\ln\cosh Dy$$

with

$$G = -\tfrac{1}{2}Q_u\nu D + \tfrac{1}{2}\sqrt{Q_u^2\nu^2D^2 + 4D^{-1}Q_uQ_y}. \tag{5.27}$$

Note that G is positive definite, unless the path cost parameter Q_y equals zero, then G also equals zero and the optimal control is to perform no action. The optimal control follows from equation 5.26 and is given by

$$u^*(y) = -Q_u^{-1}GD\tanh Dy.$$

In the two-target task, we choose a path cost function of the form

$$V(y) = \begin{cases}\Big(\tanh\big(D(y+a)\big)\Big)^2 & \text{if } y \le 0\\ \Big(\tanh\big(D(y-a)\big)\Big)^2 & \text{if } y > 0,\end{cases}$$

where the targets are located at $y = -a$ and $y = a$. One verifies in a similar way as in the one-target case that the optimal expected cost-to-go is given by

$$J(y) = \begin{cases} G \ln \cosh D(y + a) & \text{if } y \leq 0 \\ G \ln \cosh D(y - a) & \text{if } y > 0, \end{cases}$$

with G given by equation 5.27. The optimal control follows from equation 5.26 and is given by

$$u^*(y) = \begin{cases} -Q_u^{-1} G D \tanh D(y + a) & \text{if } y \leq 0 \\ -Q_u^{-1} G D \tanh D(y - a) & \text{if } y > 0. \end{cases}$$

Note that the optimal control shows no symmetry breaking: it is always optimal to steer towards the nearest target. The optimal control in the infinite-horizon model with path cost is similar to the optimal control in the finite horizon model with path cost. When the noise level ν is low, in either model the pace in which to move towards a target is dominated by the path cost, which means for both models the optimal behavior is to arrive at the target before the end time. When the noise level is high, then in either model we find that the control in absolute value is fairly small, which is explained by the fact that the influence of the noise is strong relative to the control.

6

Somatosensory anticipation of curvature in a haptic virtual environment

J.J. Tramper
S. Stephens
M. Flanders

Published in *Proceedings of the IEEE Haptics Symposium*, 2012, pp. 183–186

6.1 Introduction

Little is known about the purely haptic mechanisms that allow humans to explore three-dimensional (3D) surfaces and learn to predict their shapes. Research pertaining to surgical applications is generally focused on the haptic cues that can assist visual control (Bluteau et al., 2008; Reilink et al., 2011) rather than on purely somatosensory guidance mechanisms. Thus few studies have considered haptic exploration without vision, and most of these were restricted to issues of sensitivity or synthesis of features in two dimensions. (Henriques and Soechting, 2003; Soechting et al., 2006). Two-dimensional haptic studies suggest that subjects tend to bias remembered shapes toward being symmetrical and oriented along cardinal axes (Soechting and Flanders, 2011). A similar precedence of symmetry is also consistent with the results of a study of 3D visually-guided hand tracking, where predictive mechanisms became engaged when the trajectory of the visual target entered the second half of a symmetric loop (Mrotek et al., 2006). In the present study, we began to explore strategies for use of predictive mechanisms in a purely haptic shape-tracing task.

6.2 Methods

Subjects were seated comfortably facing a Phantom Premium 3.0 Haptic Device (Sensable Technologies, Inc.) with their right index fingertip strapped into a “finger sled” interface. The subject could move the fingertip freely within a workspace 60.0 cm wide, 60.0 cm high and 30.0 cm deep, unless it encountered a virtual object. The Phantom robot was programmed to create real forces on the subject’s fingertip that were perpendicular to the surfaces of the virtual object and proportional to the distance the fingertip had penetrated the virtual surface. This was accomplished by writing a program in C++ that generated images of geometric shapes (using OpenGL) and enabled subjects to navigate and interact tactilely with those shapes (using the OpenHaptics programming toolkit provided by the device manufacturer).

The virtual shapes used in the experiment consisted of elliptical, tubular objects approximately 40 cm in length along the long axis and 4 cm in diameter (figure 6.1a), and were positioned in the frontal plane about 9 cm above the surface of a (real) table positioned in front of the subject. A pyramid-shaped virtual funnel surface was created that extended down below the lowest point of the shape and functioned to guide the subject into the interior space of the object. The virtual funnel extended below the real surface of the table, effectively keeping the subject’s fingertip restrained to the inner surface of the funnel, making accidental exploration of the outer surface of the object impossible. The subject started each experimental trial with the fingertip on the table, inside the virtual funnel (black dot in figure 6.1a). When the trial started, the subject moved up the funnel and entered the tubular shape, at which time a tone sounded, the funnel disappeared and the hole used for entering the shape was replaced with a solid surface.

The program also recorded position, velocity and force information about the fingertip in 3D at 1-ms intervals. For all virtual surfaces, the stiffness was programmed at 1.0 N/mm. The maximum force that the robot could produce is 22 N transiently and 3 N sustained.

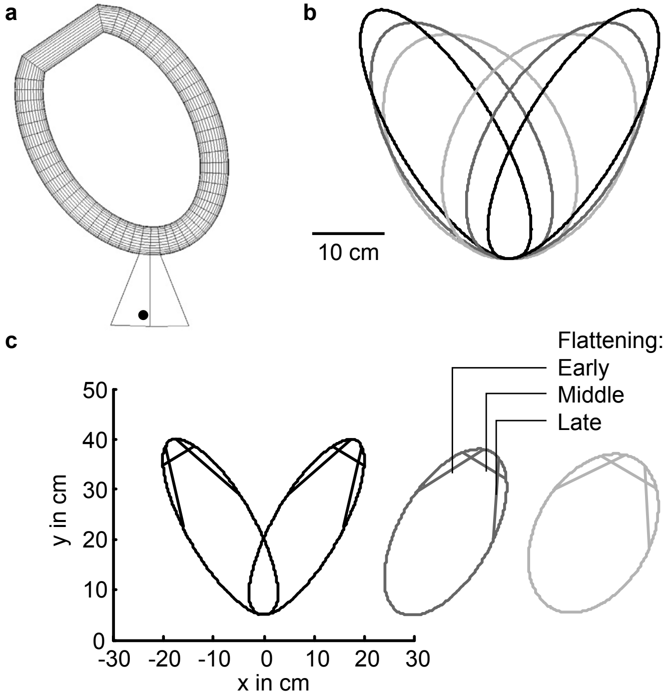

Figure 6.1 Experimental design. **(a)** Tubular ellipse (gray) with funnel (pyramid). The black dot indicates the start position of the subject's fingertip. **(b)** Ellipses with ratios 3:1, 2:1 and 3:2 of semi-major axis to semi-minor axis (black, dark gray and light gray, respectively) were rotated 30 or –30 deg in the frontal plane. **(c)** In 18 of the 24 ellipses, a curved section of the ellipse was replaced with a straight tubular segment. Subjects were instructed to move clockwise through the shapes, such that the flattening occurred at an early, middle or late portion of the shape.

The maximum force typically used by the subjects on the inner surfaces of the elliptical objects was about 1–2 N.

Three different ratios (3:1, 2:1 and 3:2) of semi-major axis to the semi-minor axis were used in building the ellipses (black, dark gray and light gray ellipses in figure 6.1b, respectively). These ellipses were rotated 30 or −30 deg in the frontal plane (to avoid positioning the shapes along the cardinal axes) and so produced a total of six different basic elliptical paths.

In 18 of the 24 ellipses used in the experiment, a curved section of the ellipse was replaced with a straight tubular segment. This was called "flattening" and was calculated to occur at an early, middle or late portion of the shape (figure 6.1c). This nomenclature is based on the fact that the subjects were instructed to move clockwise through the shapes, and thus the early flattening would be encountered by the subject sooner than the middle or late flattening. (The shape shown in figure 6.1a depicts middle flattening.) In geometric terms, each flattened section was created by removing 20% of the total coordinate vertices of the shape.

The subjects were normal, healthy adults (one male and two female) and gave informed consent before taking part in the experiment. Each subject participated in two experimental conditions consisting of 26 trials each. The subjects used trials 1 and 2 for practice. The 24 remaining shapes represented the six basic elliptical paths modified with early, middle, late or no flattening, thus each shape was unique. The sequence of shapes was random but was the same for each experiment and each subject. Trials where subjects moved counterclockwise or machine malfunction was experienced were repeated at the end of the experiment. Subjects did not receive visual information about the shapes presented.

The subject began each trial with the right fingertip at a start-position mark on the table and was allowed to rest their elbow on the armrest of the chair. The subject then raised the fingertip into the shape and moved in a clockwise manner around the shape five times. After circling the object four times, the subject was informed that only one "lap" was remaining. After completing the last lap, the virtual object disappeared, the subject returned the fingertip to the start position and reported whether or not they perceived a flattened region in the shape just explored. Subjects were instructed to remain in constant motion and to keep their eyes closed during the trial.

The "no-touch condition" differed from the "touch condition" in the instructions given to the subjects. During the no-touch condition, subjects were instructed to use the initial laps of each trial to learn the shape and then demonstrate that knowledge by touching the walls of the shape as little as possible. For the touch condition, however, subjects were instructed to move "quickly and smoothly, with as little force as possible against the sides" and to "remain in constant contact with surface of the object". Analysis focused on laps 1–4 due to occasional early termination.

6.3 Results

The subjects' performance improved during exploration of the ellipse. In the no-touch condition, where subjects were instructed to stay off the wall, the amount of time that subjects did not touch the inner wall of the ellipse increased for increasing lap number (figure 6.2, black squares). For all subjects, the percentage of time they stayed off the wall within a lap was significantly larger (Mann-Whitney U test; $p < 0.01$) for the fourth lap compared to the first lap. However, subjects never touched the wall for less than 20% of the time, and thus they were not completely successful. In the touch condition, where subjects were instructed to trace the ellipse by gently touching the wall, the amount of time that subjects stayed off the wall decreased toward zero after the first lap (figure 6.2, gray squares). The decrease between lap 1 and lap 4 was significant ($p < 0.01$) for all subjects. The values became very close to zero for laps 2–4.

Subjects became faster in exploring the shape in the touch condition. The time subjects spent tracing the fourth lap was significantly shorter ($p < 0.01$) than the first lap (figure 6.3, gray squares), indicating that their average speed increased during tracing of the wall. In the no-touch condition, the duration of lap 4 was significantly shorter than lap 1 for subject 1 ($p = 0.04$) and subject 2 ($p < 0.01$), but not for subject 3 ($p = 0.52$).

We analyzed the responses to the question "Did you detect flattening?" which was asked at the end of each trial. Using the subject reports from all shapes that did contain flattening, figure 6.4 shows combined data for the three subjects and the two tilts of each ellipse, with each bar representing the average of six reports. A score of 100% would mean that in all six cases flattening was detected; a score of 0% would mean that the

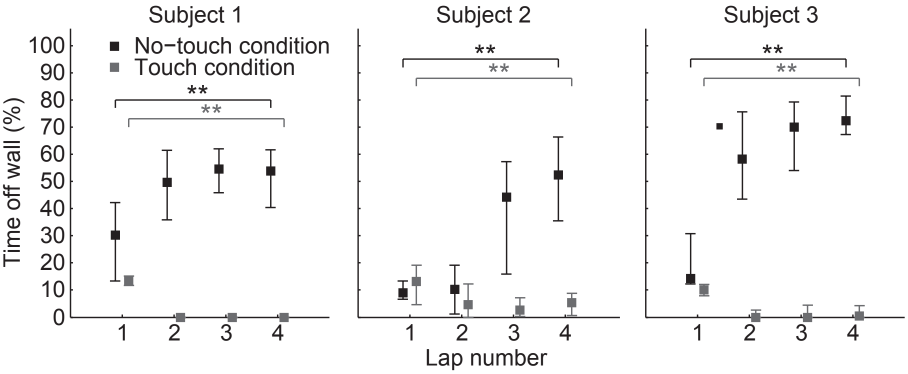

Figure 6.2 Time off wall relative to lap duration (percentage) for laps 1–4, for the no-touch (black) and touch condition (gray). Squares indicate median values over all shapes. Lower and upper error bar represent the 25th and 75th percentile, respectively. Significant differences (Mann-Whitney *U* test) between lap 1 and 4 are marked with $**$ ($p < 0.01$).

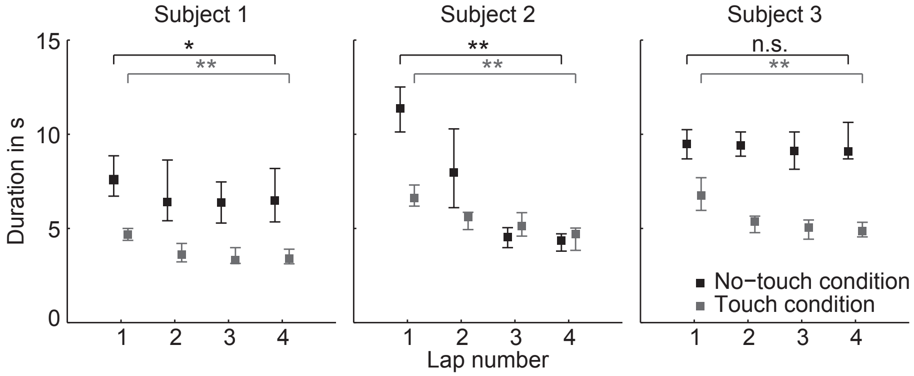

Figure 6.3 Lap duration in seconds for laps 1–4, for the no-touch (black) and touch condition (gray). Squares indicate median values over all shapes. Lower and upper error bar represent the 25th and 75thpercentile, respectively. Significant differences (Mann-Whitney *U* test) between lap 1 and 4 are marked with $*$ ($p < 0.05$) or $**$ ($p < 0.01$); differences which are not significant ($p > 0.05$) are marked with 'n.s.'.

flattening was never detected. Comparing the two experiments (figure 6.4, left and right), subject reports of flattening were more often correct in the touch condition, when they were allowed to be in constant contact with the walls ($F(1, 90) = 6.6, p < 0.05$). Reports for the most rounded shape (light gray bars) were better than the reports for the longest shape (black bars), with intermediate performance for medium shape (dark gray bars). ANOVA post hoc testing showed that the flattening in the rounded shape was detected significantly better ($p < 0.05$) than for the other two shapes, which were not different from one another (Scheffé test, $p = 0.36$). Flattening was more likely to be detected when it occurred in the middle portion (center bars, horizontal hatching), compared to early and late ($p < 0.01$), but early and late flattenings were not different from one another (Scheffé test, $p = 0.85$). Thus a flattened section was most often detected in the middle of the most rounded ellipse and most often undetected on the sides of the longest ellipse.

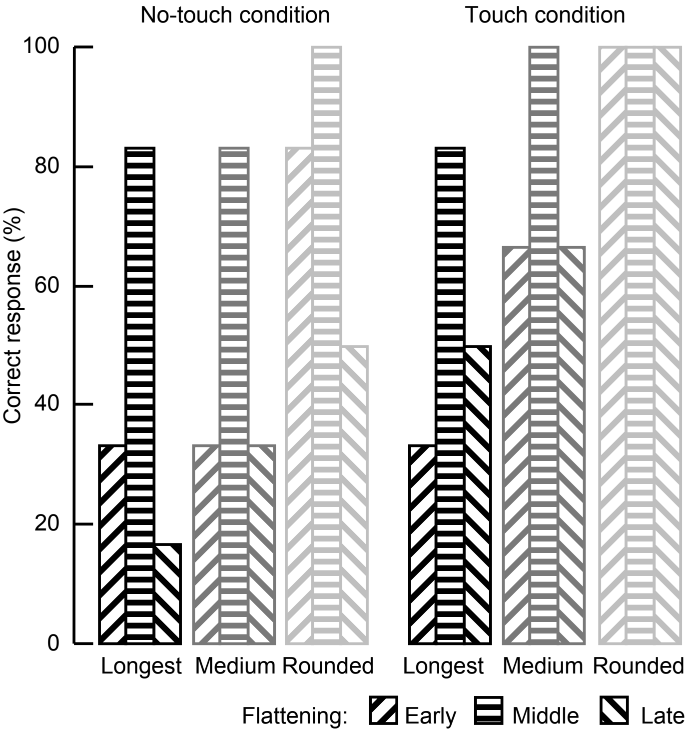

Figure 6.4 Subject reports of flattening for the no touch (left) and touch condition (right), given in percentage of trials. Black, dark gray and light gray bars indicate the average over subjects for the longest (ratio 3:1), medium (ratio 2:1) and rounded (ratio 3:2) ellipses. Early, middle and late flattening are represented by upward diagonal, horizontal and downward diagonal hatching, respectively.

To answer the question about whether subjects anticipate the upcoming flattened section of the shape, or instead merely react after encountering the start of a flattened section, for the touch condition, we analyzed contact force and finger speed around the onset of flattening for the subsequent laps. Figure 6.5 shows force and speed for subject 3 exploring an ellipse with ratio 3:2 (rounded), tilt = −30 deg and middle flattening. All subjects reported flattening for this shape (see figure 6.4). In the first lap (black), force increased and speed decreased immediately after the onset of flattening. This was caused by the subject hitting the "corner" between the smooth section of the ellipse and the flattened section. In the next laps, this peak in force immediately after the onset of flattening was less pronounced. The speed profile before the onset differed substantially between the first lap (black) and the next laps. In the first lap, the speed slightly increased between −1.5 and 0 s. However, in the same time interval the speed decreased for laps 2–4. As a result, the finger speed at the onset of flattening was lower for laps 2–4 compared to lap 1, but higher 1.5 s before the onset. Thus, after exploring the shape for the first time, this subject slowed down before entering the flattened section the next times.

We quantified the instant at which subjects slowed down by determining the cross-over point of the speed trace of lap 4 with the speed trace of lap 1 (arrow in figure 6.5), and did the same for lap 3 with lap 1. The analysis required that the speed of lap 1

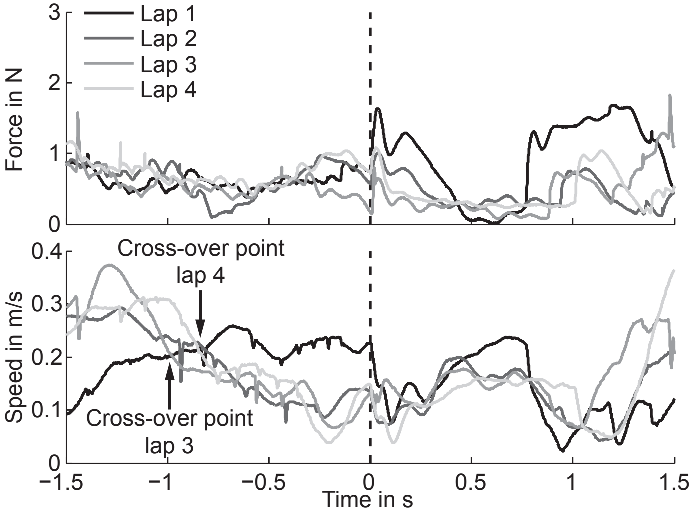

Figure 6.5 Force (upper panel) and speed (lower panel) for subject 3 exploring an ellipse with ratio 3:2, tilt –30 deg and middle flattening. Laps 1–4 are colored from black to light gray, respectively, for the touch condition. For each lap, the force and speed time traces are aligned to the onset of flattening, which is time zero (dashed line). Arrows indicate cross-over points between the speed trace of that particular lap with the speed trace of lap 1.

remained larger than the speed of laps 3 or 4 between the cross-over point and the onset of flattening. This procedure was repeated for all subjects and for all shapes with a 3:2 ratio and middle flattening. For subjects 1–3, we found a cross-over point in 100%, 100% and 75% of the cases, respectively. The median time instant at which subjects slowed down before the onset of flattening was 343 ms (range 82–613 ms), 270 ms (36–1258 ms) and 245 ms (34–1045 ms) for subjects 1–3, respectively.

6.4 Discussion

In this study, human subjects explored ellipses by moving their fingertips through a virtual tube. In the no-touch condition, we asked subjects to touch the walls of the tube as little as possible, whereas in the touch condition, subjects were asked to keep contact with the wall while moving smoothly and quickly around the shape. We compared both conditions in terms of performance (force, lap duration and verbal reports of flattening) and we quantified anticipation of flattened sections in the shape.

In the no-touch condition, the time subjects stayed off the wall increased for each subsequent lap (figure 6.4, black squares). However, subjects never managed to stay off the wall for the whole duration of a lap. This suggests that subjects improved their performance but still had difficulties with anticipating the flattening in the fourth lap. We expected that subjects would move faster if they became better at anticipating the corners. Subject 2 clearly increased his movement speed (figure 6.3, black squares), but the other subjects exhibited either a slight decrease in lap duration (subject 1) or no decrease at all (subject 3). Therefore, anticipating the corners was rather difficult for the no-touch condition. Most likely, the reason is that since subjects were instructed to stay off the wall, they were unable to accumulate haptic information for predicting the shape. In the touch condition, subjects performed well and kept in contact with the wall (figure 6.4, gray squares), which allowed them to accumulate haptic evidence for the shape. Therefore, we expected subjects to become faster over laps in the touch condition, which is what we found (figure 6.3, gray squares).

Another aspect of subjects' performance is whether subjects correctly reported flattening. Scores were higher for the touch condition than for the no-touch condition. We believe that when subjects were allowed to touch the walls, they could actively sense the "corner" between the elliptical section and the flattened section, resulting in higher scores for the touch condition. In the no-touch condition, if subjects succeeded in trying to stay off the wall, they would have tactile information only when they unintentionally hit it.

Middle flattening was more often reported correctly than early and late flattening. Most likely, this is caused by the relatively sharp corners between the elliptical section and flattened section in the middle, compared to the moderate corners found in shapes with early and late flattening (figure 6.1c). Likewise, the flattening was seldom reported when it was early or late in the longest ellipse. This may be due to the relatively large radius of curvature (about 0.6 m) at the point where the side walls of the long ellipse transitioned into the flat region. A previous 2D study, using a psychophysical technique, showed that subjects perceived a radius of curvature of about 2 m as being straight (Henriques and Soechting, 2003). Thus the transition between the gently curved sides of the long ellipse and the early and late flat regions may have been indistinct.

In designing the experiment we decided we should not orient the elliptical shapes along the cardinal directions (Soechting and Flanders, 2011). Thus the shapes were relatively difficult for subjects to recognize and remember. Performance was better when subjects were allowed to stay in contact with the wall and they did show some evidence that they anticipated approaching an upcoming flattened region (figure 6.5). However, this anticipation was not particularly consistent or precise. In our analysis of the shape with the most obvious flattening (the rounded ellipse with the middle flattening), the three subjects did show anticipation, but the timing varied widely even within an individual subject, ranging from about 100–1000 ms prior to the event. This lack of precision in anticipation is reminiscent of the results of recent studies of smooth pursuit eye movements, where shape cues were of little use unless they could be coupled to timing mechanisms (Badler et al., 2010; Winges and Soechting, 2011). Potential mechanisms for extrapolation of somatosensory targets, such as gradual or familiar surface shape transitions, have yet to be explored.

7

Predictive mechanisms in the control of contour following

J.J. Tramper
M. Flanders

Accepted for publication in *Experimental Brain Research*

7.1 Introduction

The sensorimotor system uses a combination of feedback and predictive mechanisms to control ongoing movements. For example, smooth pursuit eye movements are usually driven by visual feedback of actual retinal target motion (Krauzlis and Lisberger, 1994). However, the system can also generate a prediction of the anticipated retinal target motion, for instance when the target is temporarily occluded (Becker and Fuchs, 1985; Mrotek and Soechting, 2007) or when the direction of target motion is cued (Barnes, 2008). Activity in higher cortical areas such as the frontal eye fields may form predictions based on prior patterns of target motion, which then serve to modulate the gain of smooth pursuit in anticipated directions (Yang et al., 2012). Furthermore, in some situations the retinal target motion may be replaced with cognitively-generated target motion, thus producing a feedback system driven by a cognitive goal trajectory (Tramper et al., 2013).

Like visual guidance of eye movement, haptic guidance of arm movement is a situation where the movement itself alters the sensory input. Thus contour following (Lederman and Klatzky, 1987) and haptic tracking (Rosenbaum et al., 2006) are essentially cases of sensory guidance that are accomplished with a somatosensory feedback loop. This was quantified by Weiss and Flanders (2011) using a task where subjects ran a fingertip across spherical virtual surfaces. Subjects reacted to an unexpected change in surface curvature with a compensatory adjustment in contact force at a latency of about 50 ms, which was explained by proposing a spinal control mechanism comparing the actual somatosensory feedback with an expectation provided by efference copy. Other results of this study also suggested longer-latency feedback loops involving the somatosensory cortex, as well as cortical learning and prediction within each trial. The present study aimed to further quantify the predictive mechanisms.

In contrast to visual feedback, somatosensory feedback is complicated by the multiplicity of signal sources, such as tactile and proprioceptive inputs, and their substantial processing delays and inaccuracies (Biggs et al., 1999; Scott and Loeb, 1994). Thus the haptic guidance system should combine feedback and predictive control mechanisms in an efficient fashion. Precisely moving the fingertip in 3D space is especially challenging. When Klein Breteler et al. (2003) asked subjects to draw a repeated series of 3D triangles without tactile feedback, the fingertip position drifted and changes in arm posture accumulated across consecutive cycles. Similarly, in a preliminary study (Tramper et al., 2012), we instructed blindfolded subjects to transition from feedback to feedforward performance over the course of several consecutive laps around the same virtual shape. Subjects were instructed to touch the virtual guide as little as possible and eventually to stay just slightly off the surface of the shape. We hypothesized that, as in robotics, the subject would execute the first lap under feedback control and learn the outline of the shape for feedforward execution of subsequent laps. Perhaps due to imprecise movement execution or poor learning and memory, subjects were unable to successfully use this strategy. Thus the current study was designed to test the degree to which subjects could successfully use the alternative strategy of combining ongoing tactile feedback control (i.e., with the finger constantly in contact with the surface) with cortical anticipation of upcoming changes in surface curvature. The design allowed us to investigate two potential types of cortical

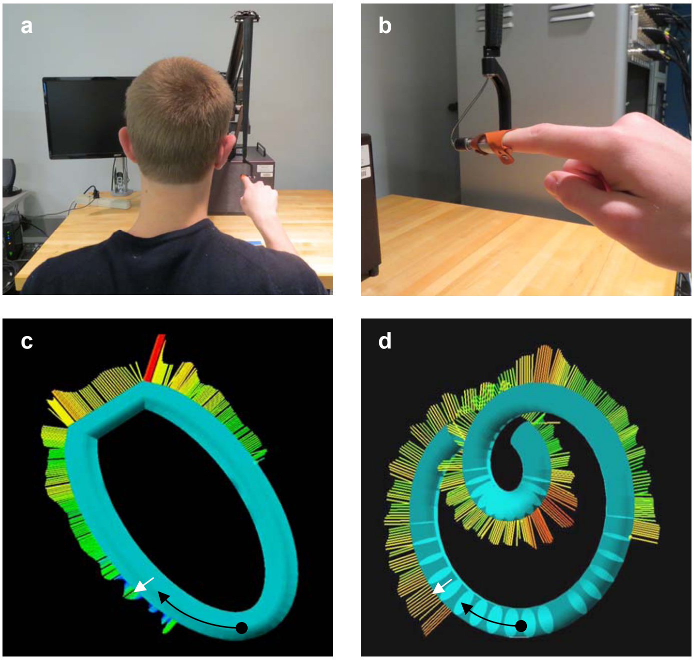

Figure 7.1 Experimental setup. The finger sled attachment (red) is viewed from the back of the subject (panel a) and from the subject's left side (panel b). Subjects had eyes closed during each trial and their computer monitor was always switched off. Fingertip starting position within virtual tubes (black dots), movement direction (black arrows), and contact force direction (white arrows) are indicated for example shapes from experiment 1 (panel c) and experiment 2 (panel d). These screenshots (seen only by the experimenter) also indicate the magnitude of the perpendicular contact forces (by color and length).

prediction: learned anticipation (experiment 1) and anticipation due to extrapolation of surface contours (experiment 2).

7.2 Methods

Setup Subjects were seated in a chair in front of a Phantom Premium 3.0 Haptic Device with finger sled (figure 7.1a, Sensable Technologies, Inc.), and the right index fingertip was attached to the tip of the lightweight robot arm (figure 7.1b). Within a workspace of 60 cm wide, 60 cm high and 30 cm deep, subjects could move their fingertip without restriction unless it encountered a virtual surface, and then the fingertip would slide along the surface. The robot could produce forces with a maximum of 22 N transiently and 3 N sustained when the fingertip attempted to penetrate the surface, and we programmed the stiffness as 1.0 N/mm. Due to the mechanics of the finger sled attachment, when the fingertip pressed into the surface, the subjects experienced compression of the enclosed finger region and resistive force in the arm corresponding to the direction of the applied force (i.e., normal to the virtual surface). In our setup, subjects generally explored 3D shapes with the index

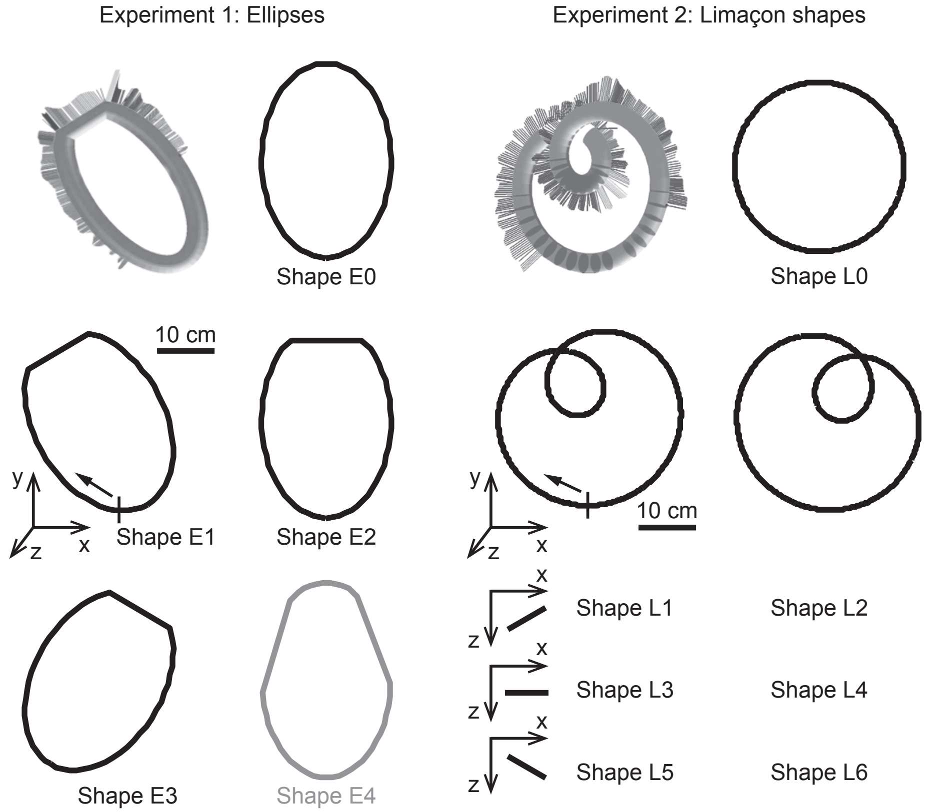

Figure 7.2 Experimental design. Left column: tubular ellipses (experiment 1) positioned in the frontal plane. Shapes E1–E3 were rotated 30, 0, or –30 deg around the *z*-axis and a portion located at the highest point of the major axis was replaced with a straight tubular segment. Shape E4 (gray) was not used in the analyses. Shape E0 was the control condition. Subjects started their movement at the bottom of the shape (indicated by the vertical line in E1) and were instructed to move in a clockwise direction. Right column: tubular Limaçon shapes (experiment 2). Shapes were rotated 25 deg counterclockwise (L1, L3, L5) or 25 deg clockwise (L2, L4, L6) around the *z*-axis. These shapes were then rotated –30 deg (L1 and L2), 0 deg (L3 and L4) or 30 deg (L5 and L6) around the *y*-axis. Shape L0, the control condition, was a circle oriented in the frontal plane.

finger nearly horizontal (figure 7.1b, also see Weiss and Flanders, 2011). Finger position, velocity, and contact force were recorded at 1-ms intervals.

Virtual shapes The virtual objects consisted of tubular ellipses (figure 7.1c, experiment 1) and Limaçon shapes (figure 7.1d, experiment 2) approximately 40 cm in length along the long axis and 4 cm in tubular diameter (figure 7.2). When a trial started, the subject moved his or her index fingertip from the table upward into a virtual funnel guiding the finger to the entrance of the tube at the bottom of the shape (indicated by the small vertical lines in figure 7.2). As soon as the fingertip entered the tube, a tone sounded, the funnel disappeared, and the tube's entrance became sealed until the end of the trial. In this way, subjects entered the tube and then followed the inner surface, pressing outward.

The ellipses (figure 7.2, left) were positioned in the frontal plane about 9 cm above the surface of a table, with the x- and y-axes representing the cardinal axes, and the z-axis the depth direction from the point of view of the subject. We used six different ellipses, all with a 3:2-ratio of major axis (33.75 cm) to minor axis (22.5 cm). Shapes E1–E3 (left column) were rotated 30, 0, or −30 deg around the z-axis. A portion of the ellipse, located at the highest point of the major axis, was replaced with a straight tubular segment of 12.26 cm. In shape E4, two curved portions of the ellipse were replaced with straight segments. This shape was included to make the sequence of shapes more unpredictable (see next section), but was not used in the analyses. Shape E0 was an ellipse with 0 deg tilt and no flattening, and acted as a control condition.

The Limaçon shapes (figure 7.2, right) were placed in vertical planes about 9 cm above the table's surface. The template shape with the small loop located at the top and oriented in the frontal plane is defined by

$$\begin{aligned} x(\phi) &= -a(\sin\phi + k\sin 2\phi) \\ y(\phi) &= -a(\cos\phi + k\cos 2\phi), \end{aligned} \qquad (7.1)$$

where x and y represent coordinates along the cardinal axes, $a = 8.0$ cm, $k = 1.25$, and angular position $\phi = 0\ldots360$ deg. The robot was programmed with direction sensitivity so that the virtual surface continued without crossing as the fingertip entered and departed the small loop. This allowed subjects to follow continuously along a single curved surface. On different trials, the template shape was rotated 25 deg counterclockwise (L1, L3, L5) or 25 deg clockwise (L2, L4, L6) around the z-axis, followed by a rotation of −30 deg (L1 and L2), 0 deg (L3 and L4) or 30 deg (L5 and L6) around the y-axis, to create a total of six Limaçon shapes in various vertical planes. As a control condition, we added a circle oriented in the frontal plane (L0). The radius of the circle was 10.4 cm, such that the curvature was equal to the average curvature of the Limaçon shapes.

Subjects and experiment Six human subjects (three males) aged between 22 and 40 years participated in both experiments. All subjects were naive and right-handed, and none of them had any known motor disorder. The subjects gave written informed consent before taking part in the experiments and the protocol was approved by the University of Minnesota IRB. In each experiment, subjects were presented a sequence of shapes starting with three training trials (including a range of tilts and possible shapes), followed by 30 (experiment 1) or 35 (experiment 2) trials using the shapes in random order, and ending with five repetitions of shape E1 (experiment 1) or shape L1 (experiment 2). In experiment 1, five repeats of elliptical shapes E0–E3 and ten repeats of shape E4 were used to create the random sequence of 30 trials. In experiment 2, five repeats of Limaçon shapes L0–L6 were used to create the random sequence of 35 trials.

Subjects started each trial with the right fingertip in contact with a start position bump on the table, then raised the fingertip into the shape, and moved in clockwise direction, making five laps in total. They were instructed to smoothly follow the wall by lightly pressing outward (radial direction) and remaining in constant contact while keeping their eyes closed. We emphasized that the main instruction was to keep moving while pressing as lightly as possible. The screenshots in figures 7.1c and d show examples of a subject tracing the shapes by pressing outward (arrows), as indicated by the color/length-coded contact force vectors perpendicular to the surface. After the subject completed the last lap, the force field disappeared and the subject returned the fingertip to the start position (and the elbow to the arm rest). Trials where subjects moved transiently backwards or where the robot malfunctioned (about 10% of the trials) were repeated at the end of the random block.

Data analysis Data were analyzed using Matlab (The MathWorks, Inc.). To skip initial transients after subjects entered the tubes via the guiding funnel, the first 10 cm of each movement was discarded. Then, each trial was subdivided into five consecutive laps, each lap starting 10 cm after the starting position at the bottom of the shape. The tangential velocity, or speed, was calculated as $v = \sqrt{v_x^2 + v_y^2 + v_z^2}$, with v_x, v_y and v_z the velocity components along the coordinate axis. In experiment 2, speed and force were smoothed with a Savitzky-Golay filter of degree 2 and a span of 199 ms. In experiment 1, we did not smooth the data because we were interested in the abrupt change of speed and force at the onset of a flattened section.

For averaging across repetitions in experiment 2, the speed and force time traces of each lap were mapped to the corresponding spatial locations along the shape (see figures 7.6 and 7.7). Therefore, we subdivided the angular position ϕ (see equation 7.1) into 1000 equally-spaced bins. Next, for each finger position $(x(t), y(t), z(t))$, finger speed and force were mapped onto the center of the nearest bin. In general, each lap contained about several thousands of time points, corresponding to a lap duration of several seconds. This resulted in multiple values per bin after the mapping procedure. Therefore, we averaged across these data points to obtain a single value for speed and force per position bin.

For natural hand movements, the tangential velocity of the fingertip is often related to the curvature of the fingertip's trajectory. This relationship is called the two-thirds power law (Lacquaniti et al., 1983; Viviani and Terzuolo, 1982) and is given by

$$v = c\kappa^{-\frac{1}{3}} \tag{7.2}$$

where v is the tangential velocity (or speed), κ is the curvature and c is a constant. (The curvature κ is related to the radius of curvature R as $\kappa = 1/R$.) In experiment 2, for each of the five laps, this equation was fitted to the observed finger speed as a function of angular position along the tube (and thus tube curvature), yielding five values for c per trial.

7.3 Results

Overall performance – both experiments While tracing one of the virtual shapes, subjects may become more familiarized with the shape over time. Therefore, we used the average tracing speed per lap as a performance index, thinking that the average speed might increase across consecutive laps. Figure 7.3 (top panel) shows the average tracing speed per lap, pooled across all trials. An average speed of 30 cm/s would correspond to about 3.4 s per lap for ellipses, and 5.3 s per lap for Limaçon shapes. The majority of subjects slightly increased their average speed across laps while exploring the flattened

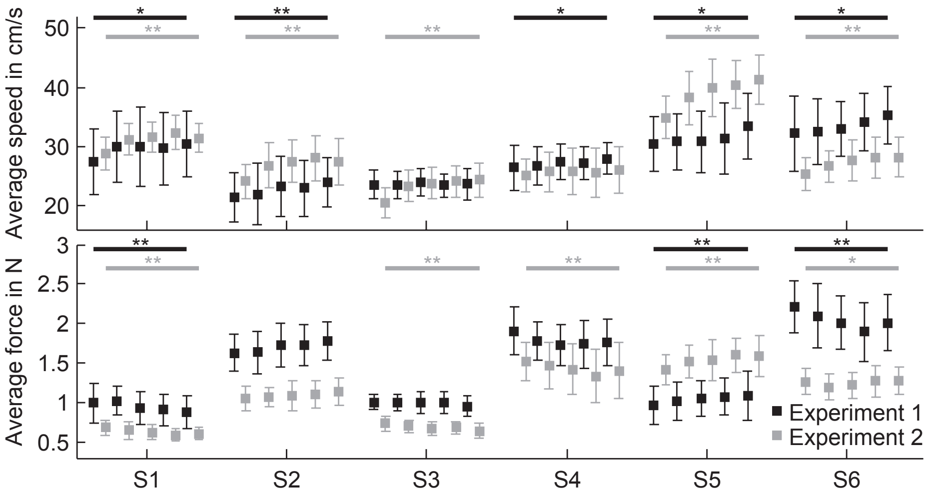

Figure 7.3 Average tracing speed (top row) and contact force (bottom row) per lap for experiment 1 (black symbols) and experiment 2 (gray symbols). Data are pooled across all repetitions of shapes E1–E3 (experiment 1; $n = 15$) or shapes L1–L6 (experiment 2; $n = 30$). Error bars represent the standard deviation. Significant difference between laps (repeated measures ANOVA) were marked with $*$ ($p < 0.05$) or $**$ ($p < 0.01$).

ellipses (E1–E3) in experiment 1 (top panel, black squares; repeated measures ANOVA, $p < 0.05$ for S1, S4–S6, $p < 0.01$ for S2; p = 0.69 for S3). This increase was also found for the Limaçon shapes (L1–L6) in experiment 2 (top panel, gray squares; repeated measures ANOVA, $p < 0.01$ for S1–S3, S5, S6; $p = 0.24$ for S4).

In both experiments, subjects were asked to trace the virtual shape in a smooth fashion by touching the wall as lightly as possible. Therefore, we used the average contact force per lap as a second measure of overall performance and tested whether this average force changed across laps (figure 7.3, bottom panel). In experiment 1 (ellipses), three subjects did not change the average force (bottom panel, black squares; repeated measures ANOVA, $p > 0.05$ for S2–S4) while tracing the shapes (black squares in figure 7.3, bottom panel; ANOVA, $p > 0.20$). The other subjects either decreased ($p < 0.01$ for S1, S6) or increased ($p < 0.01$ for S5) the amount of contact force across laps. In experiment 2 (Limaçon shapes) S1, S3 and S4 decreased their contact force (bottom panel, gray squares; repeated measures ANOVA, $p < 0.01$), whereas S5 increased the amount of force ($p < 0.01$). S2 did not adjust the force ($p = 0.06$) and S6 did so ($p < 0.05$), but slightly and without a clear decrease or increase.

To summarize, subjects improved their performance during haptic tracing of a shape by becoming slightly faster across laps. Although speed was not instructed, this is a natural tendency during an experiment with many trials. The average amount of contact force changed very little, suggesting that this aspect of the behavior was more or less maintained across laps.

Anticipation of an abrupt event – experiment 1 The next analyses focused on experiment 1, where subjects explored frontal-plane ellipses with flattened sections. This exper-

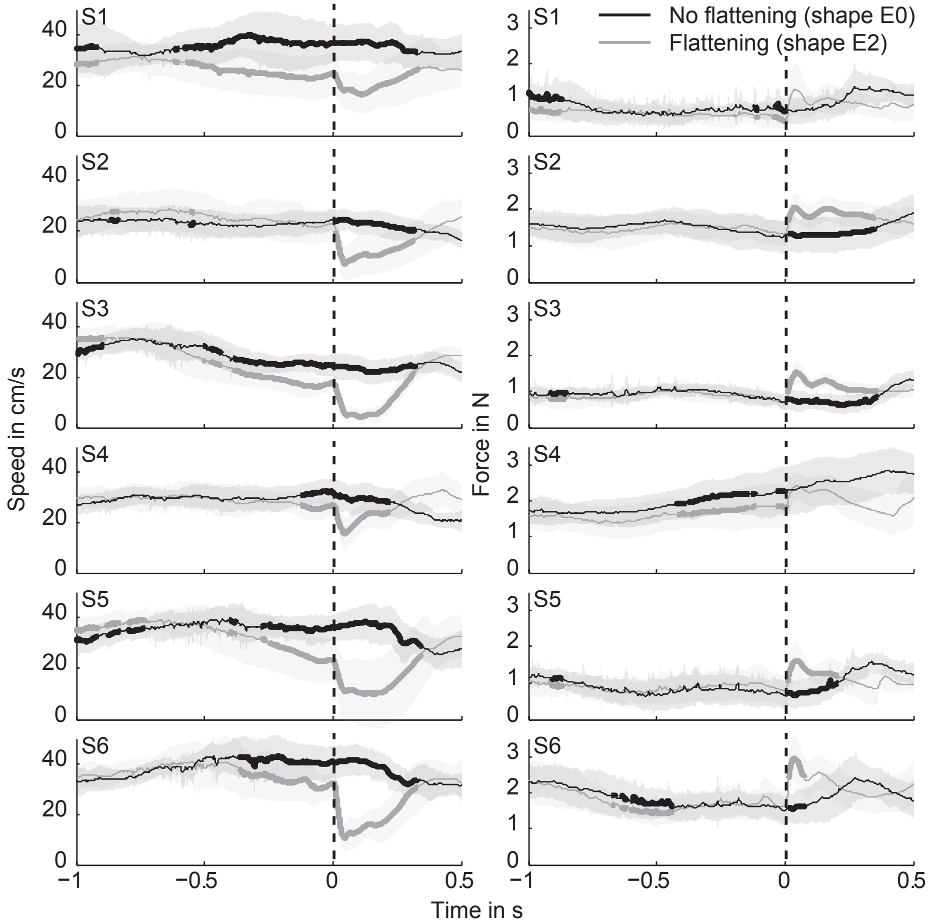

Figure 7.4 Finger speed (left column) and contact force (right column) for subjects exploring the 0-deg tilted ellipse. Black traces show the mean for data of the non-flattened shape (shape E0), pooled across laps 2–5 and repetitions (4 laps × 5 repetitions = 20 time traces). Black traces are aligned to the point that corresponds to the onset of flattening in shape E2 (flattened shape), as indicated by the dashed lines at $t = 0$. Gray traces show the mean for data of the flattened shape (shape E2) pooled across laps 2–5 and repetitions (20 time traces); they are aligned to the onset of flattening. Shaded area represents the standard deviation. Thick lines indicate significant differences (Mann-Whitney *U* test, $p < 0.05$) between the non-flattened shape (black lines) and the flattened shape (gray lines).

iment was designed to investigate whether subjects could learn to anticipate an abrupt, haptic event (the first corner). We analyzed finger speed and contact force around the time of the corner (time zero). Speed always decreased and force increased upon impact with the corner. We hypothesized that subjects would use knowledge of the shape acquired in the first lap to anticipate the corner in the subsequent laps with a preparatory adjustment in speed and/or contact force. This would be in line with the instruction to press as lightly as possible as well as the natural tendency to avoid a hard hit of the flattened surface.

Table 7.1 The anticipatory slowdown prior to the first corner of a flattened section, in time and space. Values represent the onset of a significant difference (Mann-Whitney *U* test) between finger speed in flattened (E2) and non-flattened (E0) shapes.

Subject	Time relative to corner	Distance relative to corner
S1	−578 ms	−168 mm
S2	not significant	not significant
S3	−390 ms	−54 mm
S4	−128 ms	−31 mm
S5	−250 ms	−79 mm
S6	−365 ms	−29 mm

For each subject, we compared lap 1 of shapes E1–E3 to the average values for laps 2–5. At time zero, speed in laps 2–5 was never significantly higher than in lap 1 (Mann-Whitney *U* test, $p < 0.05$), despite the fact that average lap speed was higher for most subjects (figure 7.3). This suggests some degree of anticipation in all subjects. Next, we looked for anticipatory adjustments in contact force. In the laps 2–5, subjects generally did not reduce their force just prior to impact. The only exception was S4 who started to significantly reduce contact force 131 ms before the corner (Mann-Whitney *U* test, $p < 0.05$, data not shown).

If subjects successfully anticipated the corner, by slowing, reducing contact force, or reducing stiffness, we would expect that the force of impact would decrease over laps. Subjects S1, S3, S4 and S6 did indeed show a significant reduction of contact force in laps 2–5 at or within 100 ms after the onset of flattening (Mann-Whitney *U* test, $p < 0.05$, data not shown). Thus most subjects achieved a significant degree of anticipation of the mechanical consequence of impact.

To quantify the timing of the anticipation, we excluded all data from lap 1 and compared speed and contact force between a flattened (E2) and a non-flattened (E0) version of the same shape. In figure 7.4, the gray traces represent data of the flattened ellipse with 0 deg tilt (shape E2, see figure 7.2), averaged across laps 2–5 and all repetitions (4 laps × 5 repetitions = 20 time traces). The black traces show data of the ellipse without a flattened section (control shape E0), averaged across laps 2–5 and all repetitions (20 time traces), aligned to the point that corresponded to corner of shape E2. Standard deviations are shown as light gray shaded regions around the black traces, and time intervals with significant differences between the two conditions are shown as thicker traces (Mann-Whitney *U* test, $p < 0.05$).

For the speed traces (left column of figure 7.4), all subjects except S2 significantly reduced their speed before the onset of flattening. However, the time at which subjects started to decelerate their finger ranged from –578 ms to –128 ms (table 7.1). If subjects were attempting to remember the spatial location of the corner, this slowdown point might be more consistent in space, rather than time. We therefore computed the distance from the slowdown point to the corner for each subject (table 7.1). This was also rather large and quite variable across subjects, ranging from about –17 cm to –3 cm.

The force analysis (right column of figure 7.4) revealed that most subjects did not adjust the amount of contact force prior to hitting the corner. S4 was the only subject with a sustained decrease in contact force prior to the corner, but contact force for the flattened shape was lower throughout this 1-s interval. As expected, immediately after the onset

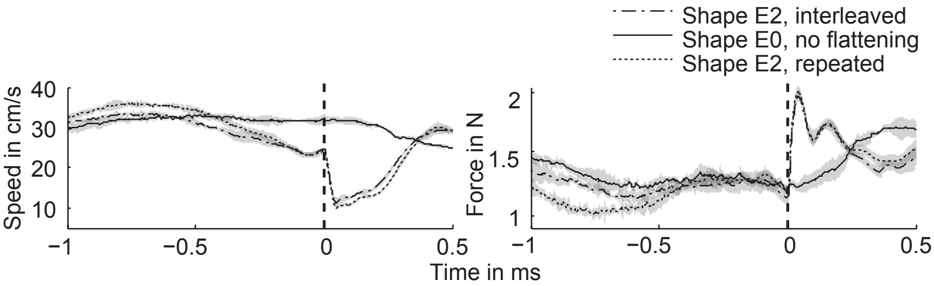

Figure 7.5 Finger speed (left) and contact force (right) for subjects exploring the 0-deg tilted ellipses in different conditions. The dash-dotted line represents data of shape E2 (0-deg tilted ellipse with flattening) for trials that were interleaved with the other shapes; the solid line represents data of shape E0 (0-deg tilted ellipse without flattening); the dotted line represents data of shape E2 for a block of five consecutively repeated trials presented at the end of the experiment. Each line shows the mean across subjects, repetitions, and laps 2–5 (6 subjects × 5 repetitions × 4 laps = 120 time traces), aligned to the onset of flattening (vertical, dashed line at t = 0). Shaded area represents the standard deviation.

of flattening, most subjects showed a significant increase compared to the non-flattened shape.

Thus, in consecutive laps around the same shape, subjects failed to exhibit a consistently successful strategy for precisely anticipating time or location of the corner. To further investigate the subjects' ability to learn to anticipate, at the end of each experiment we presented the very same shape (shape E2) in five repeated trials, and subjects were informed accordingly. Within each trial, subjects completed five sequential laps (as in the main block of trials where trials with all shapes were presented in random order). We compared the performance during this final block (shape E2, repeated) with the performance for the same shape from the main block (shape E2, interleaved), and with the control shape (shape E0, no flattening). In figure 7.5, the traces represent the mean value across subjects ($n = 6$), trial repetitions ($n = 5$), and laps 2–5 ($n = 4$). The shaded areas represent the standard deviations.

Speed (figure 7.5, left panel) was similar for repeated trials (dotted traces) and interleaved trials (dash-dotted traces). We did not find a significant difference in trial durations between the repeated trials and the interleaved trials: the mean (SD) across subjects was 20.5 s (4.2 s) and 19.1 s (2.1 s), respectively, $p = 0.11$ (two-sided t test). In both cases, the deceleration of the finger started about 500 ms before the onset of flattening, compared to the control shape (red trace).

The amount of contact force (figure 7.5, right panel) just prior to the onset of flattening did not differ between repeated E2 (dotted trace), interleaved E2 (dash-dotted trace) and the control shape E0 (solid line). Moreover, we did not find a difference in the force of impact between the repeated and interleaved trials. Before –400 ms, the force was lower for the repeated trials, compared to the other two conditions. Thus, although subjects modulated contact force during the repeated trials, this adjustment was not timed to the onset of flattening.

The comparison of speed and force between a block of repeated trials and the interleaved trials confirmed and extended our conclusion that subjects could not learn to

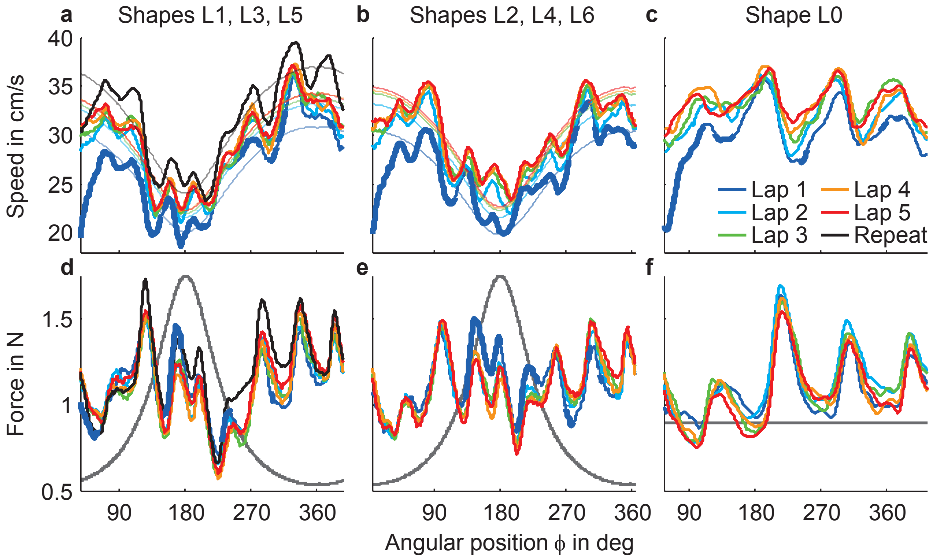

Figure 7.6 Finger speed (panels a–c) and contact force (panels d–f) pooled across subjects ($n = 6$) and repetitions ($n = 5$) of counterclockwise rotated shapes L1, L3, L5 (panels a and c), clockwise rotated shapes L2, L4, L6 (panels b and e), and shape L0 (circle; panels c and f). The x-axis represents angular position ϕ (equation 7.1); the origin $\phi = 0$ is indicated by the dashed lines in figure 7.7. Notice that data analysis started 10 cm from the starting position at the bottom of the shape (solid lines in figure 7.7), which is at a different angular position for the counterclockwise shapes, clockwise shapes, and circle. Each color represents data of a single lap. In panels d–f, the gray lines indicate the amount of curvature. In panels a and b, the thin lines show the two-thirds power law fit. In panels a and d, the black lines represent data of shape L3 for a block of five repeated trials presented at the end of the experiment.

precisely anticipate an abrupt, haptic event. This raised the question of whether subjects have the ability to predict gradual changes in the surface of virtual shapes, which is the topic of the next section.

Anticipation of gradual changes in curvature – experiment 2 In experiment 2, we measured the finger speed and contact force for Limaçon shapes in different orientations, and circles (figure 7.2, right). The Limaçon shape has two important properties. First, it has a continuous change in curvature generated with cosine functions, which allowed us to investigate the effect of a gradual change in surface curvature instead of an abrupt change as in experiment 1. Second, for the sake of discussion, the shape can be subdivided into a small and a large loop. The small loop acted as a single haptic event, analogous to the flattened section of the ellipses in experiment 1.

Figure 7.6a shows the finger speed as a function of angular position along the shape, for laps 1–5 (cool to warm colors, respectively), averaged across subjects ($n = 6$), counterclockwise rotated shapes L1, L3, L5 ($n = 3$) and repetitions ($n = 5$). Speed during the first lap (dark blue) was generally lower than the subsequent laps, with significant differences (Mann-Whitney U test, $p < 0.05$) indicated by thicker sections of the dark blue lines.

It is known that for various types of voluntary movements, finger speed is inversely related to the curvature of the finger trajectory, following the so-called two-thirds power law (see *Methods*). Therefore, we hypothesized that if subjects can anticipate the shape of the contour, finger speed might obey this law. In figure 7.6a, the thinner lines show the average model prediction calculated by fitting equation 7.2 to individual traces for each lap and then averaging. These fits show that the subject's finger speed generally followed the prediction of the power law. This was also true for most of the first lap (dark blue), even though subjects did not know which rotation was presented, and hence did not a priori know how the curvature would become the tightest. We found the same result for the clockwise rotated shapes L2, L4, L6 (figure 7.6b). Note that the maximum curvature, and hence the minimum speed, occurred at angular position $\phi = 180$ deg, which was encountered later in clockwise rotated shapes.

The circle (figure 7.6c) had a constant curvature and therefore, one would expect a more or less constant speed. Finger speed indeed had a constant baseline of about 32 cm/s, but on top of that, it showed a stereotypical modulation. Such modulations were also present in the Limaçon shapes, and cannot be attributed to noise, which was filtered out (see *Methods*), or random variability in tracing speed, since each line represents the average across 90 trials (30 trials for shape L0). We will return to this observation after first discussing the amount of contact force.

The bottom row of figure 7.6 shows the corresponding contact force for shapes L1, L3, L5 (panel d), shapes L2, L4, L6 (panel e) and shape L0 (panel f). The gray traces indicate the positional modulation of surface curvature. For both orientations of the Limaçon shape, the force was significantly higher in the beginning of the high-curvature section during the first lap (thick dark blue trace) than during the subsequent laps (other colors). Higher force is the mechanical result of moving into a tightening curve (similar to hitting a corner in experiment 1). Thus the reduction in contact force in laps 2–5 indicates improved curvature anticipation across laps.

However, even in lap 1, instead of a single peak in force in the first part of the small loop (the section with most rapidly increasing curvature), we generally found a series of peaks, arranged in a stereotypical way around the shape, also at parts with low curvature (figure 7.6d,e). If subjects did not anticipate the small loop of the Limaçon shapes, one might expect a higher contact force during the high-curvature sections, compared to the contact force when tracing the circle (figure 7.6f). Instead, the peaks in contact force in the first part of the small loop (between $\phi = 90$ and 180 deg in figure 7.6d,e) were significantly lower than the maximum value when tracing the circle (at $\phi = 215$ deg in figure 7.6f; Mann-Whitney U test, $p < 0.05$ for L1, L3, L5 and $p < 0.001$ for L2, L4, L6).

We also measured finger speed and contact force in a block with five repeats of shape L3 (black traces in figure 7.6a,d). In this situation, subjects had ample time to become familiar with the shape, which might explain why finger speed was slightly higher (figure 7.6a). The behavior followed a similar pattern as for the interleaved trials, indicating that the previous results are not an effect of the subjects' (lack of) familiarity with the shape.

Notice that in figure 7.6, we pooled the data across subjects. The reason is that, unlike in experiment 1, the results of experiment 2 were very consistent across subjects. All subjects had dominant finger speeds corresponding to the two-thirds power law, and had higher frequency speed and force modulations very similar to those shown by the average. For subjects S1, S3, S4, and S6, contact force during the high-curvature section in the first lap

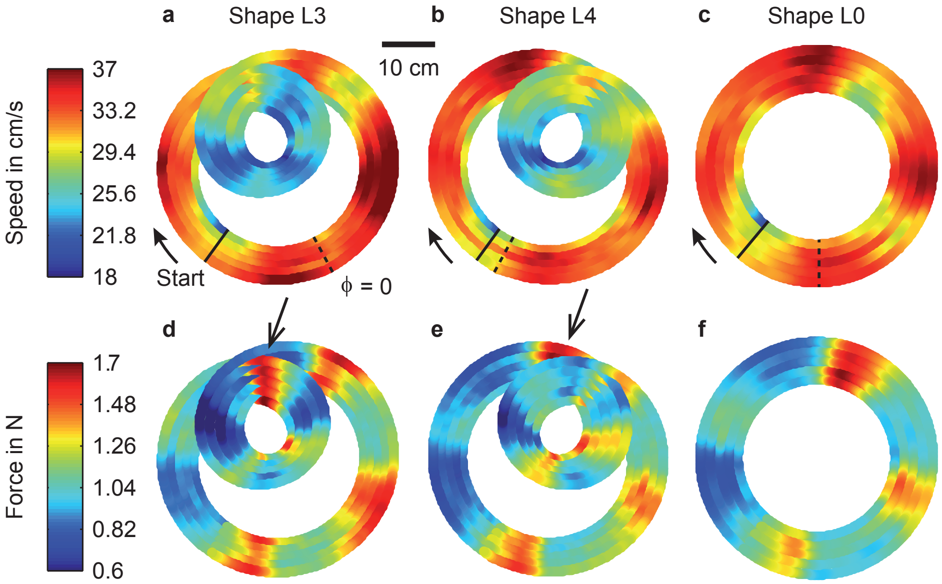

Figure 7.7 Finger speed (panels a–c) and contact force (panels d–f) pooled across subjects (n = 6), and pooled across all repetitions (n = 5) of shape L3 (panels a and d), L4 (panels b and e), L0 (panels c and f). Each drawing consists of five lines representing the laps, where the inner and outer lines correspond to lap 1 and lap 5, respectively. The start of the laps is indicated by the solid line with the arrow pointing in the movement direction (clockwise). The dashed lines show the origin of the angular position axes (figure 7.6). The arrows in panels d and e indicate a section of the Limaçon shapes where the contact force was high (see text for further explanation).

was significantly higher than during the subsequent laps. For all subjects, force during the high-curvature sections did not exceed values found during the remaining sections, and during the tracing of the circles. Therefore, the average behavior is representative of each individual subject.

Returning to the higher frequency speed and force modulations, notice that the contact force while tracing the circle (figure 7.6f) showed a similar modulation to finger speed (figure 7.6c), i.e., four peaks and troughs. Furthermore, the oscillation in speed and contact force in Limaçon shapes was not restricted to the high-curvature portions of the shape but was distributed along the whole path. This suggests that this modulation did not originate from the change in curvature. To investigate this in more detail, we present the same data in a spatial format. Figure 7.7 (top row) shows a heat map of finger speed for shape L3, L4 and L0 (panels a–c), pooled across subjects. Each line represents a single lap, where laps 1 and 5 are the inner and outer lines, respectively. This figure nicely illustrates that speed followed the two-thirds power law, since the speed was always low (blue) when the curvature was large (small loop) and high when the curvature was small (large loop), see figure 7.7a,b.

However, when one of the Limaçon shapes was rotated by 50 deg to match the other shape, the force patterns did not match (figure 7.7d,e). For example, the force was high just after the intersection point for shape L3, but before the intersection point for shape L4, as highlighted by the arrows. This is another indication that this force modulation was not the result of a change in curvature. Rather, the peaks and troughs seemed to occur at fixed positions in workspace, i.e., with respect to the subject.

This conclusion becomes evident when looking at speed and contact force while tracing the circle (panels c and f). The speed profile showed four peaks located at approximately 0, 90, 180 and 270 deg, visible as the dark red areas of the circle. These peaks coincided with the peaks in speed previously reported by Weiss and Flanders (2011, see figure 5c of their study). Force also showed a modulation with four peaks (yellow/red areas), rotated by approximately 20 deg in clockwise direction with respect to speed (compare panels c and f). Changes in curvature cannot be responsible for this pattern, since the curvature of a circle is constant. Thus, as previously discussed by Weiss and Flanders (2011), there is a spatial pattern in the speed/force modulation that is perhaps due to the biomechanics of the finger/hand/arm interacting with the Phantom robot in our setup. In the present study, this modulation was clearly not due to a lack of anticipation of the upcoming curvature. Subjects had no difficulty with curvature anticipation in laps 2–5.

7.4 Discussion

The goal of this study was to investigate the extent to which the somatosensory system can combine ongoing feedback with predictive mechanisms to guide the hand along unseen surfaces. Therefore, we measured finger speed and contact force during haptic exploration of virtual shapes with abrupt or gradual changes in curvature. Subjects repeated their exploration in sequential laps, which allowed us to dissociate relatively pure feedback control (during the first lap), from feedback combined with learned anticipation of a point in time or space (experiment 1) or anticipation due to extrapolation of surface contours (experiment 2).

Corners We found that subjects were poor in predicting an abrupt, haptic event (experiment 1). Subjects slowed down before the onset of a flattened section of the shape, but both the timing and the location were quite early and variable (table 7.1). Thus, memories were insufficient to precisely anticipate the transition from a curved to a straight section of the shape, even when subjects were allowed 25 consecutive laps (5 consecutive trials with 5 laps each, figure 7.5).

Previous work showed that the somatosensory system can quite accurately extract the shapes of planar, virtual objects (Henriques and Soechting, 2003). However, when subjects have to judge the shape of complex objects, their percept is biased toward simple geometric shapes and symmetric shapes (Ehrich et al., 2008). Also, people are better in haptically aligning rods along the cardinal axes than along axes with an oblique orientation (Hermens and Gielen, 2003; Kappers and Koenderink, 1999). Therefore, if subjects used a mental image of the shape's geometry obtained in the first lap for predicting the exact course of the second lap, it is likely that the localization of the corner between a curved and straight section was also biased, being especially difficult for tilted shapes E1 and E3. However in the present study subjects also had difficulty locating an upcoming corner in a shape symmetric around a cardinal axis (shape E2).

Another potential reason for the poor performance could have been that subjects did not perceive the flattened sections, i.e., they did not notice the corner. Our preliminary experiments showed that subjects can have difficulties in judging whether an ellipse contained a flattened section or not (Tramper et al., 2012). However, in our previous study, based on verbal reports, flattening was always detected for the ellipses used in the present experiment (with a 3:2-ratio of major axis to minor axis).

Smooth curves Although the Limaçon shapes (experiment 2) were more complex, speed nicely followed the two-thirds power law prediction (figure 7.6a,b). Also, subjects kept the amount of contact force in the same range as for tracing a circle, which is an easy shape to trace (figure 7.6d–f). Since it is known that the percept of complex shapes can be biased (Henriques and Soechting, 2005; Soechting et al., 2006), these results cannot be fully explained by the use of memory to guide the movement. If subjects could not anticipate the high-curvature section of the shape, one would expect the force to increase along with the increase in curvature, because subjects would keep hitting the wall of the tube. But this hypothesis did not fit the pattern of force modulation. Therefore, we believe that in this situation, anticipatory predictions came into play.

As outlined in section 7.1, the human visuomotor system combines feedback and feedforward mechanisms to control ongoing movements. Soechting et al. (2010) proposed a model with a predictive component for smooth pursuit eye movements, consisting of a low-pass filtered target acceleration signal. Suppose that the somatosensory system uses a similar predictive signal to guide the hand along a surface. In this case, the target is not a moving visual stimulus, but the desired finger movement along the shape. In general, natural movements are smooth and follow the two-thirds power law, that is, the velocity of the controlled limb is inversely related to the curvature of the trajectory. Thus, let us assume that the desired finger trajectory was equal to the shape of the surface with a finger speed that followed the power-law prediction. In experiment 1, the onset of the flattened section was not preceded by an associated change in curvature. Therefore, the predictive component given by the acceleration of the finger was not helpful for the abrupt change in curvature. In experiment 2, we used shapes with a continuous change in curvature. Therefore, acceleration of the finger was a good predictor for the upcoming surface curvature, and hence, subjects were able to predict the high-curvature loop of the Limaçon shape using extrapolation.

Conclusions To summarize, this study demonstrated that the haptic system is poor in predicting features at a particular spatial location, but in contrast, can successfully anticipate smooth changes in the contour being followed. The quality of predictions depends on whether the haptic input of the preceding surface is informative for the upcoming surface. In order to anticipate an abrupt change in curvature, the subject could potentially have used a memory of the location of the corner, or the position of the arm when the finger reached the corner. But this type of somatosensory memory may be biased and inaccurate (Rincon-Gonzalez et al., 2011).

Although the anatomy and physiology of somatosensory perception is well known, few previous studies have investigated the neural control mechanism for haptic guidance of contour following at the human fingertip. Studies of the neural control of active sensing are perhaps more abundant in the whisker system (Prescott et al., 2011), and it appears that whiskered tetrapods, who often explore during locomotion in darkness, may use different control strategies for accumulating information over space and time compared to humans

(Horev et al., 2011). As an approach to the topic of human haptic guidance we make an analogy to control mechanisms for visually-guided eye movements, which have been more thoroughly studied in the past. However, to postulate a negative feedback loop to guide fingertip movements, one must specify a control signal, i.e., the parameter that is fed back and driven toward zero. For smooth pursuit eye movement this is clearly the retinal slip velocity, i.e., the difference between target motion and eye motion (Krauzlis and Lisberger, 1994). For haptically exploring the shape of a smooth surface, Weiss and Flanders (2011) suggested that the control may be aimed at keeping a consistent level of contact force, which might serve the purpose of maintaining pressure on tactile receptors within a certain range of their sensitivities. This might then be coupled with a strategy for perceiving textures or irregular features of the explored surface (see for example Smith et al., 2002).

8

Nederlandse samenvatting

In het dagelijks leven maken we een enorme verscheidenheid aan bewegingen zonder dat we steeds na hoeven te denken over hoe we ieder lichaamsdeel afzonderlijk moeten aansturen. Vrijwel al onze bewegingen, zoals bijvoorbeeld naar de trein lopen of een kopje thee drinken, lijken automatisch te gaan. Zodra we besloten hebben dat we ons moeten haasten om de trein te halen, beginnen we te lopen zonder na te denken over waar we onze voeten neer moeten zetten of welke stapgrootte het meest geschikt is. En als we een slok thee willen nemen, denken we niet bewust na over hoe we iedere vinger moeten bewegen om het kopje vast te pakken, of hoeveel kracht we nodig hebben om het op te tillen.

Al deze onderliggende beslissingen worden genomen door ons brein, gebruik makend van voorspellingen en ervaringen voorafgaand aan de beweging (voorwaartse koppeling), en terugkoppeling van zintuiglijke informatie tijdens de beweging. Omdat we tijdens onze kinderjaren geleerd hebben hoe we voorwerpen moeten vastpakken, "weet" ons brein welke van de meer dan 600 spieren nodig zijn om het kopje van tafel op te pakken. Dit is een voorbeeld van aansturing door voorwaartse koppeling aangezien het brein ervaringen uit het verleden gebruikt om de huidige beweging uit te voeren. Deze manier van bewegingen aansturen kan echter problemen opleveren omdat we vooraf niet alle factoren kennen die de beweging kunnen beïnvloeden. Als onze elleboog bijvoorbeeld iets raakt terwijl we een beweging naar het kopje maken, wordt het pad dat de hand aflegt onverwachts gewijzigd. Als we hiervoor niet zouden corrigeren, zouden we naast het kopje grijpen. Daarnaast weten we wellicht niet of het kopje vol of leeg is, en weten we dus niet exact hoeveel kracht er nodig is om het kopje op te tillen.

Om met deze onzekerheden rekening te houden, stuurt het brein bewegingen bij doordat zintuiglijke informatie wordt teruggekoppeld. Tijdens een beweging gebruiken we onze ogen, oren en tast om beelden, geluiden en texturen waar te nemen. Op die manier kunnen we bepalen of het kopje thee vol of leeg is, bijvoorbeeld door er simpelweg in te kijken of door te voelen hoe zwaar het is via speciale zintuigen in de spieren. Deze informatie moet vanaf de zintuigen naar de hersenen worden gestuurd, en is daarom niet direct beschikbaar voor het aansturen van de beweging. Er is echter ook informatie over de beweging, zoals ervaringen uit het verleden, opgeslagen in ons geheugen. Deze informatie is via voorwaartse koppeling direct beschikbaar voor het brein. In dit proefschrift wordt onderzocht hoe ons brein voorwaartse koppeling en zintuiglijke terugkoppeling combineert om bewegingen te genereren en bij te sturen.

8.1 Visuele terugkoppeling

Ons visueel systeem is een van de belangrijkste bronnen van zintuiglijke informatie. We bewegen onze ogen vrijwel onophoudelijk naar vaste en bewegende objecten in de ruimte. We gebruiken snelle oogbewegingen (saccades) om naar een nieuwe locatie te kijken, bijvoorbeeld het volgende woord in deze zin. We maken ongeveer drie van deze saccades per seconde. Deze frequentie is zo hoog omdat het deel van ons netvlies waar de gezichtsscherpte het hoogst is (de gele vlek) heel erg klein is en slechts 2 graden van ons visuele veld beslaat (Purves et al., 2004). Om een compleet en gedetailleerd beeld van onze omgeving te verkrijgen, moeten we daarom onze ogen bewegen. Saccades zijn snel. Ze kunnen snelheden bereiken van meer dan 700 graden per seconde (Carpenter, 1988). Tijdens deze oogbewegingen kunnen we geen beelden waarnemen en daarom is het gunstig om de duur van een saccade zo klein mogelijk te houden. Het netvlies bestaat uit lichtgevoelige receptoren (staafjes en kegeltjes) die binnenkomende fotonen invangen en omzetten in actiepotentialen. Dit proces verloopt met een tijdconstante van ongeveer 20 ms (Friedburg et al., 2004). Om de visuele informatie om te zetten in neurale signalen moeten de ogen dus even stilstaan. Deze periodes heten fixaties en de lengte daarvan varieert tussen ongeveer 10 ms en enkele seconden.

Voor het volgen van een bewegend object gebruiken we een ander type oogbeweging, aangeduid met de term 'oogvolgbeweging'. De snelheid van deze oogbeweging komt overeen met de snelheid van het bewegende object, zodat dit object wordt afgebeeld op de gele vlek van het netvlies. Er kunnen snelheden van 100 graden per seconde bereikt worden (Meyer et al., 1985), maar afhankelijk van de snelheid en voorspelbaarheid van de beweging zijn er extra saccades nodig om het object op de gele vlek te houden (De Brouwer et al., 2002). Om ons blikveld te verplaatsen tussen nabij en veraf gelegen objecten gebruiken we vergentie-oogbewegingen. De ogen convergeren of divergeren zodat de zichtlijnen van ieder oog kruisen daar waar het object zich bevindt. Deze oogbewegingen zijn relatief langzaam (Chaturvedi en Van Gisbergen, 1998).

In ons dagelijks leven gebruiken we een combinatie van saccades, oogvolgbewegingen en vergentie-oogbewegingen om ons blikveld op relevante objecten in onze omgeving te richten. Deze oogbewegingen voorzien het brein van visuele terugkoppeling om onze bewegingen te kunnen bijsturen. Het meten van oogbewegingen tijdens het uitvoeren van bewegingen levert daarom extra informatie over hoe het brein bewegingen aanstuurt. Tijdens alledaagse taken zoals autorijden (Land en Lee, 1994), een kopje thee zetten (Land et al., 1999) of een boterham smeren (Hayhoe et al., 2003) scannen onze ogen taakrelevante locaties in de omgeving, vooruitlopend op de beweging die gaat volgen. Op die manier kan ons bewegingsapparaat visuele terugkoppeling gebruiken om de beweging te plannen en uit te voeren.

In **hoofdstuk 2** onderzochten we oog-handcoördinatie in drie dimensies. Zoals hierboven beschreven lopen oogbewegingen vooruit op handbewegingen. Aangezien verschillende typen oogbewegingen verschillende snelheden hebben, hebben we het vooruitlopen van de ogen ten opzichte van de hand onderzocht in diepte en in het frontale vlak. Proefpersonen moesten een bewegend object met hun vinger volgen of moesten met hun vinger langs een drie-dimensionaal pad bewegen. In de eerstgenoemde taak liep het oog gemiddeld 28 ms (standaard fout (SE) 6 ms) voor op de vinger in het frontale vlak. In diepterichting liep het oog echter 95 ms (SE 39 ms) achter op de vinger. In de tweede taak liep het oog gemiddeld 151 ms (SE 36 ms) voor in diepte en 287 ms (SE 13 ms) voor in het frontale vlak. Daarnaast vonden we tijdens de tweede taak dat het voorlopen van oog op hand in het frontale vlak omgekeerd evenredig was met de snelheid van de vinger. Dit suggereert dat onze ogen een vaste afstand van ongeveer 2.6 cm (variërend van 1.5 cm tot 3.5 cm per proefpersoon) voorlopen op de vinger, en dus niet met een vaste tijd voorlopen zoals tot nu toe werd aangenomen.

Hoofdstuk 2 laat tevens zien dat als we een handbeweging maken naar een visueel doel, het oog in tijd en ruimte voorloopt op de hand door middel van een serie van saccades afgewisseld met fixaties. Wetenschappers hebben aangetoond dat tijdens complexe bewegingen, oogvolgbewegingen en saccades elkaar wederzijds kunnen beïnvloeden. Ook zijn er steeds meer aanwijzingen dat oogvolgbewegingen ook kunnen optreden als er geen bewegende objecten op het netvlies vallen. In **hoofdstuk 3** onderzochten we of een combinatie van oogvolgbewegingen en saccades gebruikt kan worden om een beweging in een complexe omgeving te leiden en bij te sturen. Om dit te onderzoeken gebruikten we een computerspel waarbij proefpersonen met behulp van hun duimen twee cursors naar een doel op het scherm moesten bewegen zonder tussenliggende obstakels te raken. We vonden dat het oog voorliep op de cursors door middel van een serie saccades, afgewisseld met fixaties en oogvolgbewegingen. Deze volgbewegingen waren onafhankelijk van de positie en snelheid van de cursors. Dit betekent dat een combinatie van snelle en langzame oogbewegingen, aangestuurd door niet-visuele informatie, in staat was de cursorbeweging te leiden. Een mogelijke verklaring voor dit gedrag is dat het visueel systeem de omgeving wil verkennen om de paden van de cursors te plannen, maar tegelijkertijd ook wil controleren of de cursors langs de gewenste paden bewegen.

8.2 Vertragingen in signaaloverdracht

Stel je voor dat je gevraagd wordt een bewegende cursor op een computerscherm te volgen met je vinger. Tussen de tijd dat de cursor van positie verandert en de tijd dat je je beweging corrigeert, vindt een reeks neurofysiologische en fysische processen plaats. Fotonen uitgezonden door het computerscherm worden geabsorbeerd door lichtgevoelige receptoren (staafjes en kegeltjes) in het netvlies. Dit veroorzaakt een serie van elektrische ontladingen, ook wel actiepotentialen genoemd, die vervolgens vanaf de receptoren via de optische zenuwen en de thalamus de visuele schors bereiken (Purves et al., 2004). Vanaf daar wordt de informatie via andere hersengebieden doorgestuurd naar de motorische schors. Hier wordt bepaald hoe de betreffende spieren moeten worden geactiveerd om je arm naar de gewenste positie te bewegen. Dit signaal wordt vervolgens naar de spieren gestuurd, die op hun beurt een kracht opbouwen die groot genoeg is om de arm in beweging te brengen. Al deze processen kosten tijd. Dit betekent dat de visuele informatie over de cursorpositie op het scherm niet direct beschikbaar is voor het brein, en dat we daarom niet meteen onze arm naar de gewenste positie kunnen bewegen. In praktijk kost het minimaal 100–150 ms voordat een verandering in visuele informatie de armbeweging bij kan sturen (Day en Lyon, 2000). Bovengenoemd voorbeeld laat zien dat het tijd kost voordat zintuiglijke informatie beschikbaar is om bewegingen bij te sturen. Met andere woorden, de zintuiglijke informatie is al verouderd voordat het kan worden gebruikt om een reeds in gang gezette beweging bij te sturen. Toch blijkt uit experimenten (hoofdstuk 2) en onze eigen ervaring dat we bewegende objecten zonder vertraging kunnen volgen. Er lijkt dus helemaal geen tijdvertraging op te treden. In paragraaf 8.4 en 8.5 wordt door middel van modellen uitgelegd hoe dit kan.

8.3 Ruis en onzekerheid

Het brein codeert informatie via een serie actiepotentialen die gegenereerd worden door speciale cellen: de neuronen. De intra- en extracellulaire vloeistof van een neuron bevatten geladen deeltjes (ionen) en zijn door het celmembraan van elkaar gescheiden. Tijdens een actiepotentiaal passeren de ionen het membraan via kanalen en stromen van de kant met een hoge ionenconcentratie naar de kant met een lage concentratie. Dit proces heet diffusie en veroorzaakt een elektrische ontlading, ofwel een actiepotentiaal. Ionenpompen in het celmembraan brengen de ionenconcentratie terug naar het beginniveau, waarna het neuron klaar is om het volgende actiepotentiaal te generen (Purves et al., 2004). Het diffusieproces is een stochastisch proces, wat betekent dat het aantal ionen dat het membraan passeert kan variëren, zelfs al zouden alle eigenschappen van het neuron hetzelfde blijven (White et al., 2000). Dit betekent dat zelfs als een neuron steeds exact dezelfde informatie binnenkrijgt, de resulterende series van actiepotentialen een klein beetje van elkaar verschillen. Aangezien we vaak niet weten waar deze variatie precies vandaan komt, noemen we dit 'ruis'. Tijdens iedere stap in het aansturingsproces wordt ruis geïntroduceerd. Ruis ontstaat als fysische eigenschappen zoals licht, geluid en temperatuur worden omgezet in neurale signalen. Het ontstaat als actiepotentialen worden gegenereerd en doorgestuurd naar het volgende neuron via synapsen (de verbindingen tussen neuronen). Ruis speelt ook een rol wanneer actiepotentialen aankomen bij de spieren waar ze worden opgezet in spierkracht.

Naast ruis dient het brein ook rekening te houden met andere vormen van onzekerheid. Met onzekerheid bedoelen we hier het ontbreken van alle informatie over onze omgeving, over de taak die we op dat moment uitvoeren, of over de huidige toestand van ons lichaam. Naast vertragingen en ruis zijn er nog veel meer bronnen van onzekerheid. Tijdens het lopen weten we bijvoorbeeld niet exact hoe vlak de ondergrond is of de mate van vermoeidheid van onze spieren. Als we een kopje thee van tafel pakken weten we niet precies hoe zwaar het is. Doordat de hoeveelheid receptoren in onze vingertoppen een bovengrens heeft, weten we niet exact waar onze vingers zich op het toetsenbord bevinden als we een email typen. Ook in situaties waarin we met iemand anders interactie aangaan, zoals tijdens het praten met een vriend of als we samen met iemand sporten, treedt onzekerheid op. Dit komt omdat we niet vooraf weten wat de ander gaat zeggen of welke beweging de tegenstander gaat maken. Hoe ons bewegingsapparaat hiermee zou kunnen omgaan wordt besproken in paragraaf 8.5.

8.4 Leren van fouten door middel van terugkoppeling

Door vertragingen in signaaloverdracht (paragraaf 8.2) is de informatie van onze zintuigen altijd verouderd. Tijdens langzame bewegingen van enkele seconden of langer is er ruim voldoende tijd om een fout tussen de werkelijke toestand van ons lichaam en de toestand zoals waargenomen door onze zintuigen te corrigeren. Voor snelle bewegingen van een halve seconde of korter is de terugkoppeling van zintuiglijke informatie echter fors vertraagd ten opzichte van de duur van de beweging (Franklin en Wolpert, 2011). Saccades zijn hier een goed voorbeeld van. Dit zijn zeer snelle oogbewegingen die soms slechts 30 ms duren (Smit et al., 1987). Dit is veel korter dan de tijd die het visueel systeem nodig heeft om de oogbeweging eventueel te corrigeren. Toch zijn deze oogbewegingen zeer nauwkeurig, hoe komt dat?

Een van de oplossingen die bedacht is gaat er vanuit dat het brein leert van fouten uit het verleden door middel van terugkoppeling (Wolpert et al., 1998; Wolpert en Ghahramani, 2000), zie het model in figuur 8.1. Stel dat we een cirkel willen tekenen op een stuk papier. Aangezien we uit ervaring weten hoe een cirkel eruit ziet, is het gewenste pad dat onze hand met het potlood moet afleggen (namelijk een perfecte cirkel) bekend. Ons brein moet dit gewenste pad omzetten naar de juiste commando's om de spieren in de arm aan te

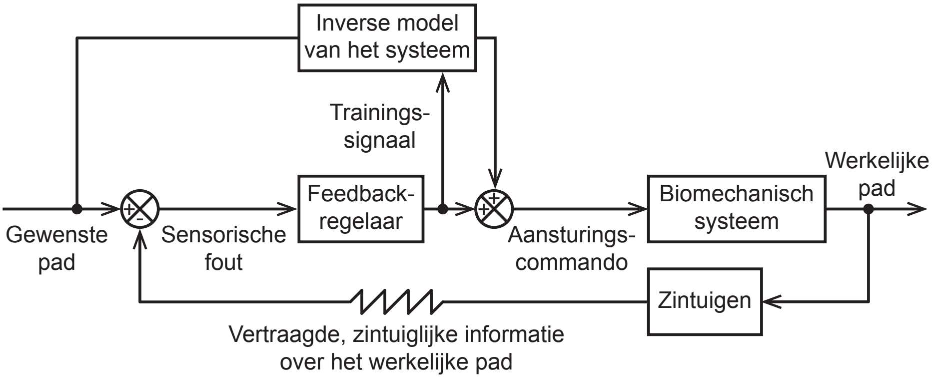

Figure 8.1 Dit model beschrijft hoe het brein bewegingen van bijvoorbeeld de arm (hier het 'biomechanisch systeem' genoemd) kan aansturen (Wolpert et al., 1998). Het 'inverse model' representeert het neurale netwerk dat het gewenste pad van de arm omzet in de bijbehorende aansturingscommando's, die vervolgens de spieren van de arm activeren. Dit heet voorwaartse aansturing. Vanwege imperfecties in het inverse model en vanwege ruis zal het werkelijke pad niet gelijk zijn aan het gewenste pad. Deze fout wordt door onze zintuigen geregistreerd en vertraagd teruggezonden naar de 'feedback-regelaar'. Deze regelaar zet de sensorische fout om in een commando om deze fout te corrigeren. Dit wordt zintuiglijke terugkoppeling genoemd. Het commando kan eveneens gebruikt worden als trainingssignaal voor het inverse model, om zo de onvolkomenheden te verkleinen. Op deze manier "leert" het model van fouten door middel van terugkoppeling.

sturen, resulterend in het daadwerkelijke pad van de handbeweging. Het onderdeel van het model dat het gewenste pad omzet naar de bijbehorende bewegingscommando's heet het inverse model. In ons voorbeeld is het inverse model van "hand met potlood" tijdens onze kinderjaren aangeleerd. Aangezien hierbij alleen ervaringen uit het verleden gebruikt worden om de huidige beweging uit te voeren, noemen we dit voorwaartse aansturing.

Niet alleen tijdens het leren maar ook als we de taak volledig onder de knie hebben, is het daadwerkelijke pad van het potlood niet exact gelijk aan het gewenste pad dat we voor ogen hadden. Onzekerheden zoals het gewicht van het potlood, de wrijving tussen potlood en papier, en de mate van vermoeidheid van onze spieren zorgen ervoor dat een exacte vertaling van het gewenste pad naar het daadwerkelijke pad onmogelijk is. Daarom gebruiken we visuele en haptische terugkoppeling (paragraaf 8.1 en 8.6) om te verifiëren of het daadwerkelijke pad overeenkomt met het gewenste pad. Zo niet, dan heeft het brein een extra commando nodig om deze zintuiglijke fout te corrigeren. In dit model wordt aangenomen dat dit commando wordt gegenereerd door de feedback-regelaar. Het uitgangssignaal van de feedback-regelaar wordt niet alleen gebruikt om een in gang gezette beweging bij te sturen, maar ook om het inverse model te trainen. We gebruiken dus een teruggekoppelde zintuiglijke fout om een beweging te leren en uit te voeren.

Om de zintuiglijke fout te berekenen moet op enig moment het gewenste pad worden vergeleken met de verouderde zintuiglijke informatie. Deze twee signalen lopen dus niet synchroon en daarom kunnen ze niet direct met elkaar worden vergeleken. Met andere woorden, het model van Wolpert et al. (1998) houdt geen rekening met de vertragingen die optreden tijdens het genereren van bewegingen. Een mogelijke oplossing is dat het neurale systeem niet wacht totdat de zintuiglijke informatie beschikbaar is, maar dat deze informatie wordt geschat op basis van recente zintuiglijke informatie. Hierdoor is de zintuiglijke informatie direct beschikbaar om de (geschatte) zintuiglijke fout te berekenen. Dit is het onderwerp van de volgende paragraaf.

8.5 Optimale aansturing via terugkoppeling

We beschikken over meer dan 200 gewrichten en 600 spieren om een haast oneindige verscheidenheid aan bewegingen uit te kunnen voeren (Franklin en Wolpert, 2011). Daarnaast stelt deze grote hoeveelheid gewrichten en spieren ons in staat om een bepaalde beweging op oneindig veel verschillende manieren uit te voeren. Als we bijvoorbeeld een kopje thee willen pakken, kunnen we verschillende combinaties van spieren gebruiken, en kunnen we verschillende paden kiezen waarlangs we onze hand bewegen, waarbij we bovendien de handsnelheid kunnen variëren. Het is opvallend dat we een dergelijke beweging desondanks uitvoeren op één bepaalde manier, namelijk met een licht gekromd pad en een klokvormig snelheidsprofiel van de hand (Atkeson en Hollerbach, 1985).

Lange tijd hebben wetenschappers zich afgevraagd waarom mensen kiezen om een beweging op één bepaalde manier uit te voeren terwijl er oneindig veel mogelijkheden zijn. Blijkbaar reduceert ons brein het aantal mogelijke oplossingen om zo de aansturing van bewegingen te vereenvoudigen. Dit kun je bereiken door aan te nemen dat de beweging zo optimaal mogelijk is ten opzichte van een aantal fysische eigenschappen. De theorie die dit idee wiskundig beschrijft heet 'optimale aansturing' (Todorov en Jordan, 2002; Todorov, 2004; Kappen, 2005b). De beste oplossing voor een bepaald aansturingsprobleem wordt gevonden door een set van mogelijke oplossingen te optimaliseren. Iedere oplossing bestaat uit een reeks van acties en aan elk van deze acties zijn strafpunten gekoppeld. Met behulp van optimalisatietechnieken wordt gekeken voor welke oplossing het totaal aantal strafpunten, uitgedrukt in een 'kostenfunctie', zo klein mogelijk is.

De optimale oplossing van een aansturingsprobleem bestaat dus uit een reeks van acties waarvoor de totale kosten geminimaliseerd is. Voor het aansturen van bewegingen wordt meestal gebruik gemaakt van een kostenfunctie die rekening houdt met de snelheid, energie of precisie van de beweging. Als je bijvoorbeeld je tegenstander wilt verslaan tijdens een potje squash, dan wil je de bal zo nauwkeurig mogelijk raken. Daarnaast wil je ook dat iedere beweging zo min mogelijk energie kost, aangezien je niet eerder uitgeput wilt raken dan je tegenstander. Het minimaliseren van de energieconsumptie en het maximaliseren van je prestatie levert je de optimale aansturing, bestaande uit een reeks commando's (acties) die de juiste spieren aansturen om de bal te raken.

Het model dat leert van fouten door middel van terugkoppeling (zie paragraaf 8.4, figuur 8.1) bevat de aanname dat de zintuiglijke informatie een waarheidsgetrouw beeld geeft van de toestand van het lichaam en de omgeving. Met andere woorden, dat model houdt geen rekening met ruis en onzekerheid in het zintuiglijke signaal. Stochastische optimale terugkoppeling kan wel rekening houden met ruis en onzekerheid (Todorov en Jordan, 2002; Scot, 2004; Todorov, 2004; Kappen, 2005b), zie het model in figuur 8.2. Dit model maakt gebruik van schattingen van de toestand van het lichaam in plaats van de werkelijke toestand. De reden is dat de werkelijke toestand, aangeleverd door zintuiglijke informatie, vertraagd binnenkomt en ruis bevat waardoor dit signaal niet direct gebruikt kan worden.

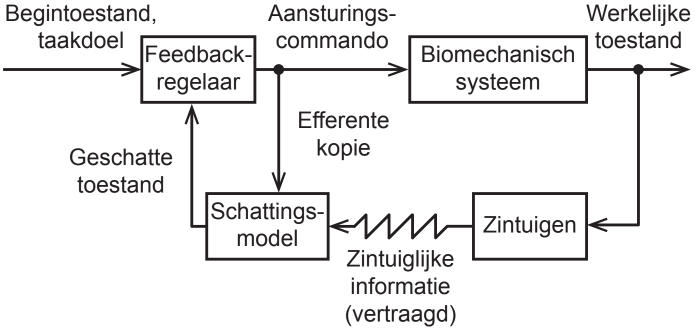

Figure 8.2 Het aansturingsmodel met stochastische optimale terugkoppeling (Todorov, 2004) is een model dat het aansturen van bewegingen beschrijft. Op basis van het taakdoel en de begintoestand van het 'biomechanisch systeem' (bijvoorbeeld de ogen, het lichaam, of een arm) genereert de 'feedback-regelaar' een commando dat het systeem aanstuurt. Het model gebruikt een 'schattingsmodel' dat de optimale, geschatte toestand van het systeem doorgeeft aan de feedback-regelaar. Deze schatting wordt gemaakt op basis van vertraagde en onnauwkeurige zintuiglijke informatie, en een kopie van het aansturingscommando ('efferente kopie').

Het model (figuur 8.2) neemt aan dat het taakdoel en de begintoestand van het 'biomechanisch systeem' (bijvoorbeeld de arm) bekend is bij de 'feedback-regelaar'. Het 'schattingsmodel' geeft de optimale, geschatte toestand van het systeem door aan de feedback-regelaar. Het schattingsmodel voorspelt de gevolgen van het zojuist gegenereerde aansturingscommando voor de stroom aan zintuiglijke informatie, gebruik makend van een kopie van dat commando ('efferente kopie'; Crapse en Sommer, 2008). Deze voorspelling, de werkelijke (vertraagde en onzekere) zintuiglijke informatie, en de dynamica van het systeem worden gewogen op basis van de bijbehorende nauwkeurigheid, om zo de toestand van het lichaam (bijvoorbeeld de positie van de arm) te bepalen. De feedback-regelaar vergelijkt deze schatting met het taakdoel en gebruikt dit verschil om het aansturingscommando te genereren. Omdat dit commando is gebaseerd op een optimale schatting, is de reeks van commando's gelijk aan de optimale oplossing voor het aansturingsprobleem. Het schattingsmodel kan gebruik maken van allerlei soorten informatie, bijvoorbeeld ervaringen uit het verleden of toekomstige voorspellingen, waardoor de feedback-regelaar rekening kan houden met verstoringen en onzekerheid door de in gang gezette beweging bij te sturen.

In **hoofdstuk 4** hebben we een aansturingsmodel met stochastische terugkoppeling gebruikt om oog-handcoördinatie te beschrijven. We gebruikten dezelfde opzet als in hoofdstuk 3, maar deze keer lieten we een computer naar de optimale oplossing van het probleem zoeken. De taak was om twee cursors naar een doel te bewegen zonder tussenliggende obstakels te raken. De computer kon de virtuele omgeving (de cursors, obstakels en het doel) waarnemen door een oog over het scherm te laten bewegen. De koppeling tussen de waarneming (via het oog) en de beweging van de cursors werd bereikt door het systeem te modelleren met 17 variabelen. Stapsgewijs werd het optimale pad voor de twee cursors en het oog berekend. Tijdens iedere stap werd ruis toegevoegd aan de posities van de obstakels en het doel om onzekerheid te creëren over de exacte locaties van deze objecten. De nauwkeurigheid waarmee de computer kon beschikken over de locatie van obstakels, het doel en de cursors hing af van de afstand tussen het oog en het object. Op die manier simuleerden we dat slechts een klein deel van het netvlies objecten scherp kan waarnemen (zie paragraaf 8.1). De computer had als doel om de totale kosten te minimaliseren, bestaande uit (1) strafpunten als de cursors het doel niet hadden bereikt, (2) strafpunten als de cursors een van de obstakels raakten, en (3) kosten voor het bewegen van de cursors en het oog. Vervolgens vergeleken we de optimale oplossing van de computer met het daadwerkelijke gedrag van proefpersonen (zie hoofdstuk 3). Voor de meerderheid van de condities vonden we dat de computervoorspelling de volgorde en locatie van de fixaties alsmede de afgelegde paden van de cursors correct voorspelde.

Verschillende studies hebben aangetoond dat doelgerichte bewegingen kunnen worden beschreven met behulp van optimale aansturing via terugkoppeling. In dergelijke studies wordt vaak opgelegd dat deze beweging binnen een bepaalde tijd voltooid moet worden. Impliciet wordt dan aangenomen dat proefpersonen exact op de eindtijd het doel bereiken. Proefpersonen zouden echter een andere strategie kunnen hanteren, namelijk dat ze het doel bereiken voordat de eindtijd verstreken is. In **hoofdstuk 5** testten we of dit inderdaad het geval is door het standaard model van optimale aansturing te vergelijken met een nieuw model. Dit model bevat een extra kostenfunctie die afwijkingen van het biomechanisch systeem (bijvoorbeeld de hand) en het doel gedurende de hele beweging in rekening brengt. Beide modellen werden getoetst door proefpersonen met behulp van een joystick een balletje op een computerscherm naar een doel te laten sturen binnen een bepaalde eindtijd. We vonden dat in tegenstelling tot het klassieke model, het nieuwe model correct voorspelt dat proefpersonen het doel bereiken voordat de tijd verstreken is.

8.6 Haptische terugkoppeling

De term ‘haptisch’ verwijst naar het vermogen om de omgeving waar te nemen met behulp van tast. Haptische terugkoppeling wordt bijvoorbeeld geleverd door de toetsen op een toetsenbord of de trilmodus van een mobiele telefoon. Als we in het donker de muur aftasten op zoek naar de lichtschakelaar levert een afwijking in de textuur van de muur informatie over de locatie van de schakelaar. Haptische aansturing kan dus plaatsvinden door via zintuiglijke terugkoppeling de werkelijke zintuiglijke informatie te vergelijken met de verwachte zintuiglijke informatie, gebruik makend van een efferente kopie (Weiss en Flanders, 2011), zie het model in figuur 8.3.

Tijdens het aansturen van de beweging met behulp van haptische terugkoppeling stuurt het inverse model een commando naar het biomechanisch systeem, bijvoorbeeld de hand. De input van het inverse model is het verschil tussen de gewenste toestand en de werkelijke toestand van het systeem, beschikbaar via zintuiglijke terugkoppeling. Door vertragingen in signaaloverdracht (paragraaf 8.2) duurt het ongeveer 100 ms voordat de haptische terugkoppeling, geleverd door het somatosensorisch systeem, de in gang gezette beweging beweging kan corrigeren (Johansson en Flanagan, 2009). Daarom maakt het brein tevens een schatting van de werkelijke toestand door een kopie van het aansturingscommando (efferente kopie) te vergelijken met de vertraagde zintuiglijke informatie, zie blok C1 in figuur 8.3. De uitkomst van het inverse model is een commando dat de spieren van de arm aanstuurt zodat de juiste kracht wordt geleverd om de hand langs het gewenste pad te laten bewegen.

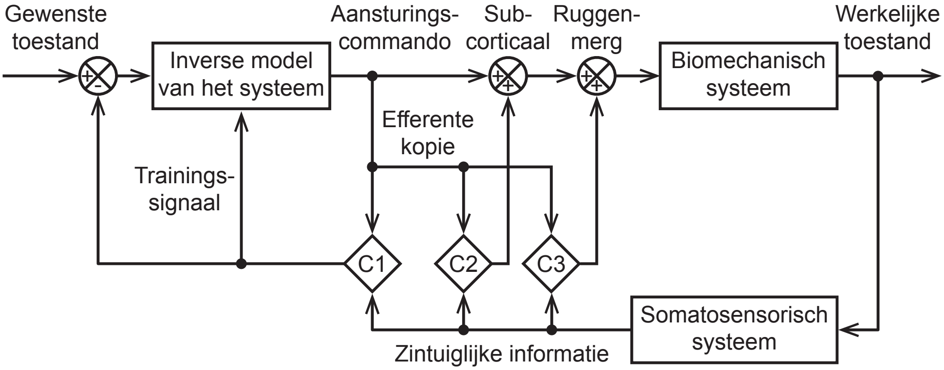

Figure 8.3 Haptische terugkoppeling bij het aansturen van bewegingen (Weiss en Flanders, 2011). Voorwaartse koppeling vindt plaats doordat het inverse model van het systeem een aansturingscommando naar het biomechanisch systeem stuurt. Het somatosensorisch systeem levert de haptische terugkoppeling die wordt vergeleken met een kopie van het aansturingscommando (efferente kopie) op verschillende niveaus in het centraal zenuwstelsel, weergegeven door de blokken C1–C3. De zintuiglijke terugkoppeling wordt tevens gebruikt om het inverse model te trainen.

Men heeft ontdekt dat gedurende een beweging waarbij we vertrouwen op ons tastzintuig, we die beweging kunnen corrigeren binnen ongeveer 50 ms (Weiss en Flanders, 2011). Dit suggereert dat niet alleen op het niveau van de hersenschors (cortex), maar ook op tussengelegen niveaus (subcorticaal en in het ruggenmerg) zintuiglijke terugkoppeling plaatsvindt. Op deze niveaus wordt de verwachte haptische terugkoppeling (verkregen door een efferente kopie) vergeleken de werkelijke haptische informatie (zie blokken C2 en C3 in figuur 8.3) om vervolgens het aansturingscommando bij te stellen. Tijdens voorwaartse koppeling bestaat er een risico op een opeenstapeling van fouten in het aansturingscommando als gevolg van ruis en onzekerheid, aangezien in dit geval alleen informatie uit het verleden beschikbaar is via het inverse model. Door het vergelijken van de werkelijke en de verwachte zintuiglijke informatie op verschillende niveaus in het centraal zenuwstelsel (blokken C1, C2 en C3), kan de huidige beweging op ieder tijdstip gevolgd en zo nodig worden bijgestuurd worden.

In hoofdstuk 2 lieten we zien dat ons visueel systeem voorspellingen gebruikt om het oog een bewegend doel te laten volgen. In hoofdstuk 6 en 7 onderzochten we of het somatosensorisch systeem over dezelfde eigenschappen beschikt. Daarom gebruikten we in **hoofdstuk 6** een experiment waarin proefpersonen hun wijsvinger in virtuele buizen rond moesten bewegen. Deze virtuele buizen hadden de vorm van een ellips en werden gemaakt door een robot die een kracht op de vingertop van de proefpersoon uitoefende zodra de vinger de wand van de buis raakte. In een aantal vormen was een gekromd deel van de buis vervangen door een recht deel. De proefpersoon kreeg in totaal 24 varianten van de ellips gepresenteerd en iedere variant werd vijf keer achter elkaar doorlopen. Proefpersonen presteerden beter wanneer hun vinger continu contact mocht houden met de wand van de buis, in plaats van wanneer hun vinger de wand niet mocht raken. Maar zelfs met deze continue haptische terugkoppeling konden proefpersonen niet exact inspelen op de overgang van een gekromd naar een recht deel van de buis. Net zoals voor het visueel systeem blijkt het voor het somatosensorisch systeem moeilijk te zijn om in te spelen op abrupte veranderingen.

In **hoofdstuk 7** testten we de mate waarin proefpersonen zintuiglijke terugkoppeling en voorspellingen over aankomende veranderingen in kromming combineerden. We gebruikten dezelfde robot als in hoofdstuk 6 om virtuele buizen te genereren. Deze buizen hadden de vorm van een ellips met een abrupt afgevlakt deel (zoals in hoofdstuk 6) of hadden de vorm van een Limaçon-figuur waarbij de kromming van de vorm continu veranderde. Vier van de zes proefpersonen anticipeerden de overgang van het gekromde naar het rechte deel van de ellips door langzamer te bewegen en door de kracht die werd uitgeoefend op de wand te verminderen. Dit was echter niet precies getimed met het moment waarop de overgang bereikt werd. De timing verbeterde niet naarmate de vorm vaker doorlopen werd. Ondanks de meer complexe vorm van de Limaçon-figuren varieerde de vingersnelheid volgens een vast patroon gerelateerd aan de kromming van de buis. Ook de manier waarop proefpersonen de kracht uitgeoefend op de wand aanpaste liet zien dat zij inspeelden op de aankomende veranderingen in kromming. Deze resultaten laten zien dat het moeilijk is om te anticiperen op een abrupte overgang in kromming, maar dat door middel van voorspellingen door het somatosensorisch systeem rekening kan worden gehouden met continue veranderingen in kromming.

Summary

This thesis aims at a better understanding of how the brain combines sensory feedback with feedforward predictions to guide movements. Therefore, we investigated human motor behavior when subjects were moving their finger along three-dimensional objects (chapter 2), were playing video a game (chapters 3 and 4), had to steer a randomly moving object to a target (chapter 5), or were touching surfaces of unknown objects (chapters 6 and 7). When making movements, the brain cannot solely rely on feedback from the sensory system, because this information is not up-to-date due to sensorimotor delays. In addition, the brain has to deal with noise in the neural system and uncertainty about the environment. In order to deal with these uncertainties, the brain combines sensory feedback with feedforward predictions. In chapter 2 we showed that during tracing of a complex three-dimensional path with the finger, a combination of saccades and vergence eye movements brings the eyes ahead of the finger to explore the upcoming trajectory. In chapter 3 we found that even smooth pursuit eye movements could be directed ahead of moving objects, instead of being driven by the movement of a visual target on the retina. In chapter 4 we modeled eye-hand coordination in an obstacle-avoidance task, taking into account observation noise of the hands and obstacles, as well as uncertainty about the locations of the objects. The model correctly predicted the order and location of fixations, and the hand trajectories. In chapter 5, we found that models optimizing the trade-off between effort and performance could not explain motor behavior under uncertainty in time-constrained tasks. We postulated a new model that also took into account the time-integrated position error of the movement. This model correctly predicted the observed movement trajectories for different levels of uncertainty. Chapters 6 and 7 showed that when subjects were moving their finger along an invisible surface, they could not anticipate abrupt changes in surface curvature. However, they could anticipate smooth changes in curvature using feedforward predictions of the somatosensory system. The next sections provide a detailed summary of chapters 2–7.

Chapter 2 – Visuomotor coordination is different for different directions in three-dimensional space

In chapter 2 we investigated visuomotor coordination in three dimensions. In most visuomotor tasks where subjects have to reach to visual targets or move the hand along a particular trajectory, eye movements have been shown to lead hand movements. Since the dynamics of vergence eye movements is different from that of smooth pursuit and saccades, we investigated the lead time of gaze relative to the hand for the depth component (vergence) and in the frontal plane (smooth pursuit and saccades) in a tracking task and in a tracing task where human subjects were instructed to move the finger along a 3D path. For tracking, gaze leads finger position on average by 28 ms (standard error (SE) 6 ms) for the components in the frontal plane, but lags finger position by 95 ms (SE 39 ms) for the depth dimension. For tracing, gaze leads finger position by 151 ms (SE 36 ms) for the depth dimension. For the frontal plane, the mean lead time of gaze relative to the hand is 287 ms (SE 13 ms). However, we found that the lead time in the frontal plane was inversely related to the tangential velocity of finger. This inverse relation for movements in the frontal plane could be explained by assuming that gaze leads the finger by a constant distance of about 2.6 cm (range 1.5–3.5 cm across subjects).

Chapter 3 – Gaze is driven by an internal goal trajectory in a visuomotor task

The tracing task described in the previous chapter demonstrates that when we make hand movements to visual targets, gaze usually leads hand position by a series of saccades to task-relevant locations. Recent research suggests that the slow smooth pursuit eye movement system may interact with the saccadic system in complex tasks. Increasing evidence demonstrates that the smooth pursuit system can receive non-retinal input. In chapter 3, we hypothesized that a combination of saccades and smooth pursuit guides the hand movements toward a goal in a complex environment, using an internal representation of future trajectories as input to the visuomotor system. This implies that smooth pursuit leads hand position, which is remarkable since the general idea is that smooth pursuit is driven by retinal slip. To test this hypothesis, we designed a video-game task in which human subjects used their thumbs to move two cursors to a common goal position while avoiding stationary obstacles. We found that gaze led the cursors by a series of saccades interleaved with ocular fixation or pursuit. Smooth pursuit was neither correlated with cursor position nor cursor velocity. Thus, a combination of fast and slow eye-movements, driven by an internal goal instead of a retinal goal, led the cursor movements. This might reflect a compromise between exploring future cursor paths and verifying that the cursors move along the desired paths.

Chapter 4 – A POMDP model of eye-hand coordination

In this chapter, we modeled eye-hand coordination in a task where an agent had to move two hands to a final common goal without hitting obstacles (the same task as described in chapter 3). The agent could perceive the scene (hands, obstacles and target) by making eye movements. The coupling between perception (the eye) and action (the hands) was achieved by modeling this system as a continuous-state partially-observable Markov decision process (POMDP) with a high-dimensional state space. The state update was subjected to Gaussian noise that varied among the elements of the scene (obstacles and target). The agent inferred the true state of the system based on stochastic observations of that state. The reliability of the observation of a hand, obstacle or target was dependent on the distance between the object and the eye, to mimic foveated vision. The agent's goal was to minimize the expected cumulative cost consisting of (1) a penalty if the hands did not reach the target, (2) a penalty if the hands hit an obstacle, and (3) the cost of moving the eye or hands. Minimizing the expected cost yielded an optimal motion pattern of the hands and the eye. Using the behavioral data presented in chapter 3, we found that for the majority of trials, the model correctly predicts the order and location of fixations, as well as the hand trajectories.

Chapter 5 – Time-integrated position error accounts for sensorimotor behavior in time-constrained tasks

Several studies have shown that human motor behavior can be successfully described using optimal control theory, which describes behavior by optimizing the trade-off between the subject's effort and performance. In this approach it is assumed that subjects reach the goal exactly at the final time. However, another strategy might be that subjects try to reach the target position well before the final time to avoid the risk of missing the target. To test this, we have investigated whether the standard model that minimizes the control effort and maximizes the performance is sufficient to describe human motor behavior in time-constrained motor tasks. We postulate a new model which includes an additional cost criterion which penalizes deviations of the effector relative to the target throughout the trial, forcing arrival on target before the final time. To investigate which model gives the best fit to the data and to see whether that model is generic, we tested both models in two different tasks where subjects used a joystick to steer a ball on a screen to hit a target (first task) or one of two targets (second task) before a final time. Noise of different amplitudes was superimposed on the ball position to investigate the ability of the models to predict motor behavior for different levels of uncertainty. The results show that a cost function representing only a trade-off between effort and accuracy at the end time is insufficient to describe the observed behavior. The new model correctly predicts that subjects steer the ball to the target position well before the final time is reached, which is in agreement with the observed behavior. This result is consistent for all noise amplitudes and for both tasks.

Chapter 6 – Somatosensory anticipation of curvature in a haptic virtual environment

Chapter 2 showed that the human visuomotor system uses predictive mechanisms to allow the eye to efficiently follow a moving target. The goal of chapters 6 and 7 was to determine whether the somatosensory system has similar capabilities as the visuomotor system. Therefore, we designed an experiment in which subjects used the right arm to move the index fingertip inside of virtual tubes, shaped as large elliptical objects positioned in the frontal plane. These virtual tubes were created by a robot that applied forces on the subject's fingertip when the fingertip touched the tube's surface. The virtual ellipses had three different aspect ratios and two different tilts. In 18 of the 24 ellipses, a curved section was replaced by a straight tubular segment, occurring at an early, middle or late phase of the movement. Each of the shapes was presented only once to each subject, but the subject explored each one by moving in five consecutive laps. Performance was more improved over the laps when subjects were allowed to stay in constant contact with the walls of the tube, rather than attempting to stay off the walls. However, even with this continuous haptic feedback, subjects could not precisely anticipate the transition from the curved section to the straight section of the tube. Thus, similarly to recent results for visually-guided eye movements, it appears that it is difficult for the haptic guidance system to anticipate abrupt changes in curvature.

Chapter 7 – Predictive mechanisms in the control of contour following

Haptic tracing is a form of active sensing, where the movement itself alters the sensory feedback. According to the literature on somatosensory guidance, the actual feedback may interact with a feedforward prediction of the anticipated feedback, to allow continuous updating. The experiment described in this chapter was designed to test the degree to which subjects combined ongoing feedback control with anticipation of upcoming changes in curvature of the surface. A position/force robot arm with a large three-dimensional workspace was attached to the index finger and was programmed to produce virtual surfaces with curvatures that varied within and across trials. With eyes closed, subjects moved the index fingertip within the lumen of virtual tubular shapes, pressing outward against the walls. The shapes were either elliptical hoops with abruptly flattened regions (similar shapes as in chapter 6) or rotated Limaçon shapes, where the surface curvature varied continuously. Four of the six subjects anticipated the corner of an abruptly flattened region by slowing down and/or decreasing contact force, but this was not precisely timed to the upcoming event and this tendency did not improve with learning. However, in spite of the more complex nature of the Limaçon shapes, which were presented with clockwise or counterclockwise rotations, and in various vertical planes, finger speed varied with curvature according to the two-thirds power law prediction. Modulation of contact force also indicated good anticipation of upcoming changes in curvature. The results demonstrate that, without vision, it is difficult to learn to anticipate the spatial location of an abrupt transition in curvature. But the results also suggest that smooth changes in curvature may be facilitated by feedforward predictions.

References

Abbeel P, Ng AY (2005) Exploration and apprenticeship learning in reinforcement learning. In *International Conference on Machine Learning (ICML)*, pp. 1–8

Admiraal MA, Keijsers NLW, Gielen CCAM (2003) Interaction Between Gaze and Pointing Toward Remembered Visual Targets. *J Neurophysiol* 90: 2136–2148

Admiraal MA, Kusters MJMAM, Gielen CCAM (2004) Modeling kinematics and dynamics of human arm movements. *Motor Control* 8: 312–338

Atkeson CG, Hollerbach JM (1985) Kinematic features of unrestrained vertical arm movements. *J Neurosci* 5: 2318–2330

Badler J, Lefèvre P, Missal M (2010) Causality attribution biases oculomotor responses. *J Neurosci* 30: 10517–10525

Barnes GR (2008) Cognitive processes involved in smooth pursuit eye movements. *Brain Cognition* 68: 309–326

Barnes GR, Hill T (1984) The influence of display characteristics on active pursuit and passively induced eye movements. *Exp Brain Res* 56: 438–447

Becker W, Fuchs AF (1985) Prediction in the oculomotor system: smooth pursuit during transient disappearance of a visual target. *Exp Brain Res* 57: 562–575

Bellman R (1957) *Dynamic Programming.* Princeton University Press, New Jersey

Biggs J, Horch K, Clark FJ (1999) Extrinsic muscles of the hand signal fingertip location more precisely than they signal the angles of individual finger joints. *Exp Brain Res* 125: 221–230

Blohm G, Missal M, Lefèvre P (2005) Direct evidence for a position input to the smooth pursuit system. *J Neurophysiol* 94: 712–721

Bluteau J, Coquillart S, Payan Y, Gentaz E (2008) Haptic guidance improves the visuo-manual tracking of trajectories. *PLoS ONE* 3: e1775

Borkar VS (2005) Controlled diffusion processes. *Probability Surveys* 2: 213–244

Bour LJ, van Gisbergen JA, Bruijns J, Ottes FP (1984) The double magnetic induction method for measuring eye movement–results in monkey and man. *IEEE Trans Biomed Eng* 31: 419–427

Braun DA, Aertsen A, Wolpert DM, Mehring C (2009a) Learning optima adaptation strategies in unpredictable motor tasks. *Journal Neurosci* 29: 6472–6478

Braun DA, Ortega PA, Wolpert DM, Friston KJ (2009b) Nash equilibria in multi-agent motor interactions. *PLoS Comput Biol* 5: e1000468

Bremen P, Van der Willigen RF, Van Opstal AJ (2007) Applying double magnetic induction to measure two-dimensional head-unrestrained gaze shifts in human subjects. *J Neurophysiol* 98: 3759–3769

Brooks A (2009) *Parametric POMDPs.* VDM Verlag

Brunskill E, Kaelbling L, Lozano-Perez T, Roy N (2008) Continuous-state POMDPs with hybrid dynamics. In *Tenth International Symposium on Artificial Intelligence and Mathematics (ISAIM)*

Carpenter RHS (1988) *Movements of the eyes (2nd edition).* Pion Limited

Challis JH (1995) A procedure for determining rigid body transformation parameters. *J Biomech* 28: 733–737

Chaturvedi V, Van Gisbergen JAM (1998) Shared target selection for combined version-vergence eye movements. *J Neurophysiol* 80: 849–862

Chen-Harris H, Joiner WM, Ethier V, Zee DS, Shadmehr R (2008) Adaptive control of saccades via internal feedback. *J Neurosci* 28: 2804–2813

Chhabra M, Jacobs RA (2006) Near-optimal human adaptive control across different noise environments. *J Neurosci* 26: 10883–10887

Collewijn H, Erkelens CJ, Steinman RM (1997) Trajectories of the human binocular fixation point during conjugate and non-conjugate gaze-shifts. *Vision Res* 37: 1049–1069

Collewijn H, Tamminga EP (1984) Human smooth and saccadic eye movements during voluntary pursuit of different target motions on different backgrounds. *J Physiol* 351: 217–250

Crapse TB, Sommer MA (2008) Corollary discharge across the animal kingdom. *Nat Rev Neurosci* 9: 587–600

Cumming BG, DeAngelis GC (2001) The physiology of stereopsis. *Annu Rev Neurosci* 24: 203–238

Day BL, Lyon IN (2000) Voluntary modification of automatic arm movements evoked by motion of a visual target. *Exp Brain Res* 130: 159–168

De Brouwer S, Missal M, Barnes G, Lefèvre P (2002) Quantitative analysis of catch-up saccades during sustained pursuit. *J Neurophysiol* 87: 1772–1780

De Hemptinne C, Lefèvre P, Missal M (2008) Neuronal bases of directional expectation and anticipatory pursuit. *J Neurosci* 28: 4298–4310

DeAngelis GC (2000) Seeing in three dimensions: the neurophysiology of stereopsis. *Trends Cogn Sci* 4: 80–90

Diedrichsen J (2007) Optimal task-dependent changes of bimanual feedback control and adaptation. *Curr Biol* 17: 1675–1679

Duhamel JR, Colby CL, Goldberg ME (1992) The updating of the representation of visual space in parietal cortex by intended eye movements. *Science* 255: 90–92

Ehrich JM, Flanders M, Soechting JF (2008) Factors influencing haptic perception of complex shapes. *IEEE T Haptics* 1: 19–26

Engel KC, Soechting JF (2003) Interactions between ocular motor and manual responses during two-dimensional tracking. *Prog Brain Res* 142: 141–153

Erez T, Smart WD (2010) A scalable method for solving high-dimensional continuous POMDPs using local approximation. In *Proceedings of the 26th Conference in Uncertainty in Artificial Intelligence (UAI)*

Erkelens CJ, van der Steen J, Steinman RM, Collewijn H (1989) Ocular vergence under natural conditions. I. Continuous changes of target distance along the median plane. *Proc R Soc London B* 236: 417–440

Essig K, Pomplun M, Ritter H (2006) A neural network for 3D gaze recording with binocular eye trackers. *Int J Parallel Emergent Distributed Syst* 21: 79–95

Faisal AA, Selen LPJ, Wolpert DM (2008) Noise in the nervous system. *Nat Rev Neurosci* 9: 292–303

Flanagan JR, Johansson RS (2003) Action plans used in action observation. *Nature* 424: 769–771

Flanders M, Tillery SIH, Soechting JF (1992) Early stages in a sensorimotor transformation. *Behav Brain Sci* 15: 309–320

Fleming WH (2006) Risk sensitive stochastic control and differential games. *Commun Inf Syst* 6: 161–178

Franklin DW, Wolpert DM (2008) Specificity of reflex adaptation for task-relevant variability. *J Neurosci* 28: 14165–14175

Franklin DW, Wolpert DM (2011) Computational mechanisms of sensorimotor control. *Neuron* 72: 425–442

Frens MA, Van der Geest JN (2002) Scleral search coils influence saccade dynamics. *J neurophysiol* 88: 692–698

Friedburg C, Allen CP, Mason PJ, Lamb TD (2004) Contribution of cone photoreceptors and post-receptoral mechanisms to the human photopic electroretinogram. *J Physiol* 556: 819–834

Fuchs AF (1967) Saccadic and smooth pursuit eye movements in the monkey. *J Physiol* 3: 609–631

Gardner JL, Lisberger SG (2001) Linked target selection for saccadic and smooth pursuit eye movements. *J Neurosci* 21: 2075–2084

Ghez C, Favilla M, Ghilardi MF, Gordon J, Bermejo R, Pullman S (1997) Discrete and continuous planning of hand movements and isometric force trajectories. *Exp Brain Res* 90: 217–233

Gielen CCAM, Dijkstra TMH, Roozen IJ, Welten J (2009) Coordination of gaze and hand movements for tracking and tracing in 3D. *Cortex* 45: 340–355

Gonzalez F, Rivadulla C, Perez R, Cadarso C (1998) Depth perception in random dot stereograms is not affected by changes in either vergence or accomodation. *Optom Vis Sci* 75: 743–747

Goossens HHLM, Van Opstal AJ (1997) Human eye-head coordination in two dimensions under different sensorimotor conditions. *Exp Brain Res* 114: 542–560

Harris CM, Wolpert DM (1998) Signal-dependent noise determines motor planning. *Nature* 394: 780–784

Hayhoe MM, Shrivastava A, Mruczek R, Pelz JB (2003) Visual memory and motor planning in a natural task. *J Vision* 3: 49–63

Henriques DY, Klier EM, Smith MA, Lowy D, Crawford JD (1998) Gaze-centered remapping of remembered visual space in an open-loop pointing task. *J Neurosci* 18: 1583–1594

Henriques DYP, Soechting JF (2003) Bias and sensitivity in the haptic perception of geometry. *Exp Brain Res* 150: 95–108

Henriques DYP, Soechting JF (2005) Approaches to the study of haptic sensing. *J Neurophysiol* 93: 3036–3043

Hermens F, Gielen CCAM (2003) Visual and haptic matching of perceived orientations of lines. *Perception* 32: 235–248

Horev G, Saig A, Knutsen PM, Pietr M, Yu C, Ahissar E (2011) Motor-sensory convergence in object localization: a comparative study in rats and humans. *Philos T R Soc B* 366: 3070–3076

Izawa J, Rane T, Donchin O, Shadmehr R (2008) Motor adaptation as a process of reoptimization. *J Neurosci* 28: 2883–2891

Jenkins GM, Watts DG (1968) *Spectral Analysis and its Applications.* Holden-Day, San Francisco

Johansson RS, Flanagan JR (2009) Coding and use of tactile signals from the fingertips in object manipulation tasks. *Nat Rev Neurosci* 10: 345–359

Jones KE, Hamilton AFC, Wolpert DM (2002) Sources of signal-dependent noise during isometric force production. *J Neurophysiol* 88: 1533–1544

Kaelbling LP, Littman ML, Cassandra AR (1998) Planning and acting in partially observable stochastic domains. *Artif Intell* 101: 99–134

Kappen HJ (2005a) Linear theory for control of nonlinear stochastic systems. *Phys Rev Lett* 95: 200201

Kappen HJ (2005b) Path integrals and symmetry breaking for optimal control theory. *J Stat Mech-Theory E* 2005: P11011

Kappers AML, Koenderink JJ (1999) Haptic perception of spatial relations. *Perception* 28: 781–796

Karatzas I, Shreve SE (2000) *Brownian motion and stochastic calculus.* Springer

Keller EL, Missal M (2003) Shared brainstem pathways for saccades and smooth-pursuit eye movements. *Ann N Y Acad Sci* 1004: 29–39

Khan AZ, Lefèvre P, Heinen SJ, Blohm G (2010) The default allocation of attention is broadly ahead of smooth pursuit. *J Vision* 10: 7

Klein Breteler MD, Hondzinski JM, Flanders M (2003) Drawing sequences of segments in 3D: kinetic influences on arm configuration. *J Neurophysiol* 89: 3253–3263

Koch C, Ullman S (1985) Shifts in selective visual attention: towards the underlying neural circuitry. *Hum Neurobiol* 4: 219–227

Körding K (2007) Decision theory: what "should" the nervous system do? *Science* 318: 606–610

Körding KP, Wolpert DM (2004) The loss function of sensorimotor learning. *P Natl Acad Sci USA* 101: 9839–9842

Kowler E (1989) Cognitive expectations, not habits, control anticipatory smooth oculomotor pursuit. *Vision Res* 29: 1049–1057

Kowler E (1990) The role of visual and cognitive processes in the control of eye movements. in kowler, e. (ed.). *Eye movements and their role in visual and cognitive processes.* Elsevier. Amsterdam: pp. 1–70

Kowler E, Martins AJ, Pavel M (1984) The effect of expectations on slow oculomotor control–IV. anticipatory smooth eye movements depend on prior target motions. *Vision Res* 24: 197–210

Kowler E, Steinman RM (1979a) The effect of expectations on slow oculomotor control–I. Periodic target steps. *Vision Res* 19: 619–632

Kowler E, Steinman RM (1979b) The effect of expectations on slow oculomotor control–II. Single target displacements. *Vision Res* 19: 633–646

Krauzlis RJ (2004) Recasting the smooth pursuit eye movement system. *J Neurophysiol* 91: 591–603

Krauzlis RJ, Lisberger SG (1994) A model of visually-guided smooth pursuit eye movements based on behavioral observations. *J Comput Neurosci* 1: 265–283

Lacquaniti F, Terzuolo C, Viviani P (1983) The law relating the kinematic and figural aspects of drawing movements. *Acta Psychol* 54: 115–130

Land M, Mennie N, Rusted J (1999) The roles of vision and eye movements in the control of activities of daily living. *Perception* 28: 1311–1328

Land MF (2006) Eye movements and the control of actions in everyday life. *Prog Retin Eye Res* 25: 296–324

Land MF, Lee DN (1994) Where we look when we steer. *Nature* 369: 742–744

Lazzari S, Vercher JL, Buizza A (1997) Manuo-ocular coordination in target tracking. I. A model simulating human performance. *Biol Cybern* 77: 257–266

Lederman SJ, Klatzky RL (1987) Hand movements: a window into haptic object recognition. *Cognitive psychol* 19: 342–368

Lisberger SG (1998) Postsaccadic enhancement of initiation of smooth pursuit eye movements in monkeys. *J Neurophysi* 79: 1918–1930

Lisberger SG (2010) Visual guidance of smooth-pursuit eye movements: sensation, action, and what happens in between. *Neuron* 66: 477–491

Lisberger SG, Morris EJ, Tychsen L (1987) Visual motion processing and sensory-motor integration for smooth pursuit eye movements. *Annual Rev Neurosci* 10: 97–129

Liu D, Todorov E (2007) Evidence for the flexible sensorimotor strategies predicted by optimal feedback control. *J Neurosci* 27: 9354–9368

McKee SP, Nakayama K (1984) The detection of motion in the peripheral visual field. *Vision Res* 24: 25–32

Meyer CH, Lasker AG, Robinson DA (1985) The upper limit of human smooth pursuit velocity. *Vision Res* 25: 561–563

Miller SA, Harris ZA, Chong EKP (2009) A POMDP framework for coordinated guidance of autonomous uavs for multitarget tracking. *EURASIP J Adv Signal Processing* 2009: 1–17

Mrotek LA, Gielen CCAM, Flanders M (2006) Manual tracking in three dimensions. *Exp Brain Res* 171: 99–115

Mrotek LA, Soechting JF (2007) Predicting curvilinear target motion through an occlusion. *Exp Brain Res* 178: 99–114

Nagengast AJ, Braun DA, Wolpert DM (2009) Optimal control predicts human performance on objects with internal degrees of freedom. *PLoS Comput Biol* 5: e1000419

Nagengast AJ, Braun DA, Wolpert DM (2011) Risk sensitivity in a motor task with speed-accuracy trade-off. *J Neurophysiol* 105: 2668–2674

Nagengast AJ, Braun DA, Wolpert DM, Diedrichsen J (2010) Risk-sensitive optimal feedback control accounts for sensorimotor behavior under uncertainty. *PLoS Comput Biol* 6: e1000857

Neggers SFW, Bekkering H (2000) Ocular gaze is anchored to the target of an ongoing pointing movement. *J Neurophysiol* 83: 639–651

Neggers SFW, Bekkering H (2001) Gaze anchoring to a pointing target is present during the entire pointing movement and is driven by a non-visual signal. *J Neurophysiol* 86: 961–970

Nyström M, Holmqvist K (2010) An adaptive algorithm for fixation, saccade, and glissade detection in eye-tracking data. *Behav Res Methods* 42: 188–204

Orban de Xivry JJ, Missal M, Lefèvre P (2008) A dynamic representation of target motion drives predictive smooth pursuit during target blanking. *J Vision* 8: 6

Peters RJ, Itti L (2008) Applying computational tools to predict gaze direction in interactive visual environments. *ACM Transactions on Applied Perception* 5: 1–19

Porta JM, Vlassis N, Spaan MTJ, Poupart P (2006) Point-based value iteration for continuous POMDPs. *J Mach Learn Res* 7: 2329–2367

Prentice S, Roy N (2009) The belief roadmap: Efficient planning in belief space by factoring the covariance. *Int J Robot Res* 28: 1448–1465

Prescott TJ, Diamond ME, Wing AM (2011) Active touch sensing. *Philos T R Soc B* 366: 2989–2995

Purves D, Augustine GJ, Fitzpatrick D, Hall WC, Lamantia AS, McNamara JO, Williams SM (2004) *Neuroscience.* Sinauer Associates Inc

Reilink R, Stramigioli S, Kappers AML, Misra S (2011) Evaluation of flexible endoscope steering using haptic guidance. *Int J Med Robot Comp* 7: 178–186

Reina GA, Schwartz AB (2003) Eye-hand coupling during closed-loop drawing: Evidence of shared motor planning? *Hum Movement Sci* 22: 137–152

Rincon-Gonzalez L, Buneo CA, Tillery SIH (2011) The proprioceptive map of the arm is systematic and stable, but idiosyncratic. *PloS ONE* 6: e25214

Rosenbaum DA, Dawson AM, Challis JH (2006) Haptic tracking permits bimanual independence. *J Exp Psychol* 32: 1266–1275

Rothkopf CA, Ballard DH, Hayhoe MM (2007) Task and context determine where you look. *J Vision* 7: 16

Sailer U, Eggert T, Ditterich J, Straube A (2000) Spatial and temporal aspects of eye-hand coordination across different tasks. *Exp Brain Res* 134: 163–173

Sailer U, Flanagan JR, Johansson RS (2005) Eye-hand coordination during learning of a novel visuomotor task. *J Neurosci* 25: 8833–8842

Saunders JA, Knill DC (2004) Visual feedback control of hand movements. *J Neurosci* 24: 3223–3234

Scarchilli K, Vercher JL, Gauthier GM, Cole J (1999) Does the oculo-manual co-ordination control system use an internal model of the arm dynamics? *Neurosci Lett* 265: 139–142

Scott SH (2004) Optimal feedback control and the neural basis of volitional motor control. *Nat Rev Neurosci* 5: 532–546

Scott SH, Loeb GE (1994) The computation of position sense from spindles in mono-and multiarticular muscles. *J Neurosci* 14: 7529–7540

Sims CR, Jacobs RA, Knill DC (2011) Adaptive allocation of vision under competing task demands. *J Neurosci* 31: 928–943

Smit AC, Van Gisbergen JAM, Cools AR (1987) A parametric analysis of human saccades in different experimental paradigms. *Vision Res* 27: 1745–1762

Smith AM, Gosselin G, Houde B (2002) Deployment of fingertip forces in tactile exploration. *Exp Brain Res* 147: 209–218

Soechting J, Flanders M (2011) Multiple factors underlying haptic perception of length and orientation. *IEEE T Haptics* 4: 263–272

Soechting JF, Rao HM, Juveli JZ (2010) Incorporating prediction in models for two-dimensional smooth pursuit. *PLoS ONE* 5: e12574

Soechting JF, Song W, Flanders M (2006) Haptic feature extraction. *Cerebral Cortex* 16: 1168–1180

Sondik EJ (1971) The optimal control of partially observable Markov processes. Ph.D. diss., Stanford

Stengel RF (1994) *Optimal Control and Estimation.* Dover Publications

Tassa Y, Erez T, Smart WD (2008) Receding horizon differential dynamic programming. In *Advances in Neural Information Processing Systems (NIPS)*, Vol. 20. MIT Press, Cambridge, MA

Thorpe S, Fize D, Marlot C (1996) Speed of processing in the human visual system. *Nature* 381: 520–522

Todorov E (2004) Optimality principles in sensorimotor control. *Nat Neurosci* 7: 907–915

Todorov E, Jordan MI (2002) Optimal feedback control as a theory of motor coordination. *Nat Neurosci* 5: 1226–1235

Tramper JJ, Gielen CCAM (2011) Visuomotor coordination is different for different directions in three-dimensional space. *J Neurosci* 31: 7857–7866

Tramper JJ, Lamont A, Flanders M, Gielen CCAM (2013) Gaze is driven by an internal goal trajectory in a visuomotor task. *Eur J Neurosci* p. In press

Tramper JJ, Stephens S, Flanders M (2012) Somatosensory anticipation of curvature in a haptic virtual environment In *Proceedings of the Haptics Symposium*, pp. 183–186. IEEE

Van den Broek B, Wiegerinck W, Kappen HJ (2010) Risk sensitive path integral control. *Proc UAI-10* pp. 615–622

Van Pelt S, Medendorp PW (2008) Updating Target Distance Across Eye Movements in Depth. *J Neurophysiol* 99: 2281–2290

Vercher JL, Quaccia D, Gauthier GM (1995) Oculo-manual coordination control: respective role of visual and non-visual information in ocular tracking of self-moved targets. *Exp Brain Res* 103: 311–322

Vindras P, Desmurget M, Viviani P (2005) Error parsing in visuomotor pointing reveals independent processing of amplitude and direction. *J Neurophysiol* 94: 1212–1224

Vinter R (2010) *Optimal control.* Springer

Viviani P, Terzuolo C (1982) Trajectory determines movement dynamics. *Neuroscience* 7: 431–437

Walter J, Ritter H (1995) Local PSOMs and Chebyshev PSOMs—improving the parametrised self-organizing maps. *Proc Int Conf Artificial Neural Networks (ICANN-95), Paris* 1: 95–102

Weiss EJ, Flanders M (2011) Somatosensory comparison during haptic tracing. *Cereb Cortex* 21: 425–434

White JA, Rubinstein JT, Kay AR (2000) Channel noise in neurons. *Trends Neurosci* 23: 131–137

Whittaker SG, Eaholtz G (1982) Learning patterns of eye motion for foveal pursuit. *Invest Ophth Vis Sci* 23: 393–397

Winges SA, Soechting JF (2011) Spatial and temporal aspects of cognitive influences on smooth pursuit. *Exp Brain Res* 211: 27–36

Wolpert DM, Ghahramani Z (2000) Computational principles of movement neuroscience. *Nat Neurosci* 3: 1212–1217

Wolpert DM, Ghahramani Z, Jordan MI (1995) An internal model for sensorimotor integration. *Science* 269: 1880–1882

Wolpert DM, Miall RC, Kawato M (1998) Internal models in the cerebellum. *Trends Cogn Sci* 2: 338–347

Yang J, Lee J, Lisberger SG (2012) The interaction of bayesian priors and sensory data and its neural circuit implementation in visually guided movement. *J Neurosci* 32: 17632–17645

Dankwoord

De kiem voor mijn proefschrift werd gelegd in de zomer van 2008, toen ik mijn stage bij Magteld en Stan aan het afronden was. Toen Stan vroeg of ik interesse had om als promovendus onderzoek te doen naar oog-handcoördinatie hoefde ik niet lang na te denken, en dus startte ik in september 2008 aan deze nieuwe uitdaging.

Ik wil beginnen met het bedanken van mijn promotor Stan Gielen. Stan, dat ik mijn proefschrift in vier jaar heb kunnen afronden is voor een groot deel ook jouw verdienste. Ondanks je drukke baan als hoofd van de afdeling, en later als decaan, wist je altijd op korte termijn tijd vrij te maken om me te helpen. Ik herinner me zelfs nog dat we een keer samen achter de computer hebben gezeten om een Matlab-probleem op te lossen. Ook stimuleerde je mij om mijn blikveld te verruimen door de samenwerking te zoeken met internationale wetenschappers, waaronder Tom Erez en Martha Flanders. Doordat jij me in contact heb gebracht met Martha heb ik een deel van mijn onderzoek in de Verenigde Staten kunnen uitvoeren, iets wat een heel belangrijke ervaring voor me is geweest.

Martha, I am really thankful that you gave me the opportunity to work in your lab. It was a great pleasure to collaborate with you. The experiments with the Phantom robot resulted in two publications (chapters 6 and 7) and your knowledge was essential for interpreting the results of the video-game experiment (chapter 3). I also admire your generosity and hospitality. You showed me your own neighborhood and you took me out for breakfast, lunch or diner. Stephen, I would like to thank you for programming the Phantom robot and your help with analyzing the data. Luckily, Martha convinced me not to visit Minneapolis during winter. The spring and summer months were perfect for exploring the city using your bike. Tom Erez, although we did not meet each other in real life, you were a nice and reliable person to work with.

Maaike en Denise, als kamergenoten van het eerste uur hebben jullie er mede voor gezorgd dat ik een super leuke tijd bij Biofysica heb gehad. Maaike, de manier waarop je je drukke baan als onderzoeker combineerde met een ongekende reeks aan outdooractiviteiten was indrukwekkend. Er ging geen weekend voorbij of je was weer wezen mountainbiken, racefietsen, klimmen of hardlopen. Denise, in de drie jaar dat we kamergenoten zijn geweest hebben we enorm veel lol gehad, zo erg zelfs dat er weleens iemand is komen kijken waar al dat geschater toch vandaan kwam. Ook kon ik altijd een gesprek met je aanknopen, zelfs al had je je koptelefoon op (iets wat bij onderzoekers zoveel betekent als: "niet storen, ik ben aan het werk"). Ik vind het fijn dat je een van mijn paranimfen wil zijn en wil je bedanken voor het beantwoorden van een stortvloed aan vragen die ik zo nu en dan had.

Elvis, sinds Denise weg is, heb ik de verzorging overgenomen. Het spijt me dat je niet meer op gezette tijden eten hebt gekregen, en je af en toe niet meer naar buiten kon kijken. Ik waardeer dan ook je doorzettingsvermogen en beloof beterschap. Dat is makkelijk gezegd, aangezien ik het stokje voor de verzorging heb overgedragen aan Marieke. Joris en Douwe, het laatste jaar van mijn promotie deelde ik de kamer met jullie. Jullie waren echt de perfecte opvolgers van Maaike en Denise en ik kon het erg goed met jullie vinden. Dat geldt zeker ook voor alle andere collega's. Magteld, ook al was je niet inhoudelijk bij mijn onderzoek betrokken, we praatten elkaar regelmatig bij en voorzag mij van advies. Joke, David en Lidwien, de afgelopen paar jaar behoorden jullie toch wel tot de harde kern van collega's waarmee ik samen ging lunchen. Het weer zorgde soms voor een dilemma: bij mooi weer wilden we graag buiten zitten, maar dan konden we geen tosti's bakken. Ook wil ik Artem, Josien, Jurrian, Tom, Marc, Rob, Peter, Yoolla, Martijn, Linsey, Moniek, Laurens, Rembrandt, Sep, Mohammad, Vicenç, Alberto, Patrick, Kevin, Willem, Bart en Atthaphon bedanken voor de gezelligheid op de afdeling en tijdens het jaarlijkse uitje.

Arjan, Cerien, Annet, Judith en Marieke, wat was het toch fijn om jullie als ondersteuning te hebben. Dit geldt zeker ook voor John! Ik heb vaak bij jullie de deur platgelopen voor een handtekening of de meest uiteenlopende vragen. Ger, Hans, Günter, Stijn en Perry, jullie stonden altijd klaar voor technische assistentie. Bart, Wim en Bert, jullie zijn nauwe betrokken geweest bij de theoretische onderbouwing van de experimenten uit hoofdstuk 5 en ik wil jullie bedanken voor de fijne samenwerking.

Voor een deel van mijn onderzoek heb ik hulp gehad van studenten. Guy en Christiaan, dankzij jullie pilot-experimenten is er uiteindelijk een mooi artikel verschenen (hoofdstuk 5). Bart, ik herinner me nog dat ik blij verrast was toen je tijdens mijn afwezigheid de opstelling had uitgebreid, proefpersonen had gezocht, metingen had gedaan, en zelfs de data al had geanalyseerd. Andres, ik heb dankbaar gebruik gemaakt van je programmeervaardigheden voor het maken van de 3D stimuli en dankzij jou hebben we een goede kalibratiemethode (PSOM) kunnen gebruiken voor kalibreren van de 3D oogpositie. Je hebt erg veel werk verzet wat is terug te vinden in drie hoofdstukken van mijn proefschrift (hoofdstuk 2, 3 en 4).

Ik hou erg van reizen en mijn promotietijd zal dan ook onlosmakelijk verbonden blijven met de meest fantastische reizen die ik in die periode heb gemaakt. Marit, met jou ben ik in maart 2009 naar Curaçao geweest. Het was een fantastische week en je was een prima buddy om samen te leren duiken. We hebben toen ook geleerd dat als je moet lachen onderwater, je duikbril volloopt. Frank en Mike, sinds onze road trip door Canada gaan we regelmatig samen op reis en we beleven keer op keer weer hilarische momenten samen, zoals bijvoorbeeld op een nacht in een Sloveens hostel (alle waarschuwingen van de Lonely Planet ten spijt). In 2010 reisde ik af naar San Diego voor de jaarlijkse Neuroscience meeting. Marloes, ik herinner me nog je verontschuldigingen voor het toch wat twijfelachtige hotel dat je had uitgezocht en dit was dan ook mijn eerste kennismaking met het fenomeen "bed bugs". Ach ja, het was in ieder geval lekker goedkoop en dan kon je van een van onze etentjes niet zeggen (ik vond het ook al zo gek dat de prijs van het dagmenu niet vermeld stond).

Ontspanning was er volop tijdens talloze activiteiten met vrienden, zoals de mannenavond-BBQ met Paul, Hein en Martijn, waarbij niet alleen de kooltjes in de fik stonden; het wekelijkse PhG-diner met Rianne, Marit, Lotte, Paul, Suzan, en later ook de kleine Joris; k(l)aasfonduen met Lotte, Lisette en Marieke van dispuut R.O.O.D.; een fotowedstrijd winnen met Jelka; carnavallen met Koen, Jerry, Mike en Frank; de etentjes met Ivo, Marloes en Judith L; de vele hardloop- en mountainbikerondjes door de bossen bij Westerhelling met Erik; een dagje dierentuin met Monica en Selmar; en natuurlijk de vele uren muziekplezier bij Philharmonie Gelre. Judith F, dankzij jou heb ik het sleeën als een van de winterse activiteiten geherintroduceerd. Mijke, we kennen elkaar al vanaf de peuterspeelzaal in Stros en dit levert keer op keer weer lachwekkende herinneringen op over onze basisschooltijd. We gaan vast en zeker nog veel leuke uitstapjes maken en wie weet belanden we ooit wel weer op de daverende kermis van Franeker.

Sumientra, vaak spraken we voor slechts een half uurtje af om te lunchen en ineens bleek het dan toch laat in de middag te zijn. Het was super fijn om op jou terug te kunnen vallen voor een serieus gesprek of om gewoon lekker te kletsen. Ook hebben we samen een poging gedaan om ons C++ eigen te maken. De opdracht “Hello World.” wilde nog wel lukken, maar al snel daarna raakten we verzand in de C++-terminologie (“If we are deleted before other, we will delete _arr = other._arr, which is not owned by us: other._arr will point to garbage and will attempt to delete array again. You die.”). Gelukkig gebruikte Thom wel begrijpelijke taal en konden we na een helder mini-college weer verder. Ik heb veel aan je gehad en heel erg bedankt dat jij een van mijn paranimfen wilt zijn.

Pap en mam, wat was het af en toe lekker om Nijmegen te verruilen voor de Zeeuwse kust en natuurlijk bedankt voor de ondersteuning tijdens mijn studie en promotie, en jullie hulp bij al die verhuizingen. Judith, Floris en de kids, het is altijd leuk om bij jullie op bezoek te komen en om lekker naar het strand te gaan. Maurice, wat is het fijn om het zo goed met iemand te kunnen vinden. Met jou beleef ik de meest gekke dingen en kom ik op de meest fantastische plekken. Onze fenomenale road trips door de VS smaakten naar meer. Door samen met jou de wereld over reizen is er een droom uitgekomen!

Curriculum Vitae

Julian Tramper was born on June 26, 1983 in Veere, the Netherlands. After high school graduation he started to study Mechanical Engineering at the Eindhoven University of Technology. After he obtained his propaedeutic degree, he decided to move to the Radboud University Nijmegen to study Natural Sciences. After obtaining his bachelor's degree in 2005, he enrolled in the international master program Transnational Ecosystem-based Water Management at the University of Duisburg-Essen and the master Environmental Sciences at the Radboud University. He graduated in 2007 with a study to the influence of metal contamination to floodplain wildlife. Since his broad scientific interest, he decided to shift his focus to the field of neuroscience by starting an internship at the department of Biophysics of the Radboud University. Here, he investigated the communication between two groups of neurons using model simulations, resulting in a master's degree of Natural Sciences in August 2008. He continued working at the same department, part of the Donders Institute of Brain, Cognition and Behaviour, as a PhD student under supervision of prof. Stan Gielen. During the last two years of his research project, he collaborated with prof. Martha Flanders from the University of Minnesota.

Julian Tramper werd geboren op 26 juni 1983 in Veere. Na het behalen van zijn VWO-diploma begon hij in 2001 aan de opleiding Werktuigbouwkunde aan de Technische Universiteit Eindhoven. Na het behalen van de propedeuse besloot hij Natuurwetenschappen te studeren aan de Radboud Universiteit Nijmegen. In 2005 behaalde hij zijn Bachelordiploma en koos hij voor het volgen van de internationale master Transnational Ecosystem-based Water Management aan de Universitt Duisburg-Essen en de master Environmental Sciences aan de Radboud Universiteit. In 2007 studeerde hij af op een onderzoek naar de risico's van metaalverontreiniging voor dieren in uiterwaarden. Tijdens zijn afstudeeronderzoek groeide de ambitie om verder te gaan in het wetenschappelijk onderzoek. Gezien zijn brede interesse besloot hij zich te oriënteren op de neurowetenschappen door een stage te lopen bij de afdeling Biofysica aan de Radboud Universiteit. Hier onderzocht hij de communicatie tussen groepen neuronen met behulp van modelsimulaties. Dit onderzoek resulteerde in het behalen van de master Natuurwetenschappen in 2008. Aansluitend is hij bij dezelfde afdeling, onderdeel van het Donders Institute for Brain, Cognition and Behaviour, gestart als promovendus onder leiding van prof. Stan Gielen. Tijdens zijn laatste twee jaar van zijn promotie heeft hij samengewerkt met prof. Martha Flanders van de University of Minnesota.

Publications

Tramper JJ, Flanders M (2013) Predictive mechanisms in the control of contour following. Accepted for publication in *Experimental Brain Research*.

Tramper JJ, Lamont A, Flanders M, Gielen CCAM (2012) Gaze is driven by an internal goal trajectory in a visuomotor task. *European Journal of Neuroscience*, doi: 10.1111/ejn.12107.

Tramper JJ, Van den Broek LJ, Wiegerinck W, Kappen HJ, Gielen CCAM (2012) Time-integrated position error accounts for sensorimotor behavior in time-constrained tasks. *PloS ONE* 7 (3), e33724.

Tramper JJ, Stephens S, Flanders M (2012) Somatosensory anticipation of curvature in a Haptic virtual environment. In *Proceedings of the IEEE Haptics Symposium*, pp. 183–186.

Erez T, **Tramper JJ**, Smart WD, Gielen CCAM (2011) A POMP model of eye-hand coordination. in *Proceedings of the Twenty-Fifth AAAI Conference on Artificial Intelligence*.

Tramper JJ, Gielen CCAM (2011) Visuomotor coordination is different for different directions in three-dimensional space. *The Journal of Neuroscience* 31 (21): 7857-7866.

Tramper JJ, Kappen HJ, Gielen CCAM (2009) Predicting human motor performance using stochastic optimal control. In *Proceedings of the Annual Symposium Advances in Computational Motor Control* 6.

Loos M, Ragas AMJ, **Tramper JJ**, Hendriks AJ (2009) Modeling zinc regulation in small mammals. *Environmental Toxicology and Chemistry* 28: 2378-2385.

Conferences

Tramper JJ, Stephens S, Flanders M (2012) Somatosensory anticipation of curvature in a Haptic virtual environment. Oral presentation. IEEE Haptics Symposium (HAPTICS 2012). Vancouver, Canada.

Tramper JJ, Van den Broek, LJ, Wiegerinck WAJJ, Kappen HJ, Gielen CCAM (2011) Predicting human motor behavior in various motor tasks with uncertainty using optimal control theory. Poster. Progress in Motor Control (PMC 2011). Cincinnati, USA.

Tramper JJ, Gielen CCAM (2010) Visuomotor coordination is different for different directions in 3D space. Poster. Society for Neuroscience Annual Meeting (SfN 2010). San Diego, USA.

Tramper JJ, Van den Broek, LJ, Wiegerinck WAJJ, Kappen HJ, Gielen CCAM (2010) Predicting human motor behavior under uncertainty using optimal control. Poster. Society for Neuroscience Annual Meeting (SfN 2010). San Diego, USA.

Tramper JJ, Van den Broek LJ, Kappen HJ, Gielen CCAM (2010) Predicting sensorimotor behaviour under uncertainty using stochastic optimal control. Poster. Forum of European Neuroscience (FENS 2010). Amsterdam, The Netherlands.

Tramper JJ, Gielen CCAM (2009) Dynamics of eye-hand coordination in 3D. Poster. Progress in Motor Control (PMC 2009). Marseille, France.

Donders Graduate School for Cognitive Neuroscience Series

1. van Aalderen-Smeets, S.I. (2007). *Neural dynamics of visual selection.* Maastricht University, Maastricht, the Netherlands.
2. Schoffelen, J.M. (2007). *Neuronal communication through coherence in the human motor system.* Radboud University Nijmegen, Nijmegen, the Netherlands.
3. de Lange, F.P. (2008). *Neural mechanisms of motor imagery.* Radboud University Nijmegen, Nijmegen, the Netherlands.
4. Grol, M.J. (2008). *Parieto-frontal circuitry in visuomotor control.* Utrecht University, Utrecht, the Netherlands.
5. Bauer, M. (2008). *Functional roles of rhythmic neuronal activity in the human visual and somatosensory system.* Radboud University Nijmegen, Nijmegen, the Netherlands.
6. Mazaheri, A. (2008). *The influence of ongoing oscillatory brain activity on evoked responses and behaviour.* Radboud University Nijmegen, Nijmegen, the Netherlands.
7. Hooijmans, C.R. (2008). *Impact of nutritional lipids and vascular factors in Alzheimers Disease.* Radboud University Nijmegen, Nijmegen, the Netherlands.
8. Gaszner, B. (2008). *Plastic responses to stress by the rodent urocortinergic Edinger-Westphal nucleus.* Radboud University Nijmegen, Nijmegen, the Netherlands.
9. Willems, R.M. (2009). *Neural reflections of meaning in gesture, language and action.* Radboud University Nijmegen, Nijmegen, the Netherlands.
10. van Pelt, S. (2009). *Dynamic neural representations of human visuomotor space.* Radboud University Nijmegen, Nijmegen, the Netherlands.
11. Lommertzen, J. (2009). *Visuomotor coupling at different levels of complexity.* Radboud University Nijmegen, Nijmegen, the Netherlands.
12. Poljac, E. (2009). *Dynamics of cognitive control in task switching: looking beyond the switch cost.* Radboud University Nijmegen, Nijmegen, the Netherlands.
13. Poser, B.A. (2009). *Techniques for BOLD and blood volume weighted fMRI.* Radboud University Nijmegen, Nijmegen, the Netherlands.
14. Baggio, G. (2009). *Semantics and the electrophysiology of meaning. Tense, aspect, event structure.* Radboud University Nijmegen, Nijmegen, the Netherlands.
15. van Wingen, G.A. (2009). *Biological determinants of amygdala functioning.* Radboud University Nijmegen Medical Centre, Nijmegen, the Netherlands.
16. Bakker, M. (2009). *Supraspinal control of walking: lessons from motor imagery.* Radboud University Nijmegen Medical Centre, Nijmegen, the Netherlands.
17. Aarts, E. (2009). *Resisting temptation: the role of the anterior cingulate cortex in adjusting cognitive control.* Radboud University Nijmegen, Nijmegen, the Netherlands.
18. Prinz, S. (2009). *Waterbath stunning of chickens: effects of electrical parameters on the electroencephalogram and physical reflexes of broilers.* Radboud University Nijmegen, Nijmegen, the Netherlands.
19. Knippenberg, J.M.J. (2009). *The N150 of the Auditory Evoked Potential from the rat amygdala: in search for its functional significance.* Radboud University Nijmegen, Nijmegen, the Netherlands.
20. Dumont, G.J.H. (2009). *Cognitive and physiological effects of 3,4-methylenedioxymethamphetamine (MDMA or 'ecstasy) in combination with alcohol or cannabis in humans.*Radboud University Nijmegen, Nijmegen, the Netherlands.
21. Pijnacker, J. (2010). *Defeasible inference in autism: a behavioral and electrophysiogical approach.*

Radboud University Nijmegen, Nijmegen, the Netherlands.

22. de Vrijer, M. (2010). *Multisensory integration in spatial orientation.* Radboud University Nijmegen, Nijmegen, the Netherlands.
23. Vergeer, M. (2010). *Perceptual visibility and appearance: effects of color and form.* Radboud University Nijmegen, Nijmegen, the Netherlands.
24. Levy, J. (2010). *In cerebro unveiling unconscious mechanisms during reading.* Radboud University Nijmegen, Nijmegen, the Netherlands.
25. Treder, M. S. (2010). Symmetry in (inter)action. Radboud University Nijmegen, Nijmegen, the Netherlands.
26. Horlings C.G.C. (2010). *A Weak balance; balance and falls in patients with neuromuscular disorders.* Radboud University Nijmegen, Nijmegen, the Netherlands.
27. Snaphaan, L.J.A.E. (2010). *Epidemiology of poststroke behavioural consequences.* Radboud University Nijmegen Medical Centre, Nijmegen, the Netherlands.
28. Dado-Van Beek, H.E.A. (2010). *The regulation of cerebral perfusion in patients with Alzheimers disease.* Radboud University Nijmegen Medical Centre, Nijmegen, the Netherlands.
29. Derks, N.M. (2010). *The role of the nonpreganglionic Edinger-Westphal nucleus in sexdependent stress adaptation in rodents.* Radboud University Nijmegen, Nijmegen, the Netherlands.
30. Wyczesany, M. (2010). *Covariation of mood and brain activity: integration of subjective self-report data with quantitative EEG measures.* Radboud University Nijmegen, Nijmegen, the Netherlands.
31. Beurze S.M. (2010). *Cortical mechanisms for reach planning.* Radboud University Nijmegen, Nijmegen, the Netherlands.
32. van Dijk, J.P. (2010). *On the number of motor units.* Radboud University Nijmegen, Nijmegen, the Netherlands.
33. Lapatki, B.G. (2010). *The facial musculature: characterization at a motor unit level.* Radboud University Nijmegen, Nijmegen, the Netherlands.
34. Kok, P. (2010). *Word order and verb inflection in agrammatic sentence production.* Radboud University Nijmegen, Nijmegen, the Netherlands.
35. van Elk, M. (2010). *Action semantics: functional and neural dynamics.* Radboud University Nijmegen, Nijmegen, the Netherlands.
36. Majdandzic, J. (2010). *Cerebral mechanisms of processing action goals in self and others.* Radboud University Nijmegen, Nijmegen, the Netherlands.
37. Snijders, T.M. (2010). *More than words: neural and genetic dynamics of syntactic unification.* Radboud University Nijmegen, Nijmegen, the Netherlands.
38. Grootens, K.P. (2010). *Cognitive dysfunction and effects of antipsychotics in schizophrenia and borderline personality disorder.* Radboud University Nijmegen Medical Centre, Nijmegen, the Netherlands.
39. Nieuwenhuis, I.L.C. (2010). *Memory consolidation: a process of integration – converging evidence from MEG, fMRI and behavior.* Radboud University Nijmegen Medical Centre, Nijmegen, the Netherlands.
40. Menenti, L.M.E. (2010). *The right language: differential hemispheric contributions to language production and comprehension in context.* Radboud University Nijmegen, Nijmegen, the Netherlands.
41. van Dijk, H.P. (2010). *The state of the brain, how alpha oscillations shape behaviour and event related responses.* Radboud University Nijmegen, Nijmegen, the Netherlands.
42. Meulenbroek, O.V. (2010). *Neural correlates of episodic memory in healthy aging and Alzheimers disease.* Radboud University Nijmegen, Nijmegen, the Netherlands.
43. Oude Nijhuis, L.B. (2010). *Modulation of human balance reactions.* Radboud University Nijmegen, Nijmegen, the Netherlands.
44. Qin, S. (2010). *Adaptive memory: imaging medial temporal and prefrontal memory systems.* Radboud University Nijmegen, Nijmegen, the Netherlands.
45. Timmer, N.M. (2011). *The interaction of heparan sulfate proteoglycans with the amyloid β protein.* Radboud University Nijmegen, Nijmegen, the Netherlands.
46. Crajé, C. (2011). *(A)typical motor planning and motor imagery.* Radboud University Nijmegen, Nijmegen, the Netherlands.
47. van Grootel, T.J. (2011). *On the role of eye and head position in spatial localisation behaviour.* Radboud University Nijmegen, Nijmegen, the Netherlands.
48. Lamers, M.J.M. (2011). *Levels of selective attention in action planning.* Radboud University Nijmegen, Nijmegen, the Netherlands.
49. van der Werf, J. (2011). *Cortical oscillatory activity in human visuomotor integration.* Radboud University Nijmegen, Nijmegen, the Netherlands.
50. Scheeringa, R. (2011). *On the relation between oscillatory EEG activity and the BOLD signal.* Radboud University Nijmegen, Nijmegen, the Netherlands.
51. Bögels, S. (2011). *The role of prosody in language comprehension: when prosodic breaks and pitch accents come into play.* Radboud University Nijmegen, Nijmegen, the Netherlands.

52. Ossewaarde, L. (2011). *The mood cycle: hormonal influences on the female brain.* Radboud University Nijmegen, Nijmegen, the Netherlands.
53. Kuribara, M. (2011). *Environment-induced activation and growth of pituitary melanotrope cells of Xenopus laevis.* Radboud University Nijmegen, Nijmegen, the Netherlands.
54. Helmich, R.C.G. (2011). *Cerebral reorganization in Parkinsons disease.* Radboud University Nijmegen, Nijmegen, the Netherlands.
55. Boelen, D. (2011). *Order out of chaos? Assessment and treatment of executive disorders in brain-injured patients.* Radboud University Nijmegen, Nijmegen, the Netherlands.
56. Koopmans, P.J. (2011). *fMRI of cortical layers.* Radboud University Nijmegen, Nijmegen, the Netherlands.
57. van der Linden, M.H. (2011). *Experience-based cortical plasticity in object category representation.* Radboud University Nijmegen, Nijmegen, the Netherlands.
58. Kleine, B.U. (2011). *Motor unit discharges: physiological and diagnostic studies in ALS.* Radboud University Nijmegen Medical Centre, Nijmegen, the Netherlands.
59. Paulus, M. (2011). *Development of action perception: neurocognitive mechanisms underlying childrens processing of others actions.* Radboud University Nijmegen, Nijmegen, the Netherlands.
60. Tieleman, A.A. (2011). *Myotonic dystrophy type 2. A newly diagnosed disease in the Netherlands.* Radboud University Nijmegen Medical Centre, Nijmegen, the Netherlands.
61. van Leeuwen, T.M. (2011). *How one can see what is not there: neural mechanisms of grapheme-colour synaesthesia.* Radboud University Nijmegen, Nijmegen, the Netherlands.
62. van Tilborg, I.A.D.A. (2011). *Procedural learning in cognitively impaired patients and its application in clinical practice.* Radboud University Nijmegen, Nijmegen, the Netherlands.
63. Bruinsma, I.B. (2011). *Amyloidogenic proteins in Alzheimers disease and Parkinsons disease: interaction with chaperones and inflammation.* Radboud University Nijmegen, Nijmegen, the Netherlands.
64. Voermans, N. (2011). *Neuromuscular features of Ehlers-Danlos syndrome and Marfan syndrome; expanding the phenotype of inherited connective tissue disorders and investigating the role of the extracellular matrix in muscle.* Radboud University Nijmegen Medical Centre, Nijmegen, the Netherlands.
65. Reelick, M. (2011). *One step at a time. Disentangling the complexity of preventing falls in frail older persons.* Radboud University Nijmegen Medical Centre, Nijmegen, the Netherlands.
66. Buur, P.F. (2011). *Imaging in motion. Applications of multi-echo fMRI.* Radboud University Nijmegen, Nijmegen, the Netherlands.
67. Schaefer, R.S. (2011). *Measuring the minds ear: EEG of music imagery.* Radboud University Nijmegen, Nijmegen, the Netherlands.
68. Xu, L. (2011). *The non-preganglionic Edinger-Westphal nucleus: an integration center for energy balance and stress adaptation.* Radboud University Nijmegen, Nijmegen, the Netherlands.
69. Schellekens, A.F.A. (2011). *Gene-environment interaction and intermediate phenotypes in alcohol dependence.* Radboud University Nijmegen, Nijmegen, the Netherlands.
70. van Marle, H.J.F. (2011). *The amygdala on alert: a neuroimaging investigation into amygdala function during acute stress and its aftermath.* Radboud University Nijmegen, Nijmegen, the Netherlands.
71. de Laat, K.F. (2011). *Motor performance in individuals with cerebral small vessel disease: an MRI study.* Radboud University Nijmegen Medical Centre, Nijmegen, the Netherlands.
72. Mädebach, A. (2011). *Lexical access in speaking: studies on lexical selection and cascading activation.* Radboud University Nijmegen, Nijmegen, the Netherlands.
73. Poelmans, G.J.V. (2011). *Genes and protein networks for neurodevelopmental disorders.* Radboud University Nijmegen, Nijmegen, the Netherlands.
74. van Norden, A.G.W. (2011). *Cognitive function in elderly individuals with cerebral small vessel disease. An MRI study.* Radboud University Nijmegen Medical Centre, Nijmegen, the Netherlands.
75. Jansen, E.J.R. (2011). *New insights into V-ATPase functioning: the role of its accessory subunit Ac45 and a novel brain-specific Ac45 paralog.* Radboud University Nijmegen, Nijmegen, the Netherlands.
76. Haaxma, C.A. (2011). *New perspectives on preclinical and early stage Parkinson's disease.* Radboud University Nijmegen Medical Centre, Nijmegen, the Netherlands.
77. Haegens, S. (2012). *On the functional role of oscillatory neuronal activity in the somatosensory system.* Radboud University Nijmegen, Nijmegen, the Netherlands.
78. van Barneveld, D.C.P.B.M. (2012). *Integration of exteroceptive and interoceptive cues in spatial localization.* Radboud University Nijmegen, Nijmegen, the Netherlands.
79. Spies, P.E. (2012). *The reflection of Alzheimer disease in CSF.* Radboud University Nijmegen Medical Centre, Nijmegen, the Netherlands.

80. Helle, M. (2012). *Artery-specific perfusion measurements in the cerebral vasculature by magnetic resonance imaging.* Radboud University Nijmegen, Nijmegen, the Netherlands.
81. Egetemeir, J. (2012). *Neural correlates of real-life joint action.* Radboud University Nijmegen, Nijmegen, the Netherlands.
82. Janssen, L. (2012). *Planning and execution of (bi)manual grasping.* Radboud University Nijmegen, Nijmegen, the Netherlands.
83. Vermeer, S. (2012). *Clinical and genetic characterisation of Autosomal Recessive Cerebellar Ataxias.* Radboud University Nijmegen Medical Centre, Nijmegen, the Netherlands.
84. Vrins, S. (2012). *Shaping object boundaries: contextual effects in infants and adults.* Radboud University Nijmegen, Nijmegen, the Netherlands.
85. Weber, K.M. (2012). *The language learning brain: evidence from second language and bilingual studies of syntactic processing.* Radboud University Nijmegen, Nijmegen, the Netherlands.
86. Verhagen, L. (2012). *How to grasp a ripe tomato.* Utrecht University, Utrecht, the Netherlands.
87. Nonkes, L.J.P. (2012). *Serotonin transporter gene variance causes individual differences in rat behaviour: for better and for worse.* Radboud University Nijmegen Medical Centre, Nijmegen, the Netherlands.
88. Joosten-Weyn Banningh, L.W.A. (2012). *Learning to live with Mild Cognitive Impairment: development and evaluation of a psychological intervention for patients with Mild Cognitive Impairment and their significant others.* Radboud University Nijmegen Medical Centre, Nijmegen, the Netherlands.
89. Xiang, HD. (2012). *The language networks of the brain.* Radboud University Nijmegen, Nijmegen, the Netherlands.
90. Snijders, A.H. (2012). *Tackling freezing of gait in Parkinson's disease.* Radboud University Nijmegen Medical Centre, Nijmegen, the Netherlands.
91. Rouwette, T.P.H. (2012). *Neuropathic pain and the brain: differential involvement of corticotropin-releasing factor and urocortin 1 in acute and chronic pain processing.* Radboud University Nijmegen Medical Centre, Nijmegen, the Netherlands.
92. van de Meerendonk, N. (2012). *States of indecision in the brain: electrophysiological and hemodynamic reflections of monitoring in visual language perception.* Radboud University Nijmegen, Nijmegen, the Netherlands.
93. Sterrenburg, A. (2012). *The stress response of forebrain and midbrain regions: neuropeptides, sex-specificity and epigenetics.* Radboud University Nijmegen, Nijmegen, the Netherlands.
94. Uithol, S. (2012). *Representing action and intention.* Radboud University Nijmegen, Nijmegen, the Netherlands.
95. van Dam, W.O. (2012). *On the specificity and flexibility of embodied lexical-semantic representations.* Radboud University Nijmegen, Nijmegen, the Netherlands.
96. Slats, D. (2012). *CSF biomarkers of Alzheimers disease; serial sampling analysis and the study of circadian rhythmicity.* Radboud University Nijmegen Medical Centre, Nijmegen, the Netherlands.
97. Van Nuenen, B.F.L. (2012). *Cerebral reorganization in premotor parkinsonism.* Radboud University Nijmegen Medical Centre, Nijmegen, the Netherlands.
98. van Schouwenburg, M.R. (2012). *Fronto-striatal mechanisms of attentional control.* Radboud University Nijmegen, Nijmegen, the Netherlands.
99. Azar, M.G. (2012). *On the theory of reinforcement learning: methods, convergence analysis and sample complexity.* Radboud University Nijmegen, Nijmegen, the Netherlands.
100. Meeuwissen, E.B. (2012). *Cortical oscillatory activity during memory formation.* Radboud University Nijmegen, Nijmegen, the Netherlands.
101. Arnold, J.F. (2012). *When mood meets memory: neural and behavioral perspectives on emotional memory in health and depression.* Radboud University Nijmegen, Nijmegen, the Netherlands.
102. Gons, R.A.R. (2012). *Vascular risk factors in cerebral small vessel disease: a diffusion tensor imaging study.* Radboud University Nijmegen Medical Centre, Nijmegen, the Netherlands.
103. Wingbermhle, E. (2012). *Cognition and emotion in adults with Noonan syndrome: a neuropsychological perspective.* Radboud University Nijmegen, Nijmegen, the Netherlands.
104. Walentowska, W. (2012). *Facing emotional faces. The nature of automaticity of facial emotion processing studied with ERPs.* Radboud University Nijmegen, Nijmegen, the Netherlands.
105. Hoogman, M. (2012). *Imaging the effects of ADHD risk genes.* Radboud University Nijmegen, Nijmegen, the Netherlands.
106. Tramper, J.J. (2012). *Feedforward and feedback mechanisms in sensory motor control.* Radboud University Nijmegen, Nijmegen, the Netherlands.